Optimising the Mobility of Nanoporous Titanium Dioxide

James Anthony Quirk

Doctor of Philosophy

Physics

April 2021

"If people did not sometimes do silly things, nothing intelligent would ever get done." – Ludwig Wittgenstein

Optimising the Mobility of Nanoporous Titanium Dioxide

J. A. Quirk

Submitted for the degree of Doctor of Philosophy in Physics
April 2021

Abstract

Titanium dioxide (TiO_2) has drawn significant attention due to its low cost, abundance, and wide array of energy applications including as an electron transport layer in solar cells, as a photocatalyst for hydrogen production, and as an electrode material in rechargeable batteries. Of the many polymorphs of TiO_2, anatase shows the most promise due to its high conductivity and excellent performance in devices. This high performance can, in part, be attributed to anatase not strongly trapping electrons in bulk-like regions of the crystal. However, a description of bulk properties is not sufficient because anatase is unstable as large, single crystals and so it usually produced as nanoparticles which are then sintered together. Polycrystalline materials have large surface area and a large number of grain boundaries where the particles come into contact with one another. These extended defects are expected to play a large role in the properties of anatase, but it is not straightforward to devise experiments that are able disentangle the individual roles of surfaces, grain boundaries, and point defects. This thesis presents first-principles models of extended defects in anatase and, where possible, makes comparison with experiment through the simulation of transmission electron microscopy. It is shown that anatase grain boundaries can introduce deep hole traps, but show no sign of electron trapping. Similarly, oxygen vacancies do not strongly trap electrons but the segregation of these ionised vacancies to the boundaries causes a space charge region to develop, which would pose a barrier to inter-grain electron transport. Models of highly-oxygen deficient nanoparticles indicate that electron trapping can occur on under-coordinated titanium sites and we propose that the oriented attachment of nanoparticles along highly oxygen-deficient facets would enable the formation of highly oxygen-deficient grain boundaries that would exhibit significant electron trapping.

Declaration

The work in this thesis is based on research carried out in Keith McKenna's group, Department of Physics, University of York, England. This work has not previously been presented for an award at this, or any other, University. All sources are acknowledged as References.

Chapter 5 represents collaborative which forms a manuscript which has just been accepted: J. A. Quirk, B. Miao, B. Feng, G. Kim, H. Ohta, Y. Ikuhara, and K. P. McKenna, "Unveiling the Electronic Structure of Grain Boundaries in Anatase with Electron Microscopy and First-Principles Modelling," Nano Lett., 2021. Miao B, Feng B, Kim G, Ohta H, and Ikuhara Y were responsible for all sample fabrication and experimental analysis. All computational work and the writing of the draft manuscript was carried out by myself.

Acknowledgements

Formal Acknowledgements

I would like to thank my supervisors Prof. Keith McKenna and Prof. Vlado Lazarov for their invaluable guidance and support throughout the entirety of this project, as well as all the members of the McKenna Materials Modelling Group, past and present. I would also like to offer special thanks to our experimental collaborators Dr. Bin Feng, Dr. Bin Miao, and the other members of Prof. Yuichi Ikuhara's research group, who fabricated and performed analysis on the anatase bicrystals seen in this thesis. Computational work made use of the facilities of Archer, the United Kingdom's national high-performance computing service, via the McKenna Materials Modelling Group's membership in the UK HPC Materials Chemistry Consortium, which is funded by EPSRC (EP/L000202/1 and EP/R029431/1), as well as making use of the Viking Cluster, which is a high-performance computation facility provided by the University of York. I am grateful for computational support from the University of York High Performance Computing service, Viking and the Research Computing team.

Informal Acknowledgements

Of all the various group members, I would like to especially thank my fellow PhD students, Razak and Adam. Aside from making the whole experience much more fun and bearable, they also had their uses; Razak is responsible for this thesis template which (mostly) worked without issue and Adam is responsible for many occasions of looking at my Python scripts and deciding he could do a better job in half the time. If I get nothing else out of my PhD, I've gained two very good friends. I look forward to seeing them, and everybody else, again for the inevitable night out in York, once the pandemic is over.

Outside of students and staff at the University of York, I have to thank my parents for supplying me with care packages of biscuits and beer throughout my entire course of study. I should also mention my two family dogs, Ellie and Daisy, who gave me a reason to actually leave the house and see sunlight during my time as a computational physicist. Finally, I also want to express my sincere gratitude to Niamh, for all of her unending support and her willingness to listen to me rant and rave about whatever problems felt impossible that day and for giving me the motivation and confidence to work through them. I could not have asked for a better partner to help me through my PhD.

Publications

The following is a list publications that contribute to this thesis. Chapters which use wording from these publications have the relevant publication mentioned at the beginning of the chapter.

1. Quirk JA, Lazarov VK, and McKenna KP. "Electronic Properties of 112 and 110 Twin Boundaries in Anatase TiO_2," *Adv. Theory Simul*, vol. 2, no. 12, pp. 1900157, 2019.

2. Quirk JA, Lazarov VK, and McKenna KP. "First-Principles Modeling of Oxygen-Deficient Anatase TiO_2 Nanoparticles," *J. Phys. Chem. C*, vol. 124, no. 43, pp. 23637-23647, 2020.

3. Quirk JA, Miao B, Feng B, Kim G, Ohta H, Ikuhara Y, and McKenna KP, "Unveiling the Electronic Structure of Grain Boundaries in Anatase with Electron Microscopy and First-Principles Modelling," *Nano Lett.*, 2021. (Just Accepted)

The following manuscripts did not contribute to this thesis but are related to charge trapping in anatase and include calculations carried out during the course of this project.

4. Carey JJ, Quirk JA, McKenna KP. "Hole Polaron Migration in Bulk Phases of TiO_2 Using Hybrid Density Functional Theory," *J. Phys. Chem. C*, vol. 125, no. 22, pp. 12441-12450, 2021.

5. JA Quirk, KP McKenna. "First-Prinicples Modeling of Carrier Recombination at Self-Trapped Hole Polarons in Bulk TiO_2," (In preparation)

Contents

List of Figures

List of Tables

Chapter 1

Introduction

1.1 Why Titanium Dioxide?

As global energy usage increases and the climate catastrophe draws nearer it is now more important than ever to develop renewable, low-emissions energy sources. Advances in solid-state devices have lead to solutions such as photovoltaics (PVs) for reaping energy from sunlight, photocatalysts for producing hydrogen through water splitting, and battery electrodes and ionic conductors for safe and efficient energy storage. Some promising technology relies on relatively rare elements,[1–8] which involves a large carbon footprint as well as encouraging destructive mining practices in order to produce viable quantities of the element. The scarcity of and demand for the ores of certain metals such as tin, tungsten, and tantalum make them hotly-contested enough that their supply chains are tainted by bloodshed and modern slavery.[9–11] If we are to ethically replace a large portion of the world's energy production with renewable sources, it is not enough to simply choose materials with which we can maximise the theoretical efficiency. We must also choose materials that minimise the ecological and sociological costs associated with their supply chains. Intuitively, the solution is to choose Earth-abundant elements that are commonplace and cheap-to-extract.

A standard example of an Earth-abundant element would be silicon, which has a wide range of electronic applications from transistors to PVs, so perhaps we shall choose silicon to build our device. Now, we are faced with unavoidable process of fabricating a useful device starting from raw materials. If we focus our attention on PVs, a silicon solar panel requires extremely pure crystals with a low density of defects and the energy-intensive refinement process severely limits the rate at which a silicon PV device can recover the energy used to create it.[12] Even if the refinement process were cheaper, silicon is not an especially strong absorber of sunlight and so the silicon

wafers must be quite thick if high efficiencies of around 20% are desired, which adds to the weight and cost. On top of this, silicon wafers tend be rather brittle, meaning that they must be reinforced by bulky glass panels.[13,14] These bulky, rigid panels increase transport costs and pose problems for deployment as it limits the areas in which they can be sensibly placed. There are, of course, approaches to maximising gains from traditional, rigid PV arrays such as implementing bifacial panels, where the reverse-side of panels also collects light that has been reflected from the ground below the panel,[15] but an ideal device would be lightweight and flexible enough that it can easily be deployed onto any surface of any shape. Flexible PV modules of around 7% to 11% efficiency have been fabricated using cadmium telluride,[16] but widespread deployment of such devices is prohibited by the rarity of tellurium in the Earth's crust.[17]

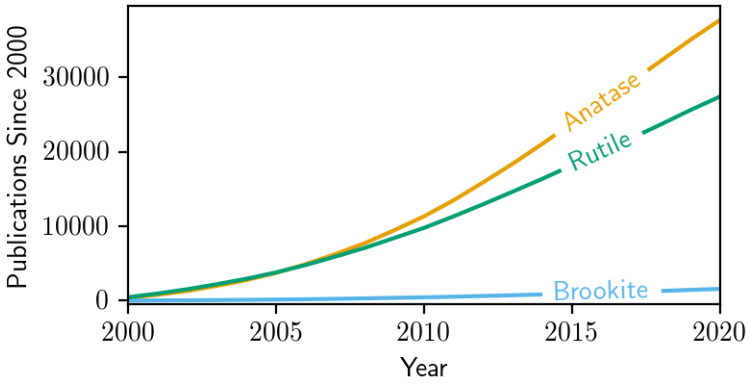

Fig. 1.1. Graph showing the cumulative number publications since 2000 concerning the anatase, rutile, and brookite polymorphs of TiO_2. Anatase is the most-researched of these polymorphs. Publication data was taken from a keyword search on the Thomson Reuters' Web of Science tool.[18]

When designing a device, there is the challenging problem of striking a balance between following criteria: 1) the material must be abundant, 2) the material must be cheap to process, 3) the devices made from the material must be efficient, and 4) the devices made from the material must be easy to deploy. A material that meets these criteria, and the focus of this thesis, is titanium dioxide (TiO_2). Titanium and its ores are commonplace in the Earth's crust and oxygen is famously (and fortunately) abundant in our atmosphere. In addition to this, TiO_2 can be synthesised through facile wet-chemistry methods,[19] as well as being relatively inert and non-toxic enough for it to be safe to deploy without too many concerns.[20–22] The various polymorphs of TiO_2 have drawn enormous attention for their potential environmental and energy-production applications including: as a photocatalyst, where it can be used to split

water for hydrogen production[23–26] or to break down pollutants for wastewater remediation;[27–29] as an electron transport medium with good conductivity in low-cost and flexible perovskite and dye-sensitised solar cells (DSSCs);[30–33] and as an anode material for rechargeable batteries, where it allows intercalation of lithium and sodium ions.[34–40] Of these polymorphs, the most commonly-discussed are anatase, rutile, and brookite. Anatase has drawn the most interest due to its excellent photocatalytic performance[41–43] and conductivity[44–48] compared to its peers (Figure 1.1). In order to understand why anatase performs so well, it is essential to understand how charge carriers (electrons and holes) behave in the material. However, as shall be seen in the following sections, an understanding of charge carrier behaviour is not straightforward in TiO_2, an issue which is further complicated by the fact that anatase proves particularly challenging to probe experimentally.

1.2 Charge Carriers in Titanium Dioxide

Charge carriers play a decisive role in enabling semiconductors to be applied to renewable energy generation and storage. The sharing and exchange of electrons between atoms will make and break the chemical bonds, governing the electronic properties of a material. In an idealised semiconducting material, there is a forbidden range of energies in which no electronic states exist known as the band gap. The band gap separates the occupied states in the valence band and the unoccupied states in the conduction band, where states in either the valence or conduction band are delocalised. Incident light can interact to excite an electron from an occupied state in the valence band into an unoccupied state in the conduction band. In a PV device, we would want these charge carriers to conduct and produce a current to generate power.[13] In a photocatalytic device, we would want these charge carriers to migrate to the surface of the material where they can undergo reactions with adsorbates.[25]

In practice, semiconductors employed in devices are not ideal and states often appear in the band gap. These states are usually associated with defects or impurities in the material (as shall be discussed in greater detail in Section 3.1). Unlike states in the valence or conduction bands, states in the gap are localised and are responsible for the trapping of charge. Charge trapping can sometimes be beneficial to the operation of a device, such as in the case of photocatalysis, where charge carriers becoming trapped and immobile at the surface of a material will increase the likelihood that the carrier interacts with an adsorbate to catalyse a reaction.[49,50] In other cases, charge trapping

will be detrimental. For example, charge traps will reduce carrier mobility and reduce the conductivity of the device, which will have an impact on the efficiency of a PV device. A trapped charge is also more likely to undergo electron-hole recombination. Recombination can be radiative, where a hole and electron recombine and release a photon; this process is not necessarily too detrimental as the photon can be absorbed again to generate a fresh electron-hole pair. The counterpart is non-radiative recombination, where the carrier pair recombine and release a phonon; this process destroys the free electron and hole before either of them can become useful and is severely pathological for both PV and photocatalytic applications.[51,52]

The common point defects in TiO_2 are typically donor defects, meaning that they introduce excess electrons into the system and dope it to be *n*-type. The standard example of an intrinsic donor defect is the oxygen vacancy, which is prevalent in TiO_2 due to its tendency to be oxygen-deficient. Some proportion of the excess electrons introduced by oxygen vacancies will become trapped on Ti atoms adjacent to the vacant site, but theoretical work suggests that vacancies in the bulk have a tendency towards allowing the excess electrons to delocalise. This delocalisation is predicted to be significantly more favourable in anatase than it is in rutile.[53,54] Examples of extrinsic donor defects would be due to intentional *n*-type doping with elements such as niobium or tantalum in order to improve conductivity. When doping TiO_2 with niobium, it is found that anatase exhibits high, metallic conductivity, whereas rutile remains semiconducting and resistive.[44,47,48] This is attributed to the fact that, in anatase, the states associated with the dopants are very diffuse and lie close to the conduction band maximum (CBM), meaning that the excess electrons can easily delocalise into the conduction band. In rutile, the dopants introduce a state around 1.0 eV below CBM, with electrons becoming trapped on Ti sites adjacent to the dopant.[45]

No material will ever be entirely free from defects and so charge trapping and carrier recombination will never be completely avoidable, though through a good fundamental understanding of the processes involved we can aim to engineer materials in order to mitigate the detrimental effects and exploit the beneficial effects. But, even in an infinite crystal that contained no defects, charge trapping can still occur. In a crystalline lattice made up of charged ions (in the case of TiO_2 these ions are Ti^{4+} and O^{2-}) the lattice will deform in response to the introduction of a charged species (such as an electron or a hole) due to the electrostatic interaction between the charged ions and the charged species, polarising the lattice. This coupling of the charge carrier with

the lattice phonons is a quasiparticle known as a polaron. In some materials, such as TiO_2,[54–58] this lattice polarisation induced by the carrier can then force the charge carrier to become localised on a specific site as a small polaron; the carrier has trapped itself. This so-called self-trapping is a mechanism by which charge carriers (electrons, or holes, or both, depending on the material or polymorph) can become trapped in the defect-free bulk and it can have profound effects on the properties of a material.

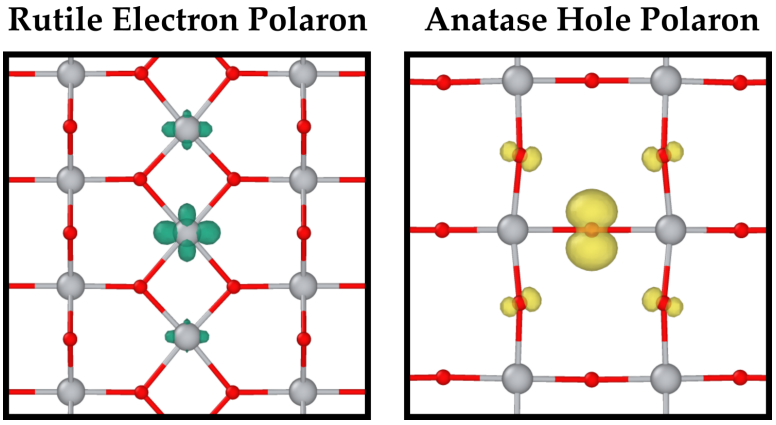

Fig. 1.2. Spin density isosurfaces (density displayed at 0.02 a_0^{-3}) showing (left) an electron trapping to form a Ti^{3+} in rutile and (right) a hole trapping to form a O^- in anatase. The polaronic distortion is most visibly pronounced in the case of anatase. Titanium and oxygen ions are represented by gray spheres and red spheres, respectively. For clarity, only one layer of atoms has been shown in each structure.

In TiO_2, an electron polaron would involve an electron trapping on Ti^{4+} to form Ti^{3+} and a hole polaron would involve a hole trapping on O^{2-} to form O^-. The presence of these polarons can be probed through various experimental techniques such: electron paramagnetic resonance (EPR), which will detect the unpaired spins associated with Ti^{3+} and O^-;[59] photoluminescence (PL) spectroscopy which will detect the photon emissions associated with polarons acting radiative recombination centres;[60–62] or conductivity measurements which can determine how the hopping of small polarons is involved in conductivity.[63] A combination of experimental and theoretical work has predicted that bulk rutile will not allow holes to become self-trapped but will allow electrons to trap. The reverse is true for bulk anatase, where electrons will not become self-trapped but holes will .[54,56,57] It is usually the case that TiO_2 is oxygen deficient, where this oxygen deficiency leads to an excess of electrons and dopes the material to be n-type. Given that electrons are the majority charge carrier in TiO_2, the tendency of rutile to trap electrons in bulk will severely impact its conductivity when compared to anatase, which will reduce its performance as an electron transport layer in PV

applications.

The behaviour of carriers in bulk anatase or at point defects appears to paint a picture of anatase being a material that does not strongly trap electrons. This is a partially satisfactory explanation for its good performance as a conductor, but it is an incomplete description. No crystal can ever be infinitely periodic, it must eventually terminate in a surface or an interface. These extended defects (and point defects in the vicinity of these extended defects) also play a large role in determining the properties of a material.

1.3 Polycrystalline Anatase

Anatase has a tetragonal crystal structure with the space group $I4_1/amd$ (Figure 1.3) with experimental lattice parameters of $a = b = 3.78$ Å, and $c = 9.51$ Å.[64] Anatase is not thermodynamically stable as large, single crystals and will undergo an irreversible phase transition into rutile if crystals grow too large or if it is processed incorrectly.[65–67] Because of this, sol-gel synthesis is usually used to produce nanoparticles which can then be sintered together to produce a nanoporous lattice of particles.[68,69] Whilst each individual nanoparticle is crystalline and highly-ordered, the resulting sintered specimen is highly irregular with a large surface area and large numbers of interfaces between particles. Where two grains of a crystalline material meet, a grain boundary (GB) occurs. GBs and surfaces are to be expected in all crystalline materials regardless of fabrication method, but they will be especially prolific in polycrystalline specimens produced by sintering.

Whilst we might describe vacancies, dopants, surfaces, and GBs as defects in the crystal structure, that is not to suggest that defects are always undesirable. In fact, many of the desirable traits of anatase are a direct result of the presence of defects. As discussed already, oxygen vacancies and donor dopants provide the n-type character that enables good conductivity. Polaronic trapping at surfaces can be beneficial for photocatalytic applications by allowing trapped charges to undergo reactions with adsorbed species.[70,71] The high surface area of the sintered specimens is intuitively beneficial in photocatalysis by increasing the area available to adsorbates.[72] High surface area is also beneficial to the functioning of DSSCs by increasing the area in which the solar-absorbing dye can make contact with anatase to be able to inject charge carriers.[73]

We can also expect GBs to impact the properties of anatase, though their role is

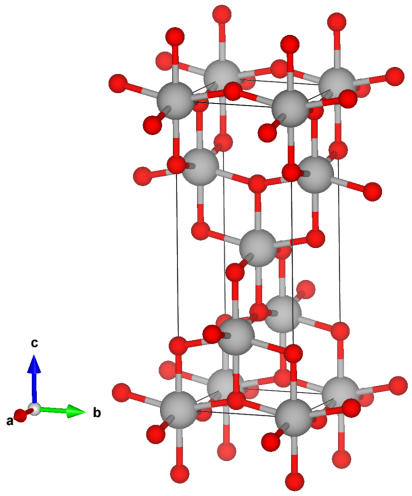

Fig. 1.3. The conventional unit cell of anatase. Titanium and oxygen ions are represented by gray and red spheres, respectively.

less intuitive. The impact of GBs in some materials and applications is beneficial, such as improved current collection at grain boundaries in cadmium telluride solar absorbers.[74] In other applications, GBs are detrimental, such as the decreased ionic conductivity at grain boundaries in lithium lanthanum titanate ionic conductors.[75,76] It is possible to minimise detrimental effects by engineering the properties of grain boundaries, for example through the addition of other dopants[77,78] or controlling the growth and processing conditions of the material.[79] However, if we wish to engineer the properties of defects we need a good understanding of the properties of the defects themselves. Anatase is problematic in this regard as polycrystalline specimens are not especially amenable to experiment (Figure 1.4), which makes it difficult to disentangle the combined effects of bulk properties, point defects, surfaces, and GBs.

Historically, in the absence of convincing evidence, mysticism might have provided a satisfactory explanation; steel was not granted its strength by the complex interactions of carbon defects, but by the ritualistic value of the bone ash used in smithing.[80] Sadly, citing the importance of magic is no longer sufficient and so, instead, we must turn to insight provided by the more rigorous (but no less esoteric) world of computational modelling.

1.4 Computational Modelling

In order to model a material at the atomic scale, the first step is to determine the interactions that we wish to probe. In the case of anatase, we are interested not only

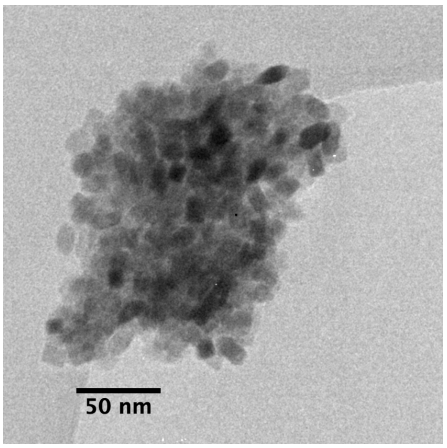

Fig. 1.4. A transmission electron microscopy (TEM) image of a cluster of sintered anatase nanoparticles. The disordered and irregular nature of the specimen makes it difficult to interpret. Image taken by Adam Kerrigan in the Nanocentre at the University of York.

in the atomic structure of the material and extended defects, but also in the electronic structure and behaviour of charge carriers. Atomic structure is sometimes accessible through classical approximations, such as interatomic force fields by which stable structures can be determined.[81] Electronic structure, however, cannot be adequately treated by classical physics and an accurate quantum mechanical description is required. Unfortunately, there is no analytic solution for a system of many interacting electrons and numerical solutions are intractable due to the number of interactions that need to be considered. Electronic structure must therefore be treated using an approximation that reduces computational cost.

The current de-facto standard of electronic structure calculations is density functional theory (DFT) due to its low computational cost and reasonable accuracy. In DFT, the interactions of many electrons are instead replaced by a functional of the electron density.[82,83] There are various approximations and functionals within DFT, but a common trait shared by all 'pure' DFT functionals that have a smooth dependence on the electron density is that they have a tendency towards artificially stabilising delocalised states.[84] Clearly, given that we wish to model charge trapping and localisation, DFT alone is not sufficient. In this thesis, we elect to employ an approach known as hybrid DFT, which combines features of DFT with desirable features of its more computationally-demanding predecessor, Hartree-Fock (HF) theory.[85] In the interest of avoiding excessive repetition, a more complete description of the details of DFT, HF theory, and hybrid DFT shall be saved for Chapter 2.

Previously, the increased computational cost of hybrid DFT placed a limiting factor on its use within solid state physics, with its use generally being relegated to small unit cells of bulk material. In recent years, however, hardware has improved and cost-saving techniques have been introduced into software which allow for large systems including point and extended defects to be tackled. Previous work in our group has developed a hybrid DFT functional optimised for modelling charge trapping in TiO_2,[57,86] which has been employed to model polarons in bulk[57] TiO_2 and at anatase surfaces,[70] as well as to investigate point defects in bulk rutile and anatase.[54] In this thesis, the same methodology is employed to investigate grain boundaries, surfaces, and nanoparticles, as well as how point defects and charge traps interact with and are affected by each of these structures. By doing so, we intend to be able to provide insight at the atomic scale such that the complicated interactions of the defects can be disentangled.

1.5 Work Presented in This Thesis

This thesis aims to use computational models to elucidate the behaviour of charge carriers in polycrystalline anatase. Chapter 2 shall introduce a more detailed discussion of the electronic structure theory employed throughout this thesis. Chapter 3 then goes on to explain how this electronic structure theory can be used to model realistic systems containing surfaces and grain boundaries in order to answer the questions that we wish to answer.

In Chapter 4, we present a study of two low-energy $\Sigma3$ {112} and $\Sigma1$ {110} twin boundaries (TBs). The $\Sigma3$ {112} TB is frequently observed experimentally and is thought to be extremely prevalent in anatase specimens, making it of high technological relevance. The $\Sigma1$ {110} TB has not been observed experimentally, though we identify examples or situations in which it may arise and how it would be detectable. For both TBs, we observe that the electronic structure of anatase is weakly perturbed by the presence of the boundaries and that they would be relatively benign for PV or photocatalytic applications. Both of the TBs are very high symmetry and present no broken bonds, so the open question remains as to whether lower symmetry boundaries would have more significant deleterious - or even beneficial - effects.

We aim to answer the questions posed in Chapter 4 in Chapter 5, where we present work that was carried out in close collaboration with experimental partners in which we investigate experimentally fabricated anatase bicrystals and compare our models with experimental images. It is determined that the findings in Chapter 4 also seem

to apply, where the electronic structure of anatase appears to be rather tolerant to the presence of GBs even where the boundaries are lower-symmetry and contain broken bonds. In this chapter, we also place more focus on the behaviour of dilute oxygen vacancies in the vicinity of GBs and show that, whilst these vacancies do not seem prone to trapping electrons, the presence of higher quantities of charged defects in the vicinity of the boundary would pose an electrostatic potential barrier to electrons passing through the boundary. We also look present a model for an unusual, highly oxygen-deficient boundary that exhibits electron trapping and would be detrimental to performance. These results highlight the importance of considering non-stoichiometry in extended defects.

The other results presented in this thesis focus on relatively high-symmetry and largely stoichiometric extended defects. Nanoparticles, however, also contain many low-symmetry features such as edges and vertices where facets meet, which should be expected to also affect properties. In Chapter 6 we present atomic and electronic structures of explicit models of oxygen-deficient nanoparticles and compare them to models of extended surfaces, to show that smaller nanoparticles are more easily reduced than their larger counterparts and that electron traps are common near the surfaces of highly-reduced particles. These results highlight that there is a fine balance to be struck between the increased conductivity due to excess electrons introduced by oxygen-deficiency, and the decreased mobility that comes with more prevalent electron traps in reduced nanoparticles.

Chapter 2

Electronic Structure Theory

The properties of a material are almost entirely determined by the behaviour of electrons within the material. In the simple case of a hydrogen atom there is one electron interacting only with the nucleus and an exact analytic solution is possible. If a system contains multiple atoms, each electron is now interacting with all other electrons as well as with each of the nuclei; such a situation is known as a many-body problem. There is no analytic solution for this situation and, as the number of bodies in the system increases, the number of interactions increases so rapidly that exact numerical solutions also become intractable. Producing accurate approximate solutions to many-body quantum mechanical problems remains one of the most arduous and time-consuming challenges in modern physics. This chapter shall outline the theoretical and practical details of solving such a problem.

2.1 Many-Body Quantum Mechanics

The state of a quantum system can be fully described by the wavefunction, $\mathbf{\Psi}$. Every observable, A, can be yielded by using the corresponding Hermitian operator, $\hat{\mathcal{A}}$. Each $\hat{\mathcal{A}}$ has a set of orthonormal eigenfunctions, $\{\mathbf{\Psi}_i\}$, and a set of real eigenvalues $\{a_i\}$ which are solutions to the eigenequation

$$\hat{\mathcal{A}}\mathbf{\Psi}_i = a_i\mathbf{\Psi}_i. \tag{2.1}$$

A special case of Equation 2.1 is the time-independent Schrödinger equation (TISE),

$$\hat{\mathcal{H}}\mathbf{\Psi}_i = E_i\mathbf{\Psi}_i, \tag{2.2}$$

where $\hat{\mathcal{H}}$ is the operator associated with the total energy of the system E, which we define as

$$\hat{\mathcal{H}} = \hat{\mathcal{T}} + \hat{\mathcal{V}}, \tag{2.3}$$

where $\hat{\mathcal{T}}$ is the kinetic energy and $\hat{\mathcal{V}}$ is the potential energy. For a system containing N_n atomic nuclei at positions $\mathbf{R}_i$ and N_e electrons at positions $\mathbf{r}_i$, we can break $\hat{\mathcal{T}}$ and $\hat{\mathcal{V}}$ down into

$$\hat{\mathcal{T}} = \hat{\mathcal{T}}_n + \hat{\mathcal{T}}_e \qquad \text{and} \qquad \hat{\mathcal{V}} = \hat{\mathcal{V}}_{n-n} + \hat{\mathcal{V}}_{n-e} + \hat{\mathcal{V}}_{e-e},$$

where the subscripts n and e indicate nuclear and electronic components and $n-n$, $n-e$, and $e-e$ subscripts indicate all unique interactions between nuclei and electrons and where (in Hartree atomic units*) each term can be defined as

$$\hat{\mathcal{T}}_n = -\frac{1}{2}\sum_{i}^{N_n}\frac{1}{M_i}\nabla_i^2, \qquad \hat{\mathcal{V}}_{n-n} = \sum_{i}^{N_n}\sum_{j>i}^{N_n}\frac{Z_i Z_j}{|\mathbf{R}_i - \mathbf{R}_j|},$$

$$\hat{\mathcal{T}}_e = -\frac{1}{2}\sum_{i}^{N_e}\nabla_i^2, \qquad \hat{\mathcal{V}}_{n-e} = \sum_{i}^{N_n}\sum_{j}^{N_e}\frac{Z_i}{|\mathbf{R}_i - \mathbf{r}_j|},$$

$$\hat{\mathcal{V}}_{e-e} = \sum_{i}^{N_e}\sum_{j>i}^{N_e}\frac{1}{|\mathbf{r}_i - \mathbf{r}_j|}.$$

Where M_i and Z_i are the nuclear mass and charge, respectively. In such a situation, $\mathbf{\Psi}_i$ becomes

$$\mathbf{\Psi}_i = \mathbf{\Psi}_i(\mathbf{r}_1, \ldots, \mathbf{r}_{N_e}, \mathbf{R}_1, \ldots, \mathbf{R}_{N_n}). \tag{2.4}$$

In principle, solving the TISE would grant access to all physical observables through $\mathbf{\Psi}_i$ but, in practice, no analytic solutions exist for the many-body case. Exact numerical solutions, too, are generally unfeasible in the absence of suitable approximations.

2.1.1 The Born-Oppenheimer Approximation

One of the most widely-used approximations in electronic structure theory is the Born-Oppenheimer approximation. This approximation is based on the fact that the nuclei are significantly more massive than the electrons which, in turn, means that the time scale of the motion of the nuclei is significantly longer than the motion of the electrons. Recognising this leads to two important consequences:

1. The mass of the nuclei is far greater than the mass of the electrons, meaning

*In Hartree atomic units the reduced Planck's constant, $\hbar$, the electron mass, m_e, the elementary charge, e, and the Bohr radius, a_0, are all defined as unity such that $\hbar = m_e = e = a_0 = 1$.

that the motion of the nuclei is on a far longer timescale than the motion of the electrons. The nuclei can be treated as stationary compared to the electrons.

2. The electronic and nuclear parts of the wavefunction can be separated.

This result allows us to treat the nuclei as fixed in space whilst we are solving the electronic part of the problem. For each set of nuclear positions, $\mathbf{R}_i$, there will also be a corresponding TISE for the electrons and a corresponding total electronic energy. These energies then define a potential energy surface for the nuclei, as illustrated in Figure 2.1 for the simple one-dimensional case of a hydrogen molecule (H_2).

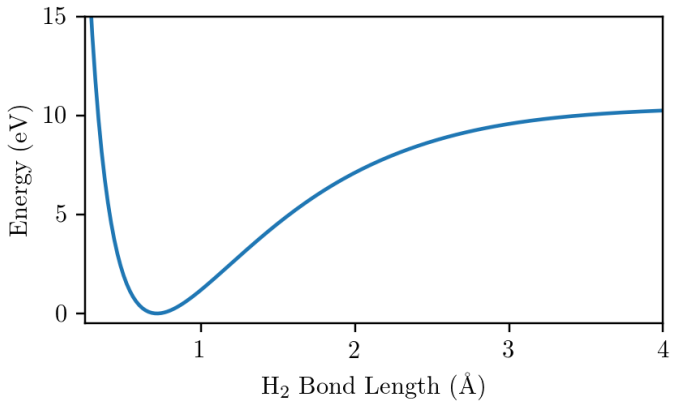

Fig. 2.1. The Born-Oppenheimer potential energy surface associated with varying the bond length in a H_2 molecule, where energies are taken relative to the lowest-energy configuration.

The Born-Oppenheimer approximation effectively allows us to replace

$$\mathbf{\Psi}_i(\mathbf{r}_1, \ldots, \mathbf{r}_{N_e}, \mathbf{R}_1, \ldots, \mathbf{R}_{N_n}) \tag{2.5}$$

with

$$\mathbf{\Psi}_i(\mathbf{r}_1, \ldots, \mathbf{r}_{N_e}). \tag{2.6}$$

The Born-Oppenheimer approximation is used throughout this thesis and, from this point on, all wavefunctions should be assumed to be of the form seen in Equation 2.6. Even with this simplification, the many-body TISE has no analytic solutions. Numerical solutions are possible, but still extremely costly without further approximation, with single-digit numbers of electrons being around the limit of feasibility.

2.1.2 The Exchange Interaction

Electrons are indistinguishable fermions. The Pauli principle states that the wavefunction of a system of identical fermions must be antisymmetric with respect to exchange of particles. If we consider the case of system of two identical particles (such as two electrons with the same spin) then this is equivalent to

$$\boldsymbol{\Psi}(\mathbf{r}_1, \mathbf{r}_2) = -\boldsymbol{\Psi}(\mathbf{r}_2, \mathbf{r}_1). \tag{2.7}$$

In the situation that both identical fermions at the same position, then the wavefunction would have to be

$$\boldsymbol{\Psi}(\mathbf{r}_1, \mathbf{r}_2) = 0 \quad \text{when} \quad \mathbf{r}_1 = \mathbf{r}_2, \tag{2.8}$$

in order to satisfy antisymmetry. This is the Pauli exclusion principle, which states that no two identical fermions can occupy the same quantum state. Any solution for a system of electrons must satisfy this constraint on the wavefunction.

2.2 Hartree-Fock Theory

2.2.1 The Hartree Equations

One of the first proposed approximate solutions to the many-body TISE was the Hartree approximation. Considering again a two particle system, it would be desirable to construct a mathematically convenient ansatz for $\boldsymbol{\Psi}$. One such approach would be to consider $\boldsymbol{\Psi}$ as some combination of orthogonal single-particle wavefunctions, $\phi_i(\mathbf{r}_i)$. A simple representation would be to write $\boldsymbol{\Psi}$ as a product to give

$$\boldsymbol{\Psi}^{\mathrm{H}}(\mathbf{r}_1, \mathbf{r}_2) = \phi_1(\mathbf{r}_1)\phi_2(\mathbf{r}_2), \tag{2.9}$$

where $\boldsymbol{\Psi}^{\mathrm{H}}$ is known as a Hartree product. Then, the Hartree equations takes the form

$$\left(-\frac{1}{2}\nabla_i^2 + \sum_{j\neq i}\int \frac{|\phi_j(\mathbf{r}_j)|^2}{|\mathbf{r}_i - \mathbf{r}_j|}\mathrm{d}\mathbf{r}_j + V_{\mathrm{ext}}(\mathbf{r}_i)\right)\phi_i(\mathbf{r}_i) = \epsilon_i\phi_i(\mathbf{r}_i), \tag{2.10}$$

where ϵ_i are the single-particle energy eigenvalues. The total energy in this approximation is not simply a sum over ϵ_i of the occupied orbitals, but is instead given by

$$E = \sum_{i}^{\text{occ.}} \epsilon_i - E_{\text{H}} \tag{2.11a}$$

$$= \sum_{i}^{\text{occ.}} \epsilon_i - \frac{1}{2} \sum_{i}^{\text{occ.}} \sum_{j \neq i}^{\text{occ.}} \int \int \frac{|\phi_i(\mathbf{r}_i)|^2 |\phi_j(\mathbf{r}_j)|^2}{|\mathbf{r}_i - \mathbf{r}_j|} \mathrm{d}\mathbf{r}_i \mathrm{d}\mathbf{r}_j, \tag{2.11b}$$

where the extra term is known as the Hartree energy, E_{H}, which serves to remove errors implicit within the eigenvalues due to the double counting of electron-electron interactions. The kinetic energy and external potential energy contributions are not double counted and need no such correction.

The Hartree product is tantalisingly simple and reasonably cheap to compute, but the choice of ansatz means that this solution does not satisfy the constraint that the wavefunction be antisymmetric under exchange of particles. This flaw renders the Hartree equations insufficient and a better choice of ansatz is required.

2.2.2 The Hartree-Fock Equations

An improved ansatz could take a properly-normalised, linear combination of $\mathbf{\Psi}^{\text{H}}(\mathbf{r}_1, \mathbf{r}_2)$ and $\mathbf{\Psi}^{\text{H}}(\mathbf{r}_2, \mathbf{r}_1)$ to give

$$\mathbf{\Psi}^{\text{S}}(\mathbf{r}_1, \mathbf{r}_2) = \frac{1}{\sqrt{2}} (\phi_1(\mathbf{r}_1)\phi_2(\mathbf{r}_2) - \phi_1(\mathbf{r}_2)\phi_2(\mathbf{r}_1)) \tag{2.12a}$$

$$= \frac{1}{\sqrt{2}} \begin{vmatrix} \phi_1(\mathbf{r}_1) & \phi_2(\mathbf{r}_1) \\ \phi_1(\mathbf{r}_2) & \phi_2(\mathbf{r}_2) \end{vmatrix}, \tag{2.12b}$$

where $\mathbf{\Psi}^{\text{S}}$ is a Slater determinant. It is clear by inspection that a wavefunction described in this way is antisymmetric under exchange of particles. It is, of course, possible to extend this to a system of N_e electrons as

$$\mathbf{\Psi}^{\text{S}}(\mathbf{r}_1, \ldots, \mathbf{r}_{N_e}) = \frac{1}{\sqrt{N_e!}} \begin{vmatrix} \phi_1(\mathbf{r}_1) & \phi_2(\mathbf{r}_1) & \ldots & \phi_{N_e}(\mathbf{r}_1) \\ \phi_1(\mathbf{r}_2) & \phi_2(\mathbf{r}_2) & \ldots & \phi_{N_e}(\mathbf{r}_2) \\ \vdots & \vdots & \ddots & \vdots \\ \phi_1(\mathbf{r}_{N_e}) & \phi_2(\mathbf{r}_{N_e}) & \ldots & \phi_{N_e}(\mathbf{r}_{N_e}) \end{vmatrix}. \tag{2.13}$$

The elegance in representing the many-body wavefunction in this manner is that, even if we were to make the extreme approximation that electrons are non-interacting, the mathematical form of a Slater determinant is such that the Pauli exclusion principle

would still be satisfied.

Taking a Slater determinant as our ansatz for the solution to the TISE yields the Hartree-Fock (HF) equations which take the form

$$\left(-\frac{1}{2}\nabla_i^2 + \sum_j \int \frac{|\phi_j(\mathbf{r}_j)|^2}{|\mathbf{r}_i - \mathbf{r}_j|}\mathrm{d}\mathbf{r}_j + V_{\text{ext}}(\mathbf{r}_i) - \hat{\mathcal{F}}\right)\phi_i(\mathbf{r}_i) = \epsilon_i\phi_i(\mathbf{r}_i)), \tag{2.14a}$$

$$\hat{\mathcal{F}}\phi_i(\mathbf{r}_i) = \int F(\mathbf{r}_i, \mathbf{r}_j)\phi_i(\mathbf{r}_j)\mathrm{d}\mathbf{r_j}, \tag{2.14b}$$

$$F(\mathbf{r}_i, \mathbf{r}_j) = \sum_j^{\text{occ.}} \frac{\phi_j^*(\mathbf{r}_j)\phi_j(\mathbf{r}_i)}{|\mathbf{r}_i - \mathbf{r}_j|}, \tag{2.14c}$$

where $\hat{\mathcal{F}}$ is known as the Fock operator. The Fock operator and its corresponding effect on the potential is non-local in space (i.e. $V(\mathbf{r}_i, \mathbf{r}_j)$ instead of simply $V(\mathbf{r}_i)$) with the consequence being that each electron in the system feels a different potential that is dependent on $\phi_j(\mathbf{r})$. As with the Hartree approximation, the total energy contains additional terms and is given by

$$E = \sum_i^{\text{occ.}} \epsilon_i - E_{\text{H}} + E_{\text{x}}^{\text{HF}} \tag{2.15a}$$

$$= \sum_i^{\text{occ.}} \epsilon_i - E_{\text{H}} + \frac{1}{2}\sum_i^{\text{occ.}}\sum_j^{\text{occ.}} \int\int \frac{\phi_i^*(\mathbf{r}_j)\phi_j^*(\mathbf{r}_i)\phi_i(\mathbf{r}_i)\phi_j(\mathbf{r}_j)}{|\mathbf{r}_i - \mathbf{r}_j|}\mathrm{d}\mathbf{r}_i\mathrm{d}\mathbf{r}_j, \tag{2.15b}$$

where E_{x}^{HF} is the Fock exchange energy. The HF approximation is significantly more computationally demanding than the Hartree approximation due to the computation of the Fock exchange term, but it is still far cheaper to compute than the exact numerical solution.

2.2.3 Electronic Correlation

The HF approximation performs reasonably well for certain systems but fails quite dramatically in others; a standard example would be the tendency of the HF approximation to predict metals to be insulators. This failure is due to the treatment of electrons as single particles that independently occupy their own lowest-energy states. In reality, an electron will excite surrounding electrons out of this lowest-energy state causing their properties to be correlated. Many materials are considered to be highly-correlated materials in which it is important to capture these correlation effects if we wish to produce reasonable models.

In order to properly describe the fully-correlated nature of the exact ground-state

wavefunction using Slater determinants, it is necessary to calculate the full configuration interaction which is a linear combination of all possible Slater determinants of the system. In practice this must be approximated by truncated the number of configuration states considered. The configuration interaction, alongside other approaches such as the GW approximation or Møller-Plesset perturbation theory, can provide accurate results but are particularly gruelling to compute, even for relatively small systems. A different methodology is required if we wish to consider large numbers of correlated electrons.

2.3 Density Functional Theory

In 1964, Pierre Hohenberg and Walter Kohn published proofs of two important theorems that would lay the groundwork for what would become density functional theory (DFT).[82] The first Hohenberg-Kohn theorem states that the external potential, $V_{\text{ext}}(\mathbf{r})$, is (to within a constant) a unique functional of the electron density, $\rho(\mathbf{r})$; since, in turn, $V_{\text{ext}}(\mathbf{r})$ fixes the Hamiltonian, $\hat{\mathcal{H}}$, we see that the full many-particle ground state is a unique functional of $\rho(\mathbf{r})$. By taking $\rho(\mathbf{r})$ to be a basic variable, the number of spatial coordinates required to describe N electrons has been reduced from $\mathbf{r}_0, \mathbf{r}_1, \ldots, \mathbf{r}_N$ to just $\mathbf{r}$.

Then, the second Hohenberg-Kohn theorem goes on to state that the total energy of a system, $E[\rho]$, is a functional of ρ defined as

$$E[\rho] \equiv F[\rho] + \int V_{\text{ext}}(\mathbf{r})\rho(\mathbf{r})\,\mathrm{d}\mathbf{r}, \tag{2.16}$$

where $F[\rho]$ is a universal functional valid for any number of particles and any V_{ext} and where $E[\rho]$ assumes its minimum value only for the correct value of $\rho(\mathbf{r})$. This means that the ground-state of a system would be trivial to find variationally, assuming that a form for $F[\rho]$ were known. Unfortunately, the exact form of universal functional remains unknown, but there are good enough approximations that density functional theory (DFT) has become the de-facto standard of electronic structure calculations.

2.3.1 The Kohn-Sham Equations

The following year, in 1965, Walter Kohn and Lu Jeu Sham introduced what became one of the most popular formalisms in DFT, known today as the Kohn-Sham (KS) equations.[83] In the KS approach, the system of interacting electrons is replaced by a

fictitious system of non-interacting electrons that reproduce the same density as the real system. In order to reproduce the effects of interaction, a local effective potential is introduced which is referred to as the KS potential, V_{KS}. Then the KS equations, which take a form analogous to the TISE, are defined in atomic units as

$$\left(-\frac{1}{2}\nabla^2 + V_{\mathrm{KS}}(\mathbf{r})\right)\phi_i(\mathbf{r}) = \epsilon_i\phi_i(\mathbf{r}), \tag{2.17}$$

where all $\{\phi_i(\mathbf{r})\}$ feel the same local potential and where the density is given by

$$\rho(\mathbf{r}) = \sum_i^N |\phi_i(\mathbf{r})|^2 . \tag{2.18}$$

The total energy of a KS system is defined as

$$E[\rho] = T_{\mathrm{S}}[\rho] + E_{\mathrm{ext}}[\rho] + E_{\mathrm{H}}[\rho] + E_{\mathrm{xc}}[\rho], \tag{2.19}$$

where T_{S} is the single-particle kinetic energy, E_{H} is the Hartree energy, E_{ext} is the energy associated with the external potential, and E_{xc} is known as the exchange-correlation (XC) energy. The first three terms can be expressed analytically as

$$T_{\mathrm{S}}[\rho] = -\frac{1}{2}\sum_i^N \int \phi_i^*(\mathbf{r})\nabla^2\phi_i(\mathbf{r})\,\mathrm{d}\mathbf{r}, \tag{2.20a}$$

$$E_{\mathrm{ext}}[\rho] = \int \rho(\mathbf{r})V_{\mathrm{ext}}(\mathbf{r})\,\mathrm{d}\mathbf{r}, \tag{2.20b}$$

$$E_{\mathrm{H}}[\rho] = \int\int \frac{\rho(\mathbf{r}_i)\rho(\mathbf{r}_j)}{|\mathbf{r}_i - \mathbf{r}_j|}\,\mathrm{d}\mathbf{r}_i\mathrm{d}\mathbf{r}_j, \tag{2.20c}$$

but these expressions are not exact and instead are the KS approximations to their many-electron counterparts. This means that the exact functional for E_{xc} must act not only as a description of exchange and correlation but also as a description of 'everything else', such that all errors are cancelled. The terms in the effective potential, V_{KS}, can then be calculated from the corresponding energy terms as functional derivatives with respect to the density to give

$$\frac{\delta E_{\mathrm{ext}}}{\delta\rho} = V_{\mathrm{ext}}(\mathbf{r}), \tag{2.21a}$$

$$\frac{\delta E_{\mathrm{H}}}{\delta\rho} = V_{\mathrm{H}}(\mathbf{r}) = \int \frac{\rho(\mathbf{r}_i)}{|\mathbf{r}_i - \mathbf{r}_j|}\,\mathrm{d}\mathbf{r}_i, \tag{2.21b}$$

$$\frac{\delta E_{\mathrm{xc}}}{\delta\rho} = V_{\mathrm{xc}}(\mathbf{r}) \tag{2.21c}$$

which then defines V_{KS} as

$$V_{\mathrm{KS}}(\mathbf{r}) = V_{\mathrm{ext}}(\mathbf{r}) + V_{\mathrm{H}}(\mathbf{r}) + V_{\mathrm{xc}}(\mathbf{r}), \tag{2.22}$$

where the form of $V_{\mathrm{xc}}(\mathbf{r})$ depends on the choice of approximation to E_{xc}.

It is important to emphasise that the analytic expression for $E_{\mathrm{H}}[\rho]$ is an approximation and it is responsible for a large source of error. By inspection it can be seen that the KS DFT form for $E_{\mathrm{H}}[\rho]$ in Equation 2.20c is not equivalent to the true Hartree energy from HF theory in Equation 2.14a. This is due to the fact that, in KS DFT, all of the density interacts with all of the density, meaning that interactions with a single-particle state with itself is erroneously included; this is known as the self-interaction error (SIE) and it remains one of the more challenging problems to consider when constructing approximations to E_{xc}. The SIE has a tendency towards artificially stabilising delocalised states, which can make DFT a poor choice for modelling charge trapping.[84]

2.3.2 Approximations to the Exchange-Correlation Functional

Even though the exact form of $E_{\mathrm{xc}}[\rho]$ is unknown, there are certain properties and constraints that are well-defined which provides an avenue by which to construct approximations. Any approximation to E_{xc} must be a functional of the density, ρ, but there are various approaches.

The Local-Density Approximation

Whilst an analytic form for E_{xc} is unknown for general systems, it is known exactly for the case of the homogeneous electron gas (HEG). Then, a simple approximation is to treat E_{xc} as depending entirely locally on the density. This is known as the local-density approximation (LDA) and it is defined as

$$E_{\mathrm{xc}}^{\mathrm{LDA}}[\rho] = \int \rho(\mathbf{r}) \epsilon_{\mathrm{xc}}^{\mathrm{LDA}}(\rho(\mathbf{r}))\, \mathrm{d}\mathbf{r} \tag{2.23a}$$

$$\frac{\delta E_{\mathrm{xc}}^{\mathrm{LDA}}}{\delta \rho} = V_{\mathrm{xc}}^{\mathrm{LDA}}(\mathbf{r}) = \rho(\mathbf{r}) \epsilon_{\mathrm{xc}}^{\mathrm{LDA}}(\rho(\mathbf{r})) \tag{2.23b}$$

where $\epsilon_{\mathrm{xc}}^{\mathrm{LDA}}(\rho(\mathbf{r}))$ is the exchange-correlation energy per particle in a HEG of density ρ. The exchange part of the LDA is given by

$$\epsilon_{\mathrm{x}}^{\mathrm{LDA}}[\rho(\mathbf{r})] = -\frac{3}{4}\left(\frac{3}{\pi}\rho(\mathbf{r})\right)^{-\frac{1}{3}}, \tag{2.24}$$

which has been determined analytically. The correlation part of the LDA energy density, ϵ_c^{LDA}, is usually fitted to high-accuracy quantum Monte-Carlo calculations and has various forms.

Despite its simplicity, the LDA performs reasonably well in appropriate systems; metals, for example, have a delocalised and almost homogeneous charge density. However, the entirely local dependence causes problems in systems with very inhomogeneous distributions of charge and for isolated systems such as molecules where the density decays to zero far from the ions. In such a case the entirely local dependence means that $\lim_{\rho\to 0} V_{\text{xc}}^{\text{LDA}}(\mathbf{r}) = 0$, which results in the LDA being unable to capture the correct asymptotic behaviour.

Generalised Gradient Approximations

Generalised gradient approximations (GGAs) are a class of approximation that aim to improve on the LDA by also including a dependence on the gradient of the density. The general form of a GGA is

$$E_{\text{xc}}^{\text{GGA}}[\rho] = \int \rho(\mathbf{r})\epsilon_{\text{xc}}^{\text{GGA}}(\rho(\mathbf{r}), \boldsymbol{\nabla}\rho(\mathbf{r}))\,\mathrm{d}\mathbf{r}, \tag{2.25a}$$

$$\epsilon_{\text{xc}}^{\text{GGA}}(\rho(\mathbf{r}), \boldsymbol{\nabla}\rho(\mathbf{r})) = \epsilon_{\text{xc}}^{\text{LDA}}(\rho(\mathbf{r}))\, F_{\text{xc}}(\rho(\mathbf{r}), \boldsymbol{\nabla}\rho(\mathbf{r})), \tag{2.25b}$$

where F_{xc} is an enhancement factor which acts to modify the LDA energy density. As with the LDA, there are various different forms of GGAs, with one of the most popular being the Perdew-Burke-Ernzerhof (PBE) functional.[87]

GGAs are often termed 'semi-local' approximations due to their dependence on a gradient term but, in reality, they are still a local approximation in which all electrons feel the same potential and still suffer from the SIE. GGAs also, generally, exhibit incorrect asymptotic behaviour for V_{xc}. Efforts have been made to construct GGAs with correct asymptotic behaviour,[88] but such functionals approximate V_{xc} directly and there is no guarantee that such an approximation corresponds to a well-defined functional derivative of a corresponding expression for E_{xc} which limits their utility due to their inability to provide a meaningful energy.[89]

Meta-Generalised Gradient Approximations

Meta-generalised gradient approximations (MGGAs) extend on the logic of GGAs by including higher-order derivatives of ρ. Some MGGAs include a very large number of

parameters that are empirically determined and there have been concerns that this loss of physical rigour has actually led to progressively worse MGGAs being constructed as time passes.[90] Nevertheless, other MGGAs focus on satisfying constraints with a modern example being the strongly constrained and appropriately normed (SCAN) functional, which satisfies all known constraints that a MGGA can satisfy[91] and has been shown to perform well for a diverse variety of systems.[92]

2.3.3 The Derivative Discontinuity

In a DFT calculation, the energy gap between the highest-occupied molecular orbital (HOMO) eigenvalue and the lowest-unoccupied molecular orbital (LUMO) eigenvalue will not be equal to the experimental band gap. This is due to a feature known as the derivative discontinuity, Δ_{xc}, which is a uniform shift in the exchange-correlation potential, V_{xc}, that occurs around integer numbers of electrons,

$$V_{\mathrm{xc}}^{N+\delta}(\mathbf{r}) = V_{\mathrm{xc}}^{N-\delta}(\mathbf{r}) + \Delta_{\mathrm{xc}}, \tag{2.26}$$

where δ is an infinitesimal deviation from an integer number of of electrons, N. A uniform scalar shift applied to a potential will give rise to an identical density, but will change the energies of the orbital eigenvalues associated with this density. Therefore the equivalent property for eigenvalues is

$$\epsilon_{N+1}(N+\delta) = \epsilon_{N+1}(N-\delta) + \Delta_{\mathrm{xc}} \tag{2.27}$$

which therefore means that the exact band gap, E_{g}, would be calculated as

$$E_{\mathrm{g}} = \epsilon_{N+1} - \epsilon_N + \Delta_{\mathrm{xc}}. \tag{2.28}$$

These errors in the band gap are not merely an artefact of the approximations made by standard DFT functionals (LDA, PBE, or SCAN, for example), but will occur in any density functional that has a continuous derivative with respect to the number of electrons, even if this functional is otherwise capable of exactly reproducing the ground-state properties of a system.[93] This behaviour is not especially detrimental for metallic systems, which have no gap, but is problematic for semiconducting systems where the band gap is a property of huge technological importance.

2.4 DFT+U

There are several proposed approaches to ameliorating the effects of the SIE and the derivative discontinuity, with one popular method being known as DFT with a Hubbard-like correction (DFT+U),[94] inspired by the older Hubbard model,[95] which utilises an on-site energy term known as U. In DFT+U, an energy penalty is applied to the system when specific orbitals have fractional occupations, where the magnitude of this energy penalty is controlled by the value of U. As U is increased, an increased degree of localisation will be observed in the orbitals to which the U value is being applied. Counteracting some of the SIE by using DFT+U allows for better descriptions of transition metal compounds such as nickel oxide, in which the highly-correlated and highly-localised d-orbitals are decisive in determining band structures, magnetic ordering, and formation energies. Now, the most important consideration is the value that should be chosen for U.

A suitable, physically-meaningful value for U is not always trivial to determine. Sometimes, it may be appropriate to only treat one species in the material with DFT+U; for example, a metal ion where d-orbital localisation or magnetism is important such as or nickel or iron in an oxide or a metal organic framework. In TiO_2, however, it is known that charge can trap on both Ti and O and, as such, a U value may need to be chosen for each element. This problem is not unmanageable for a binary material, but a ternary or quaternary material poses a significantly more challenging problem. Some schemes for determining appropriate U values include linear-response methods,[96] machine-learned fitting to more accurate solutions,[97] and fitting to experimental oxidation energies.[98]

Once a suitable U value has been determined, there is no guarantee that DFT with a Hubbard-like correction (DFT+U) will provide satisfactory results; for example, a U value that correctly allows the formation of localised states may still significantly underestimate the band gap or the dielectric constant of a material.[99,100] It may be possible to alleviate some of these deficiencies with the usage of a more accurate density functional as a starting point for DFT+U; it has been shown that using SCAN+U instead of PBE+U can yield excellent results.[101] Even with a U value that provides excellent results for a given material, the study of dopants would pose an additional problem. If we, for example, wished to study a variety of transition metal dopants in some arbitrary material, then we would then need to go through the arduous process

of optimising a suitable U value for each dopant that we wished to consider. Nevertheless, DFT+U remains a valuable tool due to the fact that it is not appreciably more computationally demanding than pure DFT.

2.5 Hybrid Density Functional Theory*

As highlighted already, DFT and HF are systematically erroneous in opposite manners. Hybrid DFT aims to exploit this by combining both approaches. Hybrid DFT has been shown to yield significantly better results in some cases but, due to the somewhat ad-hoc nature of the approach, care must be taken to ensure the DFT and HF parts have been combined in a sensible and physically meaningful manner.

2.5.1 Linearly-Mixed Functionals

A straightforward example of how a hybrid DFT functional might be constructed is where the hybrid exchange energy takes the form of a simple linear combination

$$E_{\mathrm{xc}}^{\mathrm{PBE}\alpha}(\alpha) = \alpha E_{\mathrm{x}}^{\mathrm{HF}} + (1-\alpha)E_{\mathrm{x}}^{\mathrm{PBE}} + E_{\mathrm{c}}^{\mathrm{PBE}}, \tag{2.29}$$

where $E_{\mathrm{x}}^{\mathrm{HF}}$ is the Fock exchange energy, $E_{\mathrm{x}}^{\mathrm{PBE}}$ and $E_{\mathrm{c}}^{\mathrm{PBE}}$ are, respectively, the exchange and correlation components of the PBE energy functional, and α is the fraction of Fock exchange to be mixed in. This is the form taken by the PBE0 functional, where Görling-Levy perturbation theory is used to show that a value of $\alpha = 0.25$ should be appropriate to describe ionisation and atomisation energies in many systems.[103,104] Taking the same linear form of PBE0 and tuning α in a case-by-case manner leads to class of hybrid DFT functionals that shall be referred to in this work as PBEα, in order to distinguish them from the unique case of PBE0.

2.5.2 Choosing Appropriate Parameters

Functionals such as PBE0 attempt to provide a general-purpose parameterisation, but it must be remembered that neither semilocal DFT nor HF is an exact theory, so there must be no expectation that a simple linear combination of both theories can be applied universally. Instead, a specific value of α may be necessary for a given material which

* This section has been adapted from the introduction of work that has been published: Quirk JA, Lazarov VK, McKenna KP. 'First-Principles Modeling of Oxygen-Deficient Anatase TiO_2 Nanoparticles'. *J. Phys. Chem. C. 2020 Oct 15;124(43):23637-47.*[102]

ideally, should be able to replicate the exact situation as closely as possible (Figure 2.2). If the value of α is too low, then an insufficient amount of SIE will be removed and localized states will not be sufficiently stabilized or, if the value of α is too high, then localized states will become erroneously stable and incorrect predictions may be made. Too high a fraction of Fock exchange also runs the risk of losing some of the desirable features of DFT as, whilst the inclusion of Fock exchange might do well in removing the SIE, it can also introduce potentially dominating amounts static correlation error that are usually comparatively small in standard DFT approximations.[105]

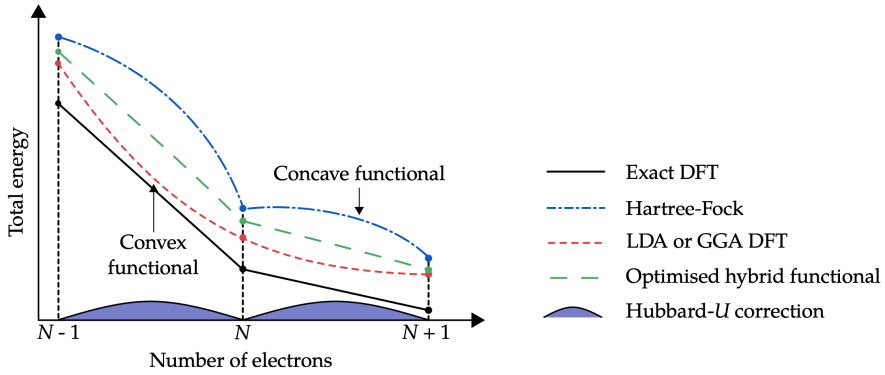

Fig. 2.2. Schematic diagram of the variation of total energy for exact, DFT and HF with the number of electrons. The exact case exhibits piecewise linearity with a discontinuous derivative. DFT has convex behaviour and HF is concave. An optimised hybrid DFT functional would ideally follow the exact line closely. Also shown is the correction that is applied by DFT+U. This figure was created by Razak Elmaslmane for use in his thesis[54] and is licensed under Creative Commons (CC BY-NC-ND 4.0).

When constructing a PBEα functional, it is possible to take an empirical approach by tuning a value of α that reproduces experimental features, commonly the band gap. Such empirical functionals are commonplace and often produce results in good agreement with experiment.[106–108] Empirical functionals do, however, come with limitations in their predictive power due to the fact that they rely on prior knowledge of accurate experimental values which may not be known when studying lesser-known or experimentally-problematic materials. A relevant example would be brookite, a phase of TiO_2, where experimental values for the band gap vary between 3.1 and 3.4 eV.[109] Empirical functionals have a trade-off in terms of universality as there is no real reason to expect that an approximate hybrid functional which gives the correct band gap would also give all other properties of interest correctly. For example, it is observed that functionals tuned to the band gap can still incorrectly predict photoluminescent peaks.[110]

Some non-empirical approaches aim to tune α in order to grant some desirable feature to the PBEα functional. For example, the so-called dielectric dependent hybrid recognizes that hybrid DFT is effectively a further, frequency-independent approximation to the Coulomb hole and screened exchange (COHSEX) approximation to the GW self-energy. It can then be shown that $\alpha = \epsilon^{-1}$ (where ϵ is the dielectric constant) reasonably approximates the COHSEX approximation. More advanced approaches combine linear and range-separated screened components in order to better capture high- and low-frequency components of the dielectric function, which should provide a more accurate model for COHSEX.[111] Dielectric-dependent hybrids generally yield good band gaps and is thought that they should provide good inputs for GW calculations.[112] This approach is not, however, based on some fundamental property of the exact functional but, instead, attempts to use hybrid DFT to approximate a higher-order method. Another approach is to construct a hybrid functional that best reproduces a known property of the exact functional. The choice of constraint can be made based on which constraint is most important to satisfy when studying a particular quantity of interest.

One such property that the exact functional must satisfy is the generalized Koopmans' condition (GKC), which gives an expression for the ionisation energy of a system of an N electrons, $I(N)$, as

$$-I(N) \equiv E(N) - E(N-1) = \epsilon_N(N), \tag{2.30}$$

where $E(N)$ is the total energy of an N electron system, and $\epsilon_i(N)$ is the i-th eigenvalue of the N electron system. Hybrid functionals that have been tuned to satisfy the GKC have been shown to accurately reproduce experimental results for molecular systems[113–115] as well as yielding accurate electron densities in simple model systems where the exact density is known.[86] One drawback is that the GKC is not as applicable to delocalized states, such as band edges in a periodic solid, due to an idiosyncrasy of periodic calculations, which can lead to difficult tuning to the GKC for solid materials.[116] However, in the case of titanium dioxide, the presence of self-trapped polarons provide a convenient localized state against which a functional can be tuned to GKC in the bulk lattice. Previous work in our group constructed GKC-tuned functionals based on polarons in the bulk of various phases of TiO_2.[54,57,86] The value of α that satisfies the GKC for polarons in the bulk of a material will not necessarily satisfy GKC for polarons occurring at surfaces or at grain boundaries. It may be tempting to tune

the value of α case-by-case, but by changing the functional between calculations, the energies of each calculation become incomparable. In the interest of keeping energy differences between calculations meaningful, the value of α optimised for the bulk is employed throughout all calculations in this thesis.

2.6 Practicalities of Calculations

When considering isolated molecules a calculation may only require tens of nuclei and few hundred electrons. An isolated molecule may provide a good description of a material in the gas phase, but condensed matter poses a greater challenge. For context, a relatively small silicon-based device might be around 10×10×10 nm in size and would contain around 55,000 atoms and 767,000 electrons. It is plain that condensed matter systems quickly become unfeasible to model in their entirety. However, many solid-state materials of interest are crystalline and, fortunately, crystals have properties that make them more amenable to computational study.

2.6.1 Periodicity in Crystals

Crystals are highly-ordered materials in which the constituent components (atoms, ions, or molecules) are arranged in patterns that repeat in space. We call the smallest repeating unit of a crystal a unit cell and, for a three-dimensional material, the cell can be described three primitive lattice vectors which we term $\mathbf{a}_1$, $\mathbf{a}_2$, and $\mathbf{a}_3$ and where the magnitude of each of these vectors is equivalent to the length of the unit cell in the corresponding direction. Since a crystal exhibits repeating units with a specific spatial frequency, it is also convenient to define a second set of vectors that span the reciprocal space corresponding to a Fourier transform of the real-space cell (Figure 2.3). The reciprocal lattice vectors ($\mathbf{b}_1$, $\mathbf{b}_2$, and $\mathbf{b}_3$), are defined as

$$\mathbf{b}_1 = 2\pi \frac{\mathbf{a}_2 \times \mathbf{a}_3}{\mathbf{a}_1 \cdot (\mathbf{a}_2 \times \mathbf{a}_3)}, \tag{2.31a}$$

$$\mathbf{b}_2 = 2\pi \frac{\mathbf{a}_3 \times \mathbf{a}_1}{\mathbf{a}_2 \cdot (\mathbf{a}_3 \times \mathbf{a}_1)}, \tag{2.31b}$$

$$\mathbf{b}_3 = 2\pi \frac{\mathbf{a}_1 \times \mathbf{a}_2}{\mathbf{a}_3 \cdot (\mathbf{a}_1 \times \mathbf{a}_2)}. \tag{2.31c}$$

If any point in real space is translated by $\mathbf{R}$ where

$$\mathbf{R} = n_1\mathbf{a}_1 + n_2\mathbf{a}_2 + n_3\mathbf{a}_3, \tag{2.32}$$

and where n_1, n_2, and n_3 are integers, this will yield a symmetrically identical point. There is an equivalent relationship in reciprocal space for a translation $\mathbf{G}$ where

$$\mathbf{G} = n_1\mathbf{b}_1 + n_2\mathbf{b}_2 + n_3\mathbf{b}_3. \tag{2.33}$$

2.6.2 Bloch's Theorem

An infinite crystal contains infinite electrons which would seemingly pose a more difficult problem than the case of a large-but-finite number of electrons, but the periodic nature of a perfect crystal means that only the electrons within the unit cell need to be represented by the wavefunction. Bloch's theorem states that an electron moving in a periodic potential (such as one provided by a crystalline material) can be described by a Bloch wave given by

$$\phi_{n,\mathbf{k}}(\mathbf{r}) = \mathrm{e}^{i\mathbf{k}\cdot\mathbf{r}} u_{n,\mathbf{k}}(\mathbf{r}), \tag{2.34}$$

where $u_{n,\mathbf{k}}$ is a periodic function with the same periodicity as the unit cell, $\mathbf{k}$ is the wavevector and n is the index of the band; keep in mind that, by reducing the problem to a unit cell, we now only need to consider as many bands are required to hold the electrons present in the unit cell rather than requiring infinite bands to contain all the electrons in an infinite crystal. Given that $u_{n,\mathbf{k}}$ has the same periodicity as the unit cell, it is plain that

$$\phi_{n,\mathbf{k}}(\mathbf{r}) = \phi_{n,\mathbf{k}}(\mathbf{r} + \mathbf{R}). \tag{2.35}$$

Similarly, the values of $\mathbf{k}$ are only unique up to a reciprocal lattice vector, $\mathbf{G}$, which means that

$$\phi_{n,\mathbf{k}}(\mathbf{r}) = \phi_{n,(\mathbf{k}+\mathbf{G})}(\mathbf{r}), \tag{2.36}$$

where the set of values of $\mathbf{k}$ that are unique define the first Brillouin zone, and we are free to restrict the considered values of $\mathbf{k}$ to this region of reciprocal space without any loss of generality. Now, if we substitute the form of a Bloch wave (Equation 2.34) in the KS equations (Equation 2.17) we yield

$$\left(-\frac{1}{2}\left(\nabla + i\mathbf{k}\right)^2 + V_{\mathrm{KS}}(\mathbf{r})\right) u_{n,\mathbf{k}}(\mathbf{r}) = \epsilon_n u_{n,\mathbf{k}}(\mathbf{r}). \tag{2.37}$$

When solving this form of the KS equations there are now two considerations that must be made: firstly, the solution to the KS equations now depends on $\mathbf{k}$, and, secondly, a decision would need to be made as to what form $u_{n,\mathbf{k}}(\mathbf{r})$ should take.

2.6.3 k-Point Sampling

The value of **k** that we choose is not arbitrary. As stated previously, the Brillouin zone consists of unique values of **k** that all correspond to unique solutions of Equation 2.37. Various quantities are associated with all unique values of **k** and are calculated as an integral across the Brillouin zone. For example, the density, ρ, can be calculated as

$$\rho(\mathbf{r}) = \frac{\Omega}{(2\pi)^3} \int_{\mathrm{BZ}} \rho_{\mathbf{k}}(\mathbf{r}) \mathrm{d}\mathbf{k}, \tag{2.38a}$$

$$\rho_{\mathbf{k}}(\mathbf{r}) = \sum_{n}^{\mathrm{occ.}} \phi^*_{n,\mathbf{k}}(\mathbf{r}) \phi_{n,\mathbf{k}}(\mathbf{r}), \tag{2.38b}$$

where Ω is the volume of the unit cell. Such integrals are evaluated numerically rather than analytically and, just as we might discretise time and space to integrate various equations, we are free to discretise reciprocal space. A sufficient number of **k**-points must be included in the integration to yield accurate results but, generally speaking, the number of points required is usually rather low as the wavefunctions vary quite slowly across reciprocal space.

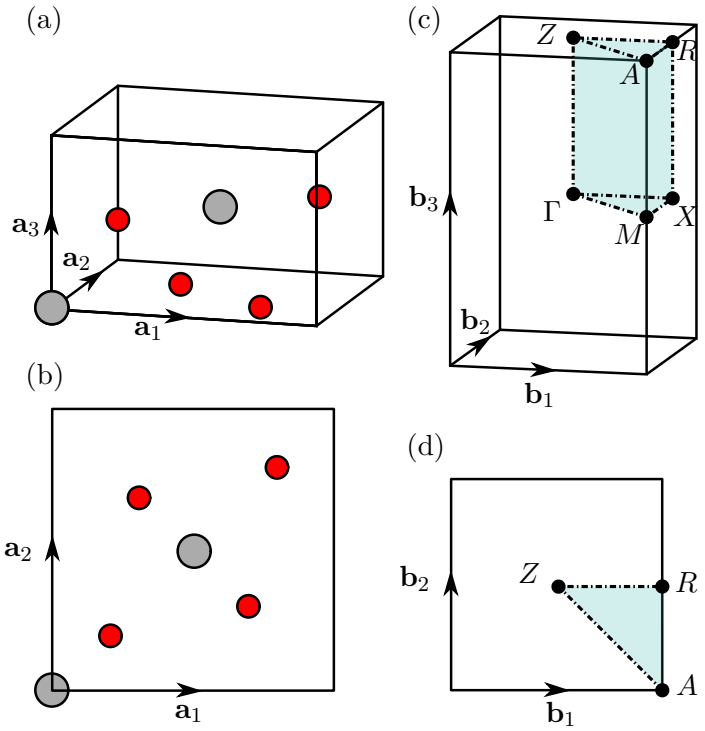

Fig. 2.3. Figure showing (a,b) two projections of the unit cell of rutile in real space where grey circles are titanium and red circles are oxygen and (c,d) corresponding projections of the reciprocal unit cell of rutile, where the special **k**-points have been marked and the shaded blue region indicates the irreducible wedge within reciprocal space.

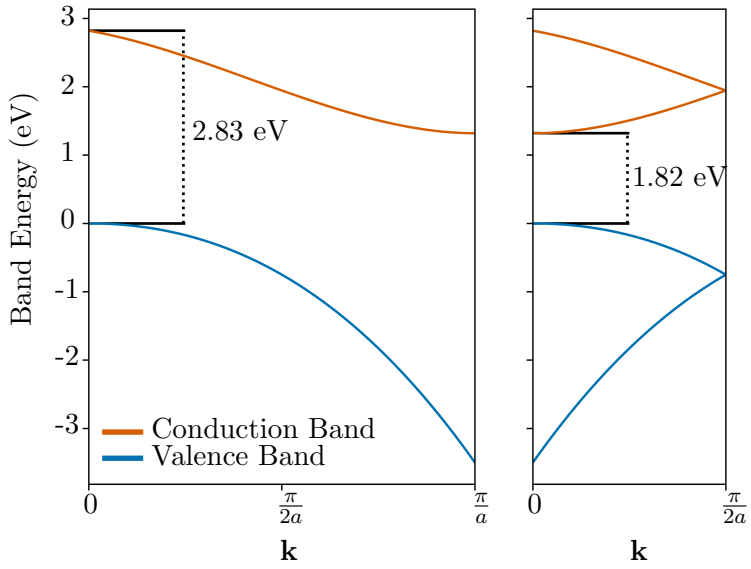

Fig. 2.4. Figures showing (left) an arbitrary band structure with an indirect gap with the direct gap evaluated at **k**=0 being significantly larger and (right) the same band structure folded into a smaller Brillouin zone. Now evaluating the gap at **k**=0 gives the correct value for the gap.

Computational cost can be further reduced by exploiting symmetry operations in reciprocal space, as illustrated in Figure 2.3 through the example of a tetragonal lattice. There are a set of 'special' **k**-points that define the vertices of an irreducible wedge in reciprocal space that has a significantly smaller volume than the actual reciprocal cell; **k**-points must chosen such that they sample the volume inside this wedge, not simply sampling the vertices of the wedge. The special point that is common to all classes of cell symmetry is the Γ-point, which is situated at $\mathbf{k} = (0, 0, 0)$. The Γ-point is a very high-symmetry point and many systems will have a band energy minimum or maximum associated with it. Some systems, such as those with indirect band gaps, may have electronic features associated with special points other than Γ, in which case extra care must be taken when sampling **k**-points.

From the definition of the reciprocal lattice vectors, it can be seen that, as the real-space cell becomes larger, the reciprocal-space cell becomes smaller. Therefore, in the case of a supercell constructed from periodic repeats of the unit cell, fewer **k**-points will be required to achieve the same **k**-point density and level of convergence. Another feature of supercells is that energy bands will be folded into the now-smaller Brillouin zone of the reciprocal supercell. This is illustrated in Figure 2.4, where the folding of the bands is such that one **k**-point alone would now be sufficient to determine the

band gap of a system with an indirect gap. In general, a band structure may not be as convenient as in this illustrative example, so large supercell expansions may be required to fold the **k**-points associated with the valence band maximum (VBM) and conduction band maximum (CBM) onto the Γ-point.

2.6.4 Basis Sets

So far details have been given for neither the form of the periodic function $u_{n,\mathbf{k}}(\mathbf{r})$ in Bloch's theorem, nor for the more general issue of form that should be expected for the single particle orbitals, ϕ_i. The choice of functions to construct the single particle orbitals, and therefore the electron density, are referred to as basis sets and there are two main forms: a linear combination of atomic orbitals, or a plane wave basis.

Linear Combination of Atomic Orbitals

A molecular orbital, ϕ_i, can be expressed as a simple linear combination of atomic orbitals (LCAO) as

$$\phi_i = \sum_n c_{i,n}\chi_n, \tag{2.39}$$

where χ_n are atomic orbitals centered on each of the nuclei and $c_{i,n}$ is a coefficient that weights the contribution of each atomic orbital. The forms of χ_n are generally based on functions that approximate the atomic orbitals of a hydrogen-like atom, which are known analytically. An example are the Slater-type orbitals (STOs), which have a radial component of the form

$$R^{\mathrm{STO}}(r) = Ar^{n-1}e^{-\xi r} \tag{2.40}$$

where A is a normalisation constant, n is the principal quantum number, and ξ is the effective nuclear charge felt by the electron. STOs are a good approximation to atomic orbitals and they correctly satisfy Kato's cusp condition, where the electron density comes to a cusp at the position of the nucleus, but are limited in their usefulness due to being mathematically unwieldy for calculating physical properties. A different approach would be to Gaussian-type orbitals (GTOs) which have the form

$$R^{\mathrm{GTO}}(r) = Ar^{n-1}e^{-\xi r^2}. \tag{2.41}$$

The advantage of GTOs is that the product of two Gaussian functions is another Gaussian function, which is very convenient for the calculation of various properties. The trade-off, however, is that a single GTO describes atomic orbitals very poorly compared to a single STO which means that, in practice, each atomic orbital is expressed as a combination of many GTOs.

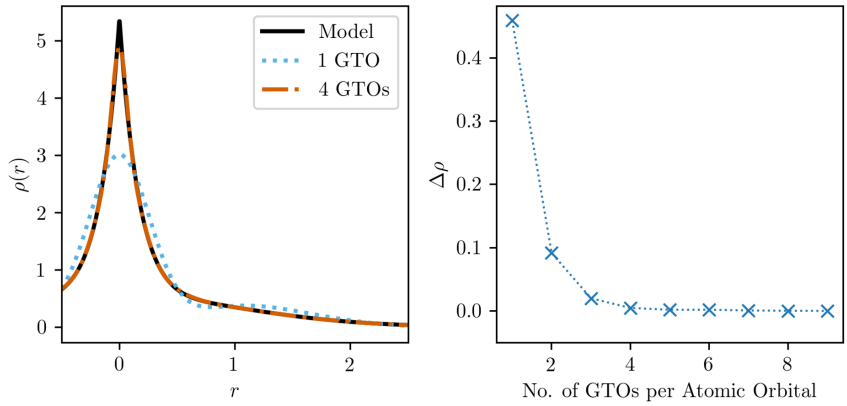

Fig. 2.5. Graphs showing (left) a portion of the densities produced by a minimal GTO basis set containing one and four GTOs and (right) how the error in the density decreases as more GTOs are included. The accuracy is converged at around four GTO functions.

As an illustrative example, Figure 2.5 shows an example density (constructed from two $1s$ STOs and one, more diffuse, $2s$ STO to give something reminiscent of a lithium atom) that has been approximated by optimising a minimal basis set constructed out of a linear combination of GTOs in order to reduce the error in the density, $\Delta\rho = \int \left(\rho_{\text{Exact}}(r) - \rho_{\text{Approx}}(r)\right)^2 \mathrm{d}r$. Whilst one GTO per atomic orbital is quite poor, the basis set quality converges extremely quickly with respect to the number of GTOs. Four GTOs is enough to yield an excellent density that even describes the cusp at the nucleus reasonably well, highlighting the potential for GTO basis sets to enable highly accurate and computationally efficient calculations.

The LCAO approach is not without drawbacks. For a realistic calculation, GTO basis sets need to account for the potentially diverse chemical environments of the atom by including more GTOs and more fitting parameters which leads to GTO basis sets being extremely diverse, with the possibility that the chosen basis set may not be appropriate to describe all situations. Another consideration is that GTO basis sets are usually centered on nuclei which means that it is not possible to model or predict states in which an electron localises off an atom such as in F-center defects or electride

materials,[117–119] without the introduction of a so-called 'ghost' basis set that occupies a site without a nucleus, such as a vacancy or interstitial site. A more general issue that always applies is the basis-set superposition error (BSSE), which refers to an error arising from two basis functions overlapping from nearby atoms. As the nuclei move closer together, their basis functions begin to overlap, effectively increasing the size and quality of the basis in this region. The error can be reduced by using a sufficiently large and well-converged basis.[120]

Plane-Wave Basis Sets

Plane-wave basis sets take a different approach that expresses the periodic part of a Bloch wavefunction, $u_{n,\mathbf{k}}(\mathbf{r})$, as a Fourier series to give

$$u_{n,\mathbf{k}}(\mathbf{r}) = \sqrt{\frac{1}{\Omega}} \sum_{|\mathbf{G}|<G_\mathrm{C}} C_{n,\mathbf{k}}(\mathbf{G}) e^{i\mathbf{G}\cdot\mathbf{r}}, \tag{2.42}$$

where $C_{n,\mathbf{k}}(\mathbf{G})$ are the coefficients of each plane wave, Ω is the volume of the cell, and G_C is a cutoff beyond which the series is truncated. These plane waves are essentially matter waves and, via the Planck relation, they have a corresponding kinetic energy given by $|\mathbf{G}|^2/2$, so usually G_C is given in terms of an energy. Unlike the LCAO basis, a measure of basis set completeness in a plane-wave basis is provided straightforwardly by G_C. Using the same model system, it can be seen (Figure 2.6) that a plane-wave basis converges smoothly as the cutoff energy is increased, with around 70 plane waves being sufficient to provide a reasonable description of the density. Plane-wave basis sets have a

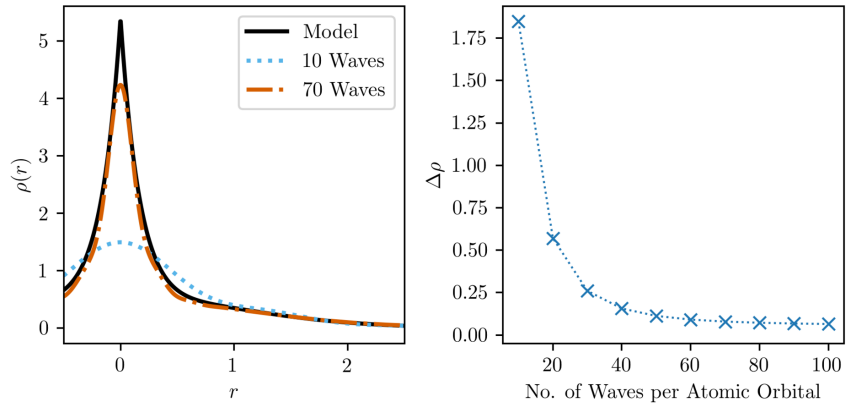

Fig. 2.6. Graphs showing (left) a portion of the densities produced by a plane-wave basis set containing 10 and 70 plane waves and (right) how the error in the density decreases as more plane waves are included. The accuracy is converged once around 70 waves are included.

number of benefits compared to LCAO basis sets. An appealing mathematical feature of plane waves is that their Fourier transform is trivial to compute, making them extremely convenient for working in reciprocal space. Another significant advantage over a LCAO basis is that plane waves uniformly describes all space in the simulation cell and are not centered on atoms, meaning that a plane wave basis can easily describe F-center defects or electride materials, as well as ensuring that there are no concerns regarding changing degrees of basis-set superposition error as atoms (and their associated basis sets) move around the simulation cell during geometry optimisation. A major downside is that a plane-wave basis requires significantly more functions than a LCAO basis, especially in order to describe highly-localised core states. This can make plane wave basis sets too computationally demanding for very large systems containing many hundreds or thousands of atoms.

2.6.5 Pseudopotentials

In an atom, the core electrons near the nucleus are very tightly bound and their charge distribution is not significantly perturbed by the chemical environment that they are in. In principle, it should be possible to eliminate the core electrons from the calculation without significant loss of accuracy, assuming that we can replace the core electrons with something that correctly maintains the behaviour of the valence electrons. In practice, this is achieved through the use of pseudopotentials, where, inside some defined region, the true nuclear potential is replaced by an effective potential and, outside the defined region, the pseudowavefunction and the true, all-electron wavefunction should be identical.

The advantages of employing pseudopotentials are twofold. The first advantage is that the number of electrons involved in the calculation has been lowered, which leads to a reduction in computational cost by reducing the number of bands that need to be considered. The second advantage is that the troublesome localised nature of the core density, and the associated cusp, no longer need to be described by the chosen basis set. This difference is especially stark when using plane waves, as illustrated in Figure 2.7 where it can be seen that excluding the core density from our model atom causes a plane-wave basis to converge considerably more rapidly. It must be remembered, however, that pseudopotentials are not a magic bullet for the computational cost of plane wave basis sets; certain elements, such as a lithium, require highly-localised $1s$ electrons to be treated as valence and may be more amenable to a LCAO approach. Just

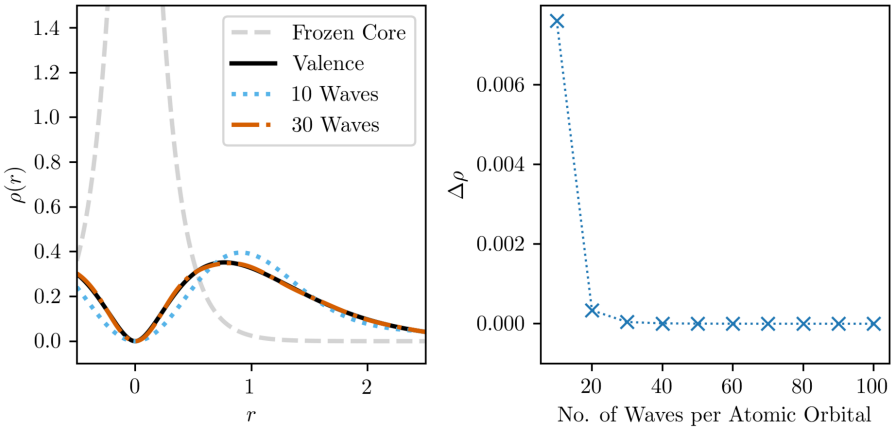

Fig. 2.7. Graphs showing (left) a portion of the densities produced by a plane-wave basis set containing 10 and 30 plane waves and (right) how the error in the density decreases as more plane waves are included. The accuracy is converged once around 30 waves are included. In this example, we are disregarding the core electrons and so far fewer plane waves are needed to reach convergence compared with the all-electron case shown in Figure 2.6

as there are many varieties of basis sets, there are also various types of pseudopotentials.

2.6.6 Geometry Optimisation

Since the introduction of the Born-Oppenheimer approximation in Section 2.1.1 we have considered the atomic positions as only being included in the Hamiltonian by virtue of the external potential they supply. This is perfectly suited to describing electronic structure but, often, the positions of the nuclei will not be known in advance. There are various algorithms that can be used to optimising the position of nuclei and they will usually require the calculation of forces on each of the ions. The force on each i-th ion, $\mathbf{F}_i$, can be calculated using the Hellman-Feynman theorem which states that

$$\mathbf{F}_i = -\frac{\partial E}{\partial \mathbf{R}_i} = -\left\langle \Psi_0 \middle| \frac{\partial \hat{\mathcal{H}}}{\partial \mathbf{R}_i} \middle| \Psi_0 \right\rangle, \tag{2.43}$$

where the ions have effectively been treated as classical particles.

In a unit cell, it can be possible to reduce the forces on atoms to zero while still yielding incorrect lattice parameters. This is due to the fact that the cell may still be under strain even if the forces are zero. This situation can be remedied by calculating the stress tensor. By minimising the stress tensor alongside the forces it is possible to determine the equilibrium shapes of unit cells.

2.7 The CP2K Code

Of the theory discussed so far, there are many different implementations across many different codes. One popular code is CP2K, which is the code that is used throughout the majority of this thesis. CP2K is appealing as it shows good scaling due to various cost-saving techniques.

2.7.1 k-Point Sampling

A major consideration when using CP2K is that it has extremely limited support with regards to **k**-point sampling; in most cases, only the Γ-point can be sampled. This means that, instead of converging the number of **k**-points included in a calculation, the size of the supercell must be increased to provide sufficient **k**-point sampling. This is not especially inconvenient, since we will usually be interested in defective systems which would already require a large supercell. Unfortunately, this limits the utility of CP2K when calculating band structures and density of states. A band structure calculation would require a non-trivial process of unfolding bands from the supercell. Density of states calculations would usually employ much denser **k**-point sampling than would be possible with a supercell calculation sampled only at the Γ-point. This issue can be mitigated by making sure to either only compare density of states plots from supercells with the same dimensions or density of states projected in different regions of the same supercell. In this way, the plots being compared are both equally under-sampled, making it a like-with-like comparison.

2.7.2 Representation of the Density

CP2K uses a Gaussian and plane waves approach where GTOs as described in Section 2.6.4 are used as the primary basis, but an auxiliary basis of plane waves are also used to describe the density. This dual representation of the density allows parts of the calculation to be evaluated more efficiently, for example the Hartree energy is easier to calculate in a plane wave basis than it is in a GTO basis.

2.7.3 Pseudopotentials

CP2K uses the Goedecker-Tetter-Hutter (GTH) pseudopotentials.[121–123] GTH pseudopotentials are norm-conserving pseudopotentials which means that, inside the cutoff

region, each pseudowavefunction is correctly normalised such that it is identical to the all-electron wavefunction.

2.7.4 Implementation of Hybrid Functionals

The implementation of hybrid functionals in CP2K is very efficient and allows for systems containing up to around 1000 atoms to be feasible to model with hybrid DFT. This is possible due to a variety of approximations that are designed to reduce the number of exchange integrals that must be performed. These approximations are designed to have as small an impact on accuracy as possible by only discounting exchange integrals that would have a very small contribution to the total energy.

Auxiliary Density Matrix Method

Similar to the dual-representation of the density, the auxiliary density matrix method (ADMM) employs an auxiliary GTO basis set for the purpose of calculating the Fock exchange integrals. These auxiliary basis sets are smaller than the standard basis and ADMM can significantly reduce the computational cost of hybrid functionals without significant reduction in accuracy, assuming the auxiliary basis has been well-converged. In this thesis, we used ADMM basis sets that contain 9 Gaussian functions for titanium and 7 Gaussian functions for oxygen. A detailed description of the convergence of these basis sets can be found in a previous work from our group.[54,57]

Truncated Coulomb Operator

A further way to reduce the number of integrals that must be computed is through the use of a range-separated functional. In CP2K, this is accomplished with the Coulomb-truncated PBEα (tr-PBEα) functional[124] in which uses a truncated Coulomb operator, u_{tr}, with the form

$$u_{\mathrm{tr}}(\mathbf{r}_i, \mathbf{r}_j) = \begin{cases} \frac{1}{|\mathbf{r}_i - \mathbf{r}_j|}, & \text{if } |\mathbf{r}_i - \mathbf{r}_j| < R_{\mathrm{tr}} \\ 0, & \text{otherwise} \end{cases}, \tag{2.44}$$

where R_{tr} is the truncation radius. Essentially, the long-range contribution to the Coulomb operator is disregarded when calculating Fock exchange. Note that this truncation radius does not apply to the Coulomb operator appearing in the DFT Hartree energy, which is comparatively much cheaper and is calculated as usual. Then, a long-range correction is applied, which calculates the 'missing' exchange at long ranges

using the PBE functional. Then, the tr-PBEα functional exchange-correlation energy, $E_{\mathrm{xc}}^{\mathrm{tr-PBE}\alpha}$, takes the form

$$E_{\mathrm{xc}}^{\mathrm{tr-PBE}\alpha}(\alpha) = \alpha E_{\mathrm{x}}^{\mathrm{tr-HF}} + \alpha E_{\mathrm{x}}^{\mathrm{PBE,LRC}} + (1-\alpha)E_{\mathrm{x}}^{\mathrm{PBE}} + E_{\mathrm{c}}^{\mathrm{PBE}}, \tag{2.45}$$

where $E_{\mathrm{x}}^{\mathrm{tr-HF}}$ is the truncated HF term and $E_{\mathrm{x}}^{\mathrm{PBE,LRC}}$ is the long-range correction term. In the interest of accuracy, the choice of R_{tr} must be sufficiently large that the long-range contributions that are being disregarded are sufficiently small. For $\alpha = 0.25$ and smaller it is found that 6 Å is well-converged with respect to lattice parameters and band gap.

2.7.5 Usage in this Thesis

CP2K is utilised for the vast majority of the calculations with this thesis, which includes all hybrid DFT calculations. For all of our hybrid DFT calculations on anatase, we use a tr-PBEα functional that is tuned to satisfy the GKC as described in Section 2.5.2, where we use a value of $\alpha = 0.105$. This fraction ensures that the GKC is obeyed to within 0.05 eV in bulk anatase.[57,70] This GKC-tuned functional is found to be in good agreement with experiment with regards to polaron formation.[57,86] A detailed description of the optimisation of this tr-PBEα functional for anatase can be found in a previous work from our group.[57,86]

The GTO basis sets used throughout this thesis are the triple-ζ precision molecularly-optimised (MOLOPT) basis sets[125] alongside ADMM basis sets that contain 9 Gaussian functions for titanium and 7 Gaussian functions for oxygen. We use five multigrids with a relative cutoff of 60 Ry and the finest grid having a cutoff of 600 Ry. We find that a 5×5×2 expansion of the conventional anatase unit cell will sufficiently sample reciprocal space to yield lattice parameters of $a = b = 3.78$ Å and $c = 9.61$ Å which are within 1% of experimentally determined parameters. We employ GTH pseudopotentials where the $3s$, $3p$, $3d$, and $4s$ electrons are considered valence for titanium and the $2s$ and $2p$ are considered valence for oxygen. As with our choice of hybrid functional, a detailed description of the convergence of basis sets, supercell size, and energy cutoffs for anatase can be found in a previous work from our group.[54,57] Unless explicitly stated otherwise, all geometry optimisations using CP2K are performed until the force on ions is less than 0.01 eV Å^{-1}.

2.8 The VASP Code

Another popular electronic structure code is the Vienna Ab-Initio Simulation Package (VASP), which differs from CP2K in that it utilises a plane-wave basis to describe the density and also allows to ability to sample reciprocal space with k-points. Large VASP calculations are typically far more computationally-demanding than CP2K calculations, especially for hybrid DFT, though it still serves a useful purpose in this thesis.

2.8.1 Projector Augmented Wave Method

In core-like regions near the nucleus, valence wavefunctions are computationally problematic as they are required to be very rapidly oscillating in order to remain orthogonal to the core states. The projected augmented wave (PAW) method remedies this by describing the real, rapidly-varying physical orbitals, ϕ_i, in terms of a smoothly-varying auxiliary orbital, $\tilde{\phi}_i$, as

$$\phi_i(\mathbf{r}) = \tilde{\phi}_i(\mathbf{r}) + \sum_j \left(\zeta_j(\mathbf{r}) - \tilde{\zeta}_j(\mathbf{r})\right) \left\langle p_j \middle| \tilde{\zeta}_i \right\rangle, \tag{2.46}$$

which requires the definitions of an all-electron basis $\{\zeta_j\}$, a pseudo basis $\{\tilde{\zeta}_j\}$, and a set of projectors p_j.[126] The projectors must satisfy the conditions that

$$\sum_j \left|\tilde{\zeta}_j\right\rangle \langle p_j| = 1, \tag{2.47a}$$

$$\left\langle p_i \middle| \tilde{\zeta}_i \right\rangle = \delta_{ij}, \tag{2.47b}$$

and where Equation 2.46 is only true if

$$\phi_i(\mathbf{r}) = \sum_j \langle p_j|\phi_i\rangle\, \zeta_j(\mathbf{r}) = \sum_j c_{ij}\phi_j(\mathbf{r}), \tag{2.48a}$$

$$\tilde{\phi}_i(\mathbf{r}) = \sum_j \left\langle p_j \middle| \tilde{\phi}_i \right\rangle \tilde{\zeta}_j(\mathbf{r}) = \sum_j c_{ij} \left|\tilde{\phi}_j\right\rangle (\mathbf{r}), \tag{2.48b}$$

which is simply stating that expansion coefficients of the pseudo and all-electron wavefunctions are the same in their respective basis expansions. As with pseudopotentials, in the PAW method space is separated into core-like regions and interstitial regions where, outside the core-like region, $\phi_i(\mathbf{r})$ and $\tilde{\phi}_i(\mathbf{r})$ are identical. The required basis sets, $\{\zeta_j\}$, a pseudo basis $\{\tilde{\zeta}_j\}$, are determined from solutions to isolated atoms.[127]

2.8.2 Usage in this Thesis

Whilst CP2K is very efficient for systems large enough for their reciprocal to be reasonably-described by sampling only at the Γ-point, the major drawback is that it is not sensible to apply it to small systems such as unit cells. VASP, on the other hand, is generally more computationally-demanding, but allows for smaller cells with reciprocal space being sampled with a Monkhorst-Pack grid. In practice, this means that VASP is the natural choice for performing high-throughput calculations on unit cells or on super-cells that are small enough in a given direction that they require more than one k-point for a sensible description. In this thesis, the main purpose of VASP is to determine grain boundary (GB) structures via high-throughput, coarsely-converged geometry optimisations. The details of these calculations shall be described in context in Section 3.3.2).

2.9 Transferability Between Codes

It is important to note that extreme care must be taken when comparing results between codes. Even though all DFT codes have their roots in the same basic theory, the specific implementations are different enough that they may not produce comparable results. For example, differences in pseudopotentials and basis sets may result in a small (but not insignificant) difference in predicted geometric properties such as lattice parameters or electronic properties such as band gaps. In general, this thesis does not use values from VASP in CP2K with the exception of certain quantities that cannot be calculated within the most recent version of CP2K as of the time of writing this thesis. An exception is made for the dielectric constant of anatase as CP2K does not have the ability to directly calculate the dielectric function. Whilst this is not ideal, the usage of a dielectric constant calculated in VASP does not change the nature of any qualitative analysis that is made in this thesis, as shall be made more clear when the relevant theory is discussed in Section 3.4.1.

Chapter 3

Modelling and Analysing Point and Extended Defects

The crystalline systems we have discussed in Chapter 2 have all been, to some degree, limited in how realistic they are, as they consist of infinite, pristine bulk crystals. As acknowledged in Chapter 1, all crystalline materials contain defects. Defects are responsible for a wide array of properties of materials and an understanding of these defects is essential if we wish to engineer a material for a particular application. This chapter outlines the methodology required to produce first-principles models of defect properties in order to provide insight at the atomic scale. First-principles models in the absence of experimental evidence to support the conclusions will always be somewhat speculative and so, to that end, we also discuss producing simulated transmission electron microscopy (TEM) images in order to aid comparison with experiment.

3.1 Point Defects

The simplest defects to consider are point defects. Examples of point defects that are relevant in binary oxides would include: vacancy defects, where a particular atom in the structure is missing; interstitial defects, whereby an atom occupies a site in the lattice where an atom would not normally be found; and substitution defects where a site in the lattice is occupied by an element that it would not normally be occupied by. The charge and location of a defect is often described using Kröger-Vink notation.[128] This notation takes the form X_Y^q where X is the species of the defect, Y refers to the site the defect occupies, and q is the charge of the defect relative to the charge of Y. Traditionally, a net positive, neutral, or negative charge would be denoted with the symbols $^\bullet$, $^\times$, or $'$, respectively, whereas, in this thesis, we elect to use the more familiar numeric superscript for charge. Some examples of Kröger-Vink notation would include:

- Ti^{0}_{Ti} - A titanium atom on a titanium site, with neutral charge.
- Nb^{1+}_{Ti} - A niobium atom on a titanium site, with a single positive charge.
- v^{2+}_{O} - An oxygen vacancy with a double positive charge.
- O^{2-}_{i} - An oxygen on an interstitial site with a double negative charge.
- O^{1+}_{O} - An oxygen on an oxygen site with a single positive charge (a hole polaron).

Point defects in their various charge states are responsible for a wide array of familiar properties of materials. For example, pure corundum aluminium oxide (Al_2O_3) is transparent, but trace quantities of transition metal impurities give corundum the vibrant reds, blues, and other colours that we associate with gem-quality rubies and sapphires.[129] Technologically desirable defects might donate or accept electrons to dope semiconductors to be *n*- or *p*-type, respectively, but undesirable defects may trap charge and lead to non-radiative recombination, reducing the efficiency of optoelectronic devices such as light-emitting diodes or photovoltaic (PV) cells.[130,131]

3.1.1 Modelling Point Defects in Periodic Boundary Conditions

A point defect is 'zero-dimensional' and has no periodicity in any direction and, depending on the material, the concentration of defects can be extremely dilute. We cannot feasibly model a realistically dilute concentration of defects in a periodic supercell as it may require millions of atoms, so instead we settle for simply making the supercell as large as it can be made.[132] Ideally, the supercell would be large enough that the defect does not appreciably interact with its own periodic image, but the specific size of the supercell will generally be constrained by the computational cost of the methods that are being employed.

For a supercell containing some defect, X in a charge state q we can define the formation energy of the defect E_d as

$$E_\mathrm{d}[X^q] = E_\mathrm{tot}[X^q] - E_\mathrm{tot}[\mathrm{Bulk}] - \sum_i \Delta N_i \mu_i + q(E_\mathrm{VBM} + \mu_e) + E_\mathrm{corr.}, \tag{3.1}$$

where $E_\mathrm{tot}[X^q]$ is the total energy of the defective supercell, $E_\mathrm{tot}[\mathrm{Bulk}]$ is the total energy of the pristine, bulk supercell, ΔN_i is the change in the number of the i-th species in the supercell, μ_i is the chemical potential of the i-th species, E_VBM is the energy of the valence band maximum (VBM), μ_e is the chemical potential of electrons which

is typically taken to correspond to the Fermi energy relative to the VBM, E_F, and $E_{corr.}$ are any corrections that need to be applied.[132] Generally, corrections are applied when considering charged defects; the finite size of the supercell leads to a spurious interaction between a charged defect and its periodic image.[133–135] The magnitude of such a correction is inversely proportional to the size of the supercell, so the sort of large anatase TiO_2 supercells that would be employed in `CP2K` correspond to a small correction of less than 0.01 eV.[54] This correction is most important when comparing formation energies of differently-charged defects, but is less important for relative formation energies of similarly-charged defects at different sites in a supercell, where the magnitude of the error should be expected to be the same for all considered defects and so energy differences should be unaffected. The environmental conditions of the material will affect the value the chemical potential of a species, μ_i. For example, oxygen-poor conditions would correspond to a lower value of μ_O and so a lower energy cost to form oxygen vacancies. Similarly, the value of μ_e depends on E_F, which will vary depending on the concentrations of either p- or n-type defects, where the formation energy and therefore concentrations of these defects, in turn, depends on E_F. An accurate approximation of expected equilibrium defect concentrations therefore requires a self-consistent numerical solution.[136]

As we alluded to in Section 2.6.4, care must be taken when calculating defect properties using a linear combination of atomic orbitals (LCAO). A plane-wave basis will populate the entire supercell homogeneously regardless of the contents of the supercell, but an atom-centered Gaussian basis will only sample places where there are atoms. This means that adding and removing point defects is effectively changing the sampling of the basis set throughout the supercell and can cause varying degrees of basis-set superposition error (BSSE) between the pristine supercell and the defective supercell. For a sufficiently high-quality basis set this will not necessarily cause problems but, for peace of mind, it is possible to probe the degree of BSSE in a system using the counterpoise scheme implemented in `CP2K`.[137] Typical values for a well-converged will be less than 0.01 eV which is usually sufficient for solid-state calculations. Even in the absence of BSSE, problems can arise if the charge density associated with a defect is expected to localise off-atom in a region that isn't well-described by the basis, such as in F-center anion vacancies where the charge density localises on the position of the vacant anion. This can be alleviated by adding a ghost atom which has no nuclear potential or charge - but which does have a basis - at the position of the vacancy.[117,118]

3.1.2 Charged Defects

As mentioned in Chapter 1, defects are able to trap charge. An example of charge-trapping in TiO_2 point defect might be a v_O^0 or a v_O^{1+}. Since oxygen in TiO_2 is O^{2-}, a v_O^0 would be the scenario in which two electrons trap in the vicinity of the vacant O^{2-} so that the site is not differently charged compared to the defect-free cell to give $v_O^{2+} + 2\,e^- \longrightarrow v_O^0$. Similarly a v_O^{1+} defect would be the situation where only one electron traps in the vicinity to give $v_O^{2+} + e^- \longrightarrow v_O^{1+}$. If there is no localisation of excess charge, then a significant distortion in the lattice will occur to screen out the effect of the net positive charge of the v_O^{2+}.

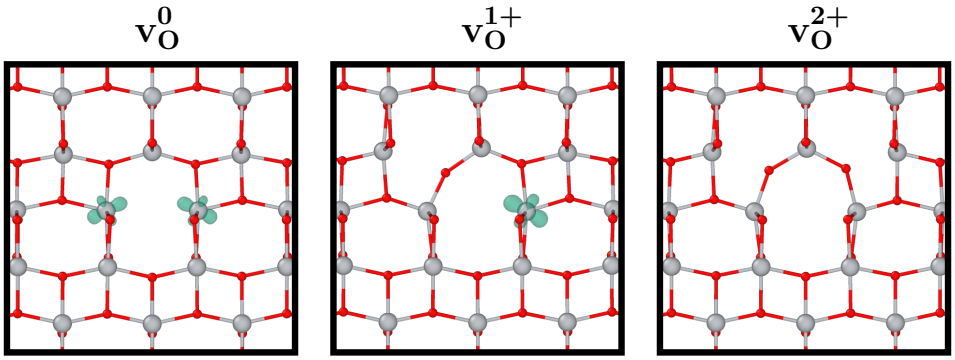

Fig. 3.1. Spin density isosurfaces showing examples of the various charge states that an oxygen vacancy in anatase can take. In the neutral and singly positively charged states (v_O^0 and v_O^{1+}) two electrons and one electron trap, respectively. In the v_O^{2+} no electrons trap. In the case where the defect has a net charge with respect the the site it occupies, a significant distortion to the lattice must occur in order to screen out the effect of this charge.

As long as an appropriate functional is being employed that removes an appropriate amount of the self-interaction error (SIE), successfully converging on these localised configurations is possible. However, it is often the case that the delocalised solution is a local minima, or that the delocalised solution is lower in energy than the localised solution. In such a case, the geometry optimisation procedure may not find the desired localised structure if the initial guess for the geometry is closer to the delocalised configuration than the localised configuration. If there is a desire to examine charge trapping on a specific site (such as to investigate polarons in bulk or to study the relative stability of different trap sites), it is usually sufficient to apply a polaron-like distortion to the lattice such that it will be preferential for charge to localise at specific site. For example, in order to form a O_O^{1+} on a specific O in TiO_2, it is sufficient to break the symmetry by pushing Ti^{4+} ions 0.1 Å radially outwards from the chosen site.

This will provide an initial guess in which a hole localises on the chosen site to form a O^-. The geometry of the system can then be optimised and, if the polaron is stable, the charge will remain localised and a geometry for the O_O^{1+} defect can be determined. For a relatively small supercell, the delocalised configuration is not always entirely realistic as it limits the length scales over which a carrier can delocalise. Nevertheless, comparisons between the energies of the localised geometry, the delocalised geometry, and a series of linearly-interpolated geometries between these configurations can give access to approximations for a wide array of interesting quantities such as defect ionisation barriers or rates of non-radiative recombination.[138,139]

3.1.3 Chemical Potentials

Modelling point defects will almost always require changing the number of a species in the supercell which makes the definition of the chemical potential extremely important. Usually, we are considering particles being added from or removed to some infinite reservoir; this reservoir should represent the species of interest in a physically meaningful context. For example, if we are considering intrinsic defects in metal oxides, the obvious choice of chemical potential for oxygen would be O_2 in the gas phase as would be found in the atmosphere. Then, the reservoir for the metal species in a metal oxide is sometimes taken to be the pure metal. Whilst this would be perfectly reasonable when using a generalised gradient approximation (GGA) or meta-generalised gradient approximation (MGGA), it presents a problem for metal oxides which require hybrid DFT or DFT with a Hubbard-like correction (DFT+U) for an accurate description of their properties, as the pure metal would be badly described by DFT+U or hybrid DFT (as explained in Section 2.5) and so the energetics of the calculated chemical potentials would be dubious.

Sometimes, however, it is possible to define the chemical potential of the metal species in reference to another semiconducting phase that can be well-described by the same hybrid DFT or DFT+U functional. In the case of TiO_2, our procedure is to take the value of μ_O in O-rich conditions to be

$$\mu_O = \frac{1}{2} E_{O_2}, \tag{3.2}$$

where E_{O_2} is the total energy of an oxygen molecule in the gas phase. If we assume that TiO_2 is in equilibrium with the O_2 atmosphere in O-rich conditions, then we can

define the chemical potential of Ti, μ_{Ti}, as

$$\mu_{\mathrm{Ti}} = E_{\mathrm{TiO_2}} - E_{\mathrm{O_2}}. \tag{3.3}$$

For O-poor conditions, we choose the chemical potentials corresponding to anatase in equilibrium with corundum (TiO_2/Ti_2O_3),

$$\mu_{\mathrm{Ti}} + 2\mu_{\mathrm{O}} = E_{\mathrm{TiO_2}} \tag{3.4a}$$

$$2\mu_{\mathrm{Ti}} + 3\mu_{\mathrm{O}} = E_{\mathrm{Ti_2O_3}}, \tag{3.4b}$$

where $E_{\mathrm{Ti_2O_3}}$ is the energy of a unit of bulk corundum. Going from O-rich to O-poor corresponds to a shift in chemical potential of $\Delta\mu_{\mathrm{O}} = -3.96$ eV. The rationale for choosing Ti_2O_3 instead of TiO or metallic Ti is that Ti_2O_3 is the more stable material over a wide range of μ_{O}, which suggests that considering the equilibrium with Ti_2O_3 provides the most meaningful limit on TiO_2 growth.[53,54,140,141]

3.2 Surfaces

A surface occurs where the finite extent of the solid crystal terminates and is replaced by a non-solid medium such as liquid, gas, or vacuum. A surface can be treated as a perfect crystal which has been 'cleaved' along a particular crystallographic plane, where the energy cost associated with cleaving the surface will vary depending on the structure of the crystal.

3.2.1 Modelling Surfaces in Periodic Boundary Conditions

Surfaces are two-dimensional defects. In some ways, it may seem that surfaces are more amenable to periodic treatment than point defects, since a surface is periodic in the two dimensions that lie parallel to the surface, but, in the dimension normal to the surface, the periodicity is broken by vacuum. In practice, a surface must be modelled by a slab of material of finite width, oriented such that each side of the slab exposes the facet of interest (Figure 3.2). Then, the lattice vector of the supercell that is normal to the surface can be varied to increase the amount of vacuum between the slabs. In order for a slab model to be a reasonable model of a surface, the slab must be thick enough that the centre of the slab is roughly bulk-like and the distance between the slabs must be large enough that the slabs do not appreciably interact with one another.[142]

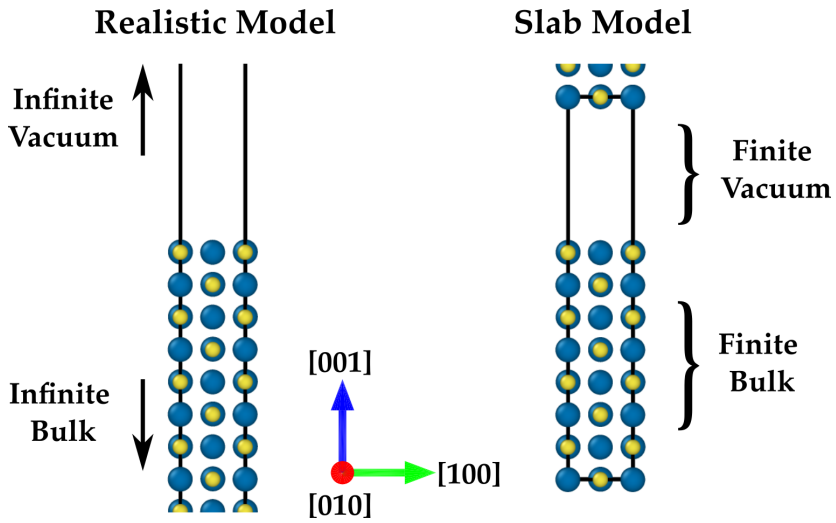

Fig. 3.2. Schematic diagram showing a {001} surface of an arbitrary rock salt structure in the (left) realistic case of effectively infinite vacuum and bulk and the (right) slab model where periodic boundary conditions cause there to be two equivalent surfaces in the cell, separated by finite vacuum. Black lines show periodic boundaries.

The formation energy of a neutral, stoichiometric surface, γ_S, can be calculated using a variation of Equation 3.1 as

$$\gamma_S = \frac{E_{tot}[\text{Surface}] - NE_{tot}[\text{Bulk}]}{2A}, \tag{3.5}$$

where $E_{tot}[\text{Surface}]$ is the energy of a slab model containing N unit equivalents of the bulk material, and A is the cross-sectional area of the slab where the factor of 2 accounts for the two equivalent surfaces in the model. In general, slab models will be made stoichiometric and point defects will be treated in the same way as in bulk. However, there are situations in which surfaces exhibit non-stoichiometry[143] and this should be treated as feature of the surface, rather than simply as large numbers of point defects on a pristine surface. This shall be discussed in more detail in Section 3.4.2.

When optimising the geometry of a surface, none of the cell vectors should be allowed to relax. Allowing the cell vectors parallel to the plane to relax would give a geometry corresponding to an unconstrained film of a finite width, whereas we are attempting to model a surface that has its lattice vectors constrained by the infinite bulk below and so we must fix the cell vectors to that of the bulk. Similarly, the cell vector normal to the surface corresponds to the vacuum and it should not be allowed to relax in order to avoid causing the supercell to fall into an unphysical minima where periodic images of the surfaces are interacting (as well as to avoid the extreme scenario where the vacuum is removed entirely and the slab snaps back together with its periodic image

to form bulk). Whilst the cell vectors are not allowed to relax, the atomic coordinates are, of course, free to move.

3.2.2 Equilibrium Crystals

Thin films grown for the purpose of controlled experiments are often grown through methods such as molecular-beam epitaxy or pulsed laser deposition,[144–147] in which case the facets that are expected to appear are (in the absence of other defects) largely dictated by the orientations in which the material can be grown on the substrate. Crystals produced for industrial purposes, however, might opt for cheaper wet-chemistry methods that grow the nanoparticles in solution, such as the sol-gel process.[19] In this case, the growth is comparatively unconstrained and, given that different facets have different formation energies, it should be expected that the lowest-energy facets will appear in higher quantities. The Wulff construction is a method that determines the equilibrium shape of a particle of fixed volume by minimising the total surface energy of the crystal (Figure 3.3).[148] In this thesis, Wulff constructions are determined using a Python library called `WulffPack`.[149]

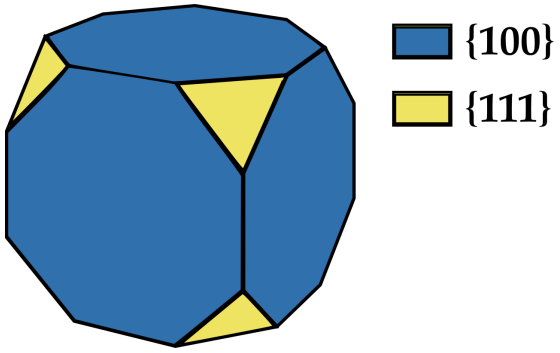

Fig. 3.3. Example of a possible equilibrium crystal morphology of an arbitrary cubic material. The {100} surface has a lower formation energy than the {111} surface, and so the Wulff construction is dominated by {100} facets.

The specific morphology of a crystal can be affected by the conditions in which it is grown. A different chemical environment during growth may stabilise certain surfaces and alter the expected equilibrium crystal. It can also be the case that different growth kinetics or pathways will make a non-equilibrium geometry more favourable. The combination of these factors allows for particles to be tailored to preferentially expose certain facets, or to take on a wide variety of more exotic shapes such as rods, tubes, spheres, or ribbons, in order to improve the suitability of a nanoparticle for a given application.

3.3 Grain Boundaries

In general, a crystalline sample will not be made up of one single crystal (monocrystalline) and will instead contain many differently-sized and differently-oriented grains (polycrystalline), where a grain boundary (GB) refers to the interface between two grains of a crystal. This applies to sintered nanocrystalline samples as well as to thin-films, where grain boundaries (GBs) can nucleate during growth.

3.3.1 Modelling Grain Boundaries in Periodic Boundary Conditions

The GBs presented in this thesis are known as 'tilt' grain boundaries as they involve a rotation (a tilt) about an axis parallel to the grain. A simple, symmetric tilt GB can be described by the crystallographic plane parallel with the GB, $\{hkl\}$, and the axis of rotation, $[mno]$. If the crystallographic lattices of grains of different orientations are overlapped, some number of points in each lattice will overlap with one another. From the proportion of overlapping points, we can define what is known as a Σ value. This concept is somewhat archaic, but it is effectively the reciprocal of the fraction of points that are coincident between the differently oriented grains*, and so gives a convenient indicator of whether a GB is high-symmetry (low Σ) or low-symmetry (high Σ). The notation for a tilt GB rotated about [001] and with the {210} crystallographic plane parallel to the GB plane would be $\Sigma5[001]\{210\}$, or where the rotation axis is omitted for simplicity we would be left with $\Sigma5\{210\}$.

Suppose that we want to model a $\Sigma5\{210\}$ GB. Given that they are also two-dimensional, modelling GBs in a periodic supercell is very similar to the modelling of surfaces in a periodic supercell. The GB is modelled using a supercell containing two differently-oriented slabs (grains) without vacuum separating them, in our example a {210}-oriented slab and its mirror image. Where each grain meets is a GB, meaning that there are two symmetrically-equivalent GBs in the supercell (Figure 3.4).[150,151] The grains should be thick enough to ensure that the centre of the grain is effectively bulk-like and to ensure that there is no interaction between the GBs in the supercell. Given the similarities between modelling surfaces and GBs in a periodic supercell, we can use Equation 3.5 with all the terms referring to the GB instead of referring to a surface.

*In practice this value can simply be calculated as $\Sigma = h^2 + k^2 + l^2$. If this yields an even value for Σ, this implies that a division by two would describe the same periodicity, so divide by two to obtain an odd value for Σ.

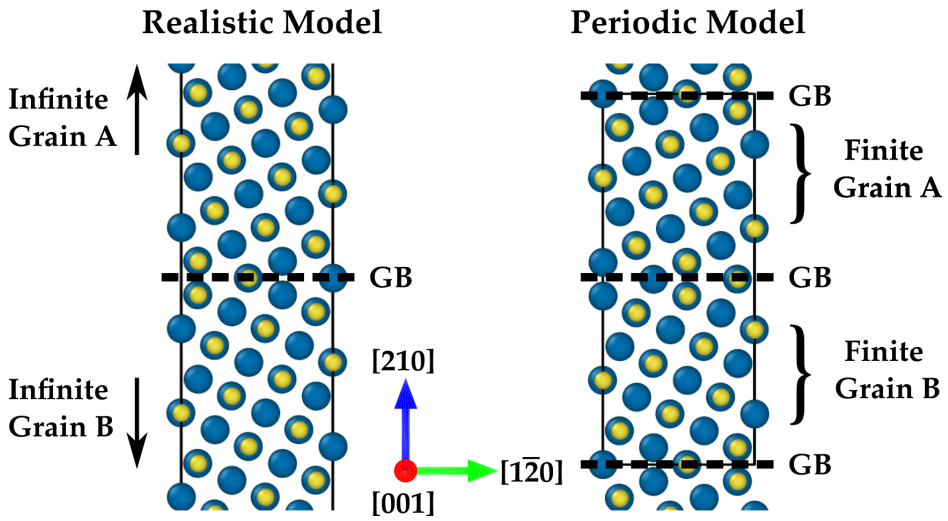

Fig. 3.4. Schematic diagram showing a $\Sigma 5\{210\}$ GB of an arbitrary rock salt structure in the (left) realistic case of effectively infinite grains and the (right) periodic model where periodic boundary conditions cause there to be two equivalent GBs in the cell, separated by finite grains. Thin, solid black lines show periodic boundaries and thick, dashed black lines show GBs

As with surfaces, the cell vectors parallel to the GB plane should not be allowed to relax, in order that the material be constrained to the bulk lattice parameters. However, in GBs the volume of the crystal is generally changed due to the relaxation in the vicinity of the boundary. We can calculate the excess volume per unit area, ΔV, for our GB supercell as

$$\Delta V = \frac{V_{\mathrm{GB}} - N V_{\mathrm{Bulk}}}{2A}, \tag{3.6}$$

where V_{Bulk} is the volume of the bulk unit cell, V_{GB} is the volume of the GB supercell containing the equivalent of N bulk units of the material, and where the cross-sectional area, A, is doubled to account for the two GBs in the cell as with our definition for formation energies.

3.3.2 Determining Stable Grain Boundary Structures

Similar to surfaces, a GB will undergo some relaxation and reconstruction in the vicinity of the boundary plane, but GBs have additional degrees of freedom that must be considered. For a given GB orientation, a translation of one grain with respect to the other will yield a distinct structure, in addition to the usual relaxation and reconstruction that occurs at an extended defect. These translations are referred to as rigid-body translations. There are methods one could employ to determine stable GB structures, such as semi-heuristic approaches that attempt to find a global minimum by sampling

large numbers of configurations through simulated annealing,[152] or algorithms such as random-structure searching.[153] A simpler and computationally cheaper approach is to perform a systematic scan through the rigid-body translations where, at each translation, the geometry of the GB structure is optimised by usual geometry optimisation procedures described in Section 2.6.6.[77,150] This method has previously been successful in predicting experimentally-verifiable GB structures.[154,155]

Regardless of the approach taken, a large number of energy evaluations will be required, with significantly more energy evaluations generally being required for global minimisation schemes. In order to make this screening process feasible, it generally must be carried out using as computationally cheap a method as can be managed whilst still reproducing a sensible energy surface. For some materials, classical force fields are capable of providing a good approximation at very low computational cost but for some materials, such as TiO_2, they tend to fail quite badly. For this reason, the work carried out in this thesis elects to use the Perdew-Burke-Ernzerhof (PBE) functional to perform systematic scans through rigid-body translations which, despite giving a poor description of the electronic structure of TiO_2 compared with hybrid functionals, tends to give a good description of stoichiometric systems where charge localisation is less important.

For all of these high-throughput and coarsely-converged calculations, we calculate energies and forces using the PBE functional as implemented in `VASP`. Whilst `CP2K` is generally a computationally-cheaper code, the speed-up is less significant for standard density functional theory (DFT) than it is for expensive hybrid DFT calculations that are unsuited to high-throughput calculations, so there are times where `VASP` is the cheaper option. To understand why this is the case, consider that, even though the lattice vector normal to the GB plane will always be large, in a high-symmetry GB one or both of the lattice vectors in the directions parallel to the GB plane will typically be small. In such a situation, the Γ-point-only sampling of `CP2K` would require us to build a supercell to achieve sufficient and uniform sampling of reciprocal space, even for a very roughly-converged and cheap calculation. `VASP`, however, allows us to employ k-points which can then be reduced by symmetry in a way that a supercell cannot. For example, a Σ3 boundary in a material with a small unit cell might have lattice vectors normal to the GB plane of around 4 Å and may only require 100 atoms to achieve grains over 20 Å thick. In `CP2K`, we might then have to expand this into a $3 \times 3 \times 1$ supercell with 900 atoms, whereas in `VASP` we may sample reciprocal space with $3 \times 3 \times 1$ k-points,

which could then be reduced by symmetry to just 5 k-points, whilst still retaining the original 100 atoms. Furthermore, even when k-point symmetry does not yield such high returns, we find that `VASP` is generally more stable when compared to `CP2K`, which is more prone to convergence problems when optimising both the electronic and geometric parts of the problem. This makes `VASP` require less hands-on intervention than `CP2K` when tackling some of the difficult-to-converge starting configurations that occur in the rigid-body scans.

We employ projected augmented wave (PAW) pseudopotentials,[127] using the recommended `Ti_pv` pseudopotential which treats the $3s$, $3p$, $3d$, and $4s$ electrons as valence for titanium and the soft `O_s` pseudopotential which treats $2s$ and $2p$ as valence for oxygen. We use a plane wave energy cutoff of 500 eV for all calculations. Monkhorst-Pack grids used to sample reciprocal space vary depending on the supercells being calculated and will be stated in the methods section of the relevant results chapters. Geometry optimisations in high-throughput calculations are performed until the force on ions is less than 0.2 eV Å^{-1}. The standard rules for optimisations of GBs outlined in Section 3.3.1 apply; at each considered translation, all atoms are allowed to relax, the lattice vectors parallel to the GB plane are held fixed, and the lattice vector normal to the to the GB plane is allowed to relax.

3.4 Defect Segregation

Extended defects can induce strain, introduce broken bonds, or alter the electrostatic environment in their vicinity. The combination of these factors leads to the formation energies of point defects being different in the vicinity of a surface or GB compared to in a bulk-like region. For an arbitrary point defect, we can then define a segregation energy to a particular site, $\Delta E_{\mathrm{d},i}$, as

$$\Delta E_{\mathrm{d},i} = E_{\mathrm{d},i} - E_{\mathrm{d},\infty}, \tag{3.7}$$

where $E_{\mathrm{d},i}$ is the formation energy of the defect at site i and $E_{\mathrm{d},\infty}$ is the formation energy of the same defect in a bulk-like region of the crystal. By this definition, if $\Delta E_{\mathrm{d},i}$ is negative then it is more favourable to form this defect at the site of interest than it is to form the defect in a bulk-like region. Assuming that defects do not interact with one another, then the concentration of defects at a site in the vicinity of an extended defect, χ_{i}, can then be related to the concentration of defects in the bulk, χ_{∞}, by the

Langmuir-McClean equation

$$\frac{\chi_i}{1-\chi_i} = \frac{\chi_\infty}{1-\chi_\infty} \exp\left(\frac{-\Delta E_{\mathrm{d},i}}{k_\mathrm{B}T}\right), \tag{3.8}$$

where k_B is the Boltzmann constant, and T should be refer to a temperature at which the defect of interest would be mobile, typically the temperature at which a specimen was annealed rather than the operating temperature of a specimen in a device.

The segregation of defects to surfaces and GBs can have profound effects on the mechanical and electronic properties of a material, which can be beneficial or detrimental. An example of a beneficial effect would be the segregation of chlorine dopants to GBs in cadmium telluride, enhancing current collection in PV applications through the establishment of local $p-n-p$ junctions.[74] A detrimental effect could be the undesirable phase transition occurring at the surface of $LiMn_2O_4$ battery cathodes, driven by high concentrations of oxygen vacancies.[156] Another consideration would be the charge state of the segregated defects. An intrinsically n-type semiconductor such as TiO_2 is effectively self-doped through the presence of oxygen vacancies which, over a wide range of Fermi energies in both rutile and anatase, will preferentially form v_O^{2+} defects where the two excess electrons delocalise into the conduction band.[54] If these vacancies segregate to the boundary where, perhaps, it is more favourable to form v_O^{0} or v_O^{1+} through the localisation or one or more electrons in the vicinity of the defect, then each vacancy contributes fewer mobile charge carriers. However, in the event that carriers introduced by vacancies at the boundary still prefer to delocalise, the segregation of charged defects such as v_O^{2+} to a GB can still affect the performance of a device through the formation of a space-charge region which comes with an associated perturbation to the electrostatic potential.

3.4.1 Defect-Induced Space-Charge Regions

If it is favourable for a charged defect to segregate to a GB, then a higher concentration of defects should be expected at the boundary (Equation 3.8). A high concentration of charged defects will lead to GB region of a crystal having higher degree of net charge than in the bulk of the crystal, which affects the electrostatic environment which, in turn, will affect the formation energy of charged defects. Accounting for varying electrostatic potential, Φ, we can rewrite the Langmuir-McClean equation (Equation

3.8) as

$$\frac{\chi_i}{1-\chi_i} = \frac{\chi_\infty}{1-\chi_\infty} \exp\left(\frac{-(q\Delta\Phi_i + \Delta E_{\mathrm{d},i})}{k_\mathrm{B}T}\right), \tag{3.9}$$

where q is the charge of the defect and $\Delta\Phi_i$ is the electrostatic potential at site i, taken relative to the bulk as

$$\Delta\Phi_i = \Phi_i - \Phi_\infty. \tag{3.10}$$

The space-charge density due to charged defects, ρ_s, is related to the concentration of charged defects by

$$\rho_\mathrm{s} = \sum_i q_i \chi_i, \tag{3.11}$$

which then, in turn, defines the electrostatic potential Φ through the Poisson equation

$$\nabla^2\Phi = \frac{-\rho_\mathrm{s}}{\epsilon\epsilon_0}, \tag{3.12}$$

where ϵ is the relative permittivity of the material and ϵ_0 is the permittivity of free space. Strictly-speaking, because ρ_s is a function of Φ, Equation 3.12 is the Poisson-Boltzmann equation. It is worth mentioning here that the value of ϵ that is used in these calculations comes is calculated in `VASP`, using a PBEα functional with $\alpha = 0.105$. Despite the fact that the hybrid DFT implementations differ between `CP2K` and `VASP`, the value of ϵ only appears as a factor and we make no comparisons between phases and so no qualitative analysis would be changed, even if specific quantities would vary slightly with the use of a hypothetical value of ϵ calculated from `CP2K`.

The development of a space-charge region has serious ramifications for a device. The space-charge potential that develops at a GB poses a barrier to any charge carriers that are conducting normal to the boundary. This is detrimental in, for example, dye-sensitised solar cells (DSSCs) where the carriers injected from the dye must conduct through a sintered network of TiO_2 nanoparticles, where each GB that occurs at the interface between particles has the possibility of forming a significant barrier to transport. In this thesis, Equation 3.12 is solved numerically using the Python package `PySCSES`, which can self-consistently solve the Poisson-Boltzmann for systems containing site-specific defects and segregation energies in arbitrary boundaries.[157]

Space charge potentials are, of course, accessible directly from first-principles calculations and are likely to be more accurate than the comparatively crude one-dimensional approximation made in the Poisson-Boltzmann equation. However, this assumes that one can determine the correction defect concentration that should be expected in the

vicinity of the GB, which is not trivial as it requires the consideration of defect-defect interactions. Even if the correct defect concentration profile is known, achieving the dilute concentrations of defects that might be expected to appear far from the GB would require much larger supercells than are computationally feasible. For this reason, a self-consistent solution to the Poisson-Boltzmann equation remains a valuable tool due to its low computational cost and simplicity.

3.4.2 Highly-Defective Regions

In some cases, point defects may occur in such large quantities in the vicinity of an extended defect that the region deviates significantly from stoichiometry. For example, there is experimental evidence for non-stoichiometry occurring in surfaces, with vacancies occurring at the surface in a periodic, reconstruction-like fashion.[143,158] In such a case, it is no longer reasonable to treat the point defects as dilute and non-interacting defects to a pristine structure. Instead, we should treat the non-stoichiometry as intrinsic feature of the extended defect itself, and reintroduce the chemical potential term to the formation energy to give

$$\gamma_{\mathrm{S}} = \frac{E_{\mathrm{tot}}[\mathrm{Extended}] - NE_{\mathrm{tot}}[\mathrm{Bulk}] - \sum_i \Delta N_i \mu_i}{2A}, \tag{3.13}$$

where $E_{\mathrm{tot}}[\mathrm{Extended}]$ is the total energy of the supercell containing the extended defect which, as before, can be either a surface or GB. Note that, in the case of a GB, we should relax the lattice vector normal to the boundary plane in order to properly model the effects that high defect concentrations will have on the excess volume.

3.5 Simulating Transmission Electron Microscopy Images

Microscopy has played a large role in scientific studies since its inception in the 17th century. A traditional optical microscope employs glass lenses to focus visible light in order to produce very detailed images of tiny structures such as biological cells. Biological cells are, however, orders of magnitude larger than the individual atoms that comprise the nanostructures that we are interested in. The theoretical limit of resolution, d, is given by

$$d = \frac{\lambda}{2n \sin \alpha}, \tag{3.14}$$

where λ is the wavelength of the illuminating beam, n is the refractive index, and α is the half-angle of the cone of the incident illuminating beam. The denominator in this relation is often referred to as the numerical aperture, NA. As an example, visible green light ($\lambda \approx 400$ nm) with a numerical aperture of NA $= 0.2$ would allow for a resolution of $d = 2$ μm. To put this number into context, anatase has experimental lattice vectors of $a = b = 3.78$ Å, and $c = 9.51$ Å,[64] around a factor of 10^4 smaller than the limit posed by using visible light.

Light waves are carried by photons but, of course, all particles have wave-like behaviour. The de Broglie wavelength, λ_{dB}, of a non-relativistic particle is given by

$$\lambda_{\mathrm{dB}} = \frac{h}{p} \tag{3.15}$$

where p is the particle momentum. For example, take a non-relativistic electron with $p = 1.37 \times 10^{-22}$ kgms^{-1} and a corresponding wavelength of $\lambda_{\mathrm{dB}} = 4.84$ pm. Using the same value of NA=0.2 gives a value of $d = 24.2$ pm or 0.242 Å, comfortably in the range of atomic resolution. It is possible to use electrons to produce an image in a way analogous to an optical microscope with a technique called transmission electron microscopy (TEM).

3.5.1 Conventional and Scanning Transmission Electron Microscopy

In conventional transmission electron microscopy (CTEM) (Figure 3.5), the procedure is near identical to conventional light microscopy, where a plane-wave electron beam is shone on a specimen then focused by a lens. Scanning transmission electron microscopy (STEM) differs from CTEM in that it first focuses the beam into a small probe which is then scanned across the specimen so that an image can be built up as a raster (Figure 3.6). The scanning is achieved through the use of specialised coils that deflect the beam towards the region of interest. STEM allows for local properties of a specimen to be probed in greater detail than with CTEM, where parallel beams pass through the specimen in its entirety before focusing.

In TEM, it is possible to produce bright field (BF) and dark field (DF) images. BF describes a situation where only unscattered electrons produce the image, creating bright areas where electrons pass through largely unhindered. DF images are built up only from electrons that have been scattered, meaning that the bright regions of the image correspond to strongly-scattering regions of the specimen. In STEM, these

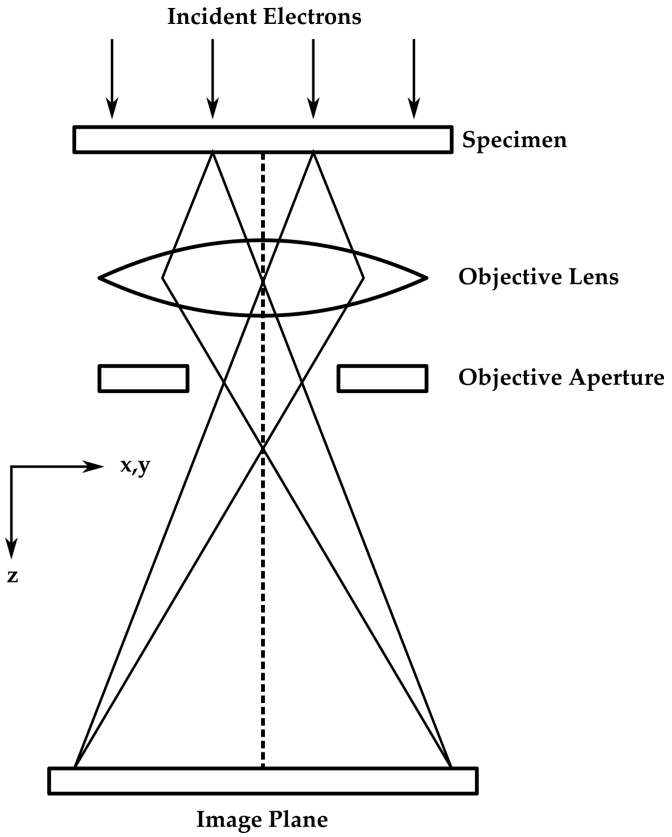

Fig. 3.5. Simple schematic (not to scale) diagram of a CTEM. The condenser and projector lenses at the top and bottom have been ignored.

images can be collected simultaneously using a BF detector and separate, ring-shaped (annular) detector to produce a high-angle annular dark field (HAADF) image. The contrast HAADF images is proportional to Z^2, where Z is the atomic number of the species being imaged. Since heavier elements deflect more strongly, different elements will show up with different bright contrasts in the final image, but generally lighter elements will appear dark. For example, a HAADF image of $SrTiO_3$ may have Sr and Ti show up with clearly different contrasts whilst O would be invisible.[159,160] A middle-ground between the extremes of BF and HAADF is annular bright field (ABF), in which a BF image is created with an annular detector as in HAADF, usually the detector collects electrons in the range of around $\alpha/2$ to α where α is the convergence semi-angle of the electron beam. The benefit of this approach is that it prevents the image becoming over-saturated by the unscattered electrons, allowing species as light hydrogen to be successfully imaged,[161] though generally the difference in contrast between heavier elements is less pronounced. To use the example of $SrTiO_3$ again, an ABF image would make it possible to identify columns of O, but might not allow Sr and Ti to be distinguished from one another.[160]

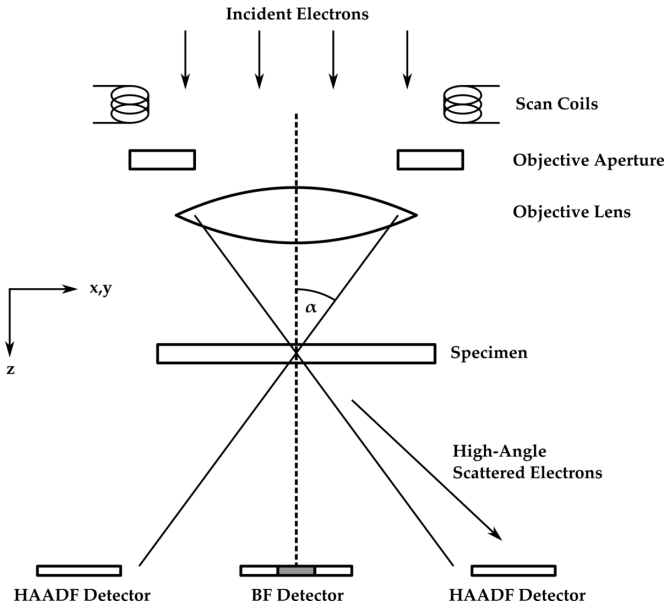

Fig. 3.6. Simple schematic (not to scale) diagram of a STEM. The condenser and projector lenses at the top and bottom have been ignored. The convergence semi-angle is marked as α. The grey shaded area on the BF detector indicates the region which would be discarded in order to produce an ABF image.

3.5.2 Image Aberrations

The assumption of an ideal lens, whether discussing electron optics or light optics, is that lens can focus all incident beams to a single point. In practice, this is never achieved as realistic lenses are imperfect and non-ideal. Deviations from ideal performance are referred to as aberrations. Aberrations are responsible for the blurring and distorting of an image, with the specifics depending on the source of the aberration. The aberrations seen in electron optics are analogous to those that occur in light optics and so share the same names.

In order to limit aberrations, only a small portion of the electron rays near an axis normal to the specimen (the optic axis) are used for imaging, meaning that we can disregard electrons far from the optic axis (the paraxial ray approximation). Assuming that the electron beam is well-aligned with the optic axis, the lowest order aberration we encounter is spherical aberration. This occurs because the fields further away from the optic axis will be stronger, so that electrons with a large angle between their path and the optic axis will be deflected more than is required for proper focus (Figure 3.7). This is referred to as spherical aberration by analogy with a similar process in light optics, where the edge of a spherically-polished lens will tend to be thinner than the center, causing differing degrees of refraction depending on where the light passes

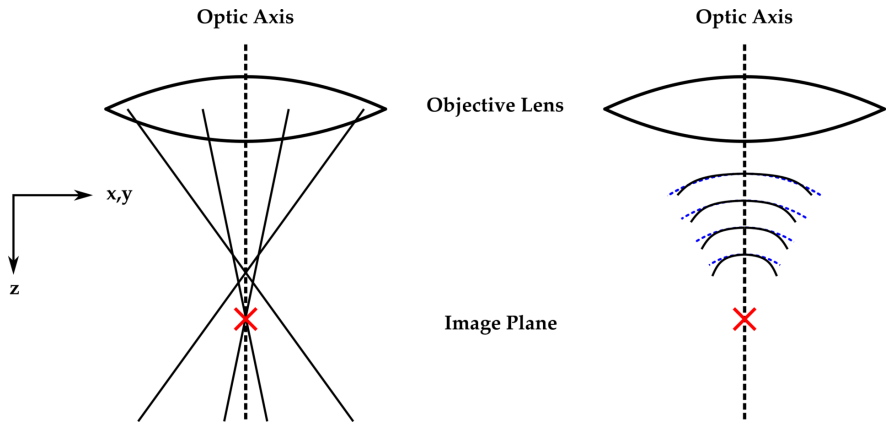

Fig. 3.7. Schematic diagram of demonstrating the effect of spherical aberration of the electron trajectory (left) and on the electron wavefunctions (right). On the right the blue-dotted lines indicate the character of the ideal wavefunction in the absence of spherical aberration. The red cross indicates the ideal focus point. Note that the focal point is different for electron rays close and far from the optic axis.

through the lens.

Spherical aberration is a major limiting factor on the resolution of a TEM image. Modern microscopes are capable of correcting spherical aberration. Even in the absence of dedicated spherical aberration correctors, it is possible to improve an image resolution through the use of intentional defocus. The defocus has some error-cancelling behaviour in combination with spherical aberration, with an 'optimal' defocus as a function of spherical aberration being referred to a Scherzer defocus. In practice, defocus can also be tuned to improve the clarity of specific features within an image.[162]

3.5.3 Multi-Slice Method

Electron microscopy images provide a two-dimensional projection of a three-dimensional structure and, as such, can be difficult to interpret. First-principles modelling can provide insight, but comparing a computer-rendered image of atomic positions with an experimental image is not always straightforward, in part because the experimental image depends strongly on the specific parameters of the microscope and detectors. For this reason, it can be desirable to simulate the TEM image that would correspond to the atomic coordinates determined by the first-principles models. One such method that allows the simulation of TEM images is the multislice method, which shall be described in this section.

The electrons used in TEM are sufficiently energetic that a precise description would require the relativistic Dirac equation. However, a simple approach that yields

a reasonable description is to substitute the relativistic electron mass and wavelength into the non-relativistic time-independent Schrödinger equation (TISE). Then we can write the TISE for this system to be written in Hartree atomic units as

$$\left(-\frac{1}{2\gamma}\nabla^2 - V(\mathbf{r})\right)\Psi_f(\mathbf{r}) = E\Psi_f(\mathbf{r}) \tag{3.16}$$

where $V(\mathbf{r})$ is the nuclear potential due to the specimen, $\gamma = (1 - {}^{v^2}/_{c^2})^{-1/2}$ is the Lorentz factor for an electron with speed v, and $E = \frac{4\pi^2}{2\gamma\lambda}$ is the energy of an electron assuming all processes are elastic. The full wavefunction of the relativistic electron, $\Psi_f(\mathbf{r})$, is described by

$$\Psi_f(\mathbf{r}) = \exp\left(\frac{2\pi i z}{\lambda}\right)\phi(\mathbf{r}), \tag{3.17}$$

where z is the Cartesian direction normal to the sample i.e. in the direction of travel of the wave, and $\phi(\mathbf{r})$ is a factor describing the portion of the wavefunction that varies slowly in z. Given the fact that the incident electrons have very high velocity in z, λ is very small, and $\phi(\mathbf{r})$ varies very slowly in z we can state that

$$\left|\frac{\partial^2\phi}{\partial z^2}\right| \ll \left|\frac{1}{\lambda}\frac{\partial\phi}{\partial z}\right|. \tag{3.18}$$

Now, Equation 3.16 can be simplified through a straightforward but long-winded rearrangement of terms (which shall be omitted in this thesis but which can be easily found in the relevant sources)[163,164] to write an approximate TISE for fast electrons moving in z as a first-order differential equation in z of the form

$$\begin{aligned}\frac{\partial\phi(\mathbf{r})}{\partial z} &= \left(\frac{i\lambda}{4\pi}\nabla^2_{xy} + \frac{2i\gamma\lambda}{4\pi}V(\mathbf{r})\right)\phi(\mathbf{r}) \\ &= \left(\frac{i\lambda}{4\pi}\nabla^2_{xy} + i\sigma V(\mathbf{r})\right)\phi(\mathbf{r}),\end{aligned} \tag{3.19}$$

where $\nabla^2_{xy} = {}^{\partial^2}/_{\partial x^2} + {}^{\partial^2}/_{\partial y^2}$ and $\sigma = {}^{2\gamma\lambda}/_{4\pi}$ is the interaction parameter. This approximate form is referred to as a high-energy approximation or a paraxial approximation to the TISE.

The multi-slice solution to Equation 3.19 opts to break the problem down into small specimen slices. Instead of solving across all z, the problem is integrated from z to $z+\Delta z$, where Δz is the width of a slice. It can then be shown (again, through a lengthy derivation which has been omitted in favour of reference to appropriate sources)[163,164]

that $\phi(\mathbf{r})$ takes the form

$$\phi(x,y,z+\Delta z) = \exp\left(\frac{i\lambda\Delta z}{4\pi}\nabla_{xy}^2\right) t(x,y,z)\phi(x,y,z) + \mathcal{O}(\Delta z^2), \tag{3.20}$$

where $t(x,y,z)$ is the transmission function for the designated slice of the specimen, given by

$$\begin{aligned} t(x,y,z) &= \exp\left(i\sigma\int_z^{z+\Delta z} V(x,y,z')\mathrm{d}z'\right) \\ &= \exp\left(i\sigma V_{\Delta z}(x,y,z)\right), \end{aligned} \tag{3.21}$$

where $V_{\Delta z}$ is the projected potential in the slice. Defining the problem in this way effectively treats the specimen as a series of planes separated by vacuum with a thickness of Δz (Figure 3.8). The errors introduced by the multi-slice method can be reduced through careful placement of slices. Ideally, each slice would contain one plane of atoms such that each slice contains an averaged potential of one atomic plane. Then, the propagation through vacuum would best model the propagation of the electron beam through the interstitial regions between the planes.

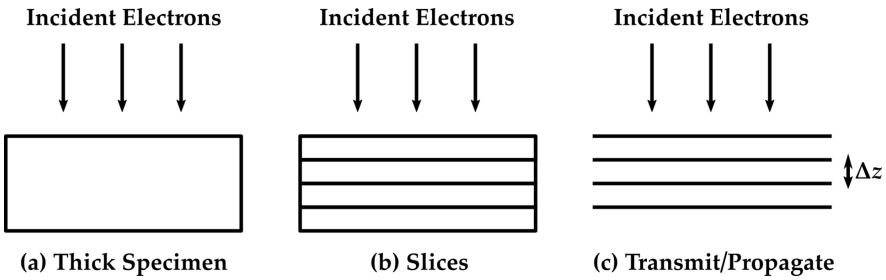

Fig. 3.8. Diagrams showing (a) the full specimen, (b) the specimen separated into thin slices, and (c) how each slice involves transmission through a slice followed by propagation through vacuum of thickness Δz.

In this thesis all multi-slice simulations are carried out using the `QSTEM` code and the `pyQSTEM` library,[163] which grants a high-level interface to provide atomic coordinates directly from the output of `CP2K`, `VASP`, or similar codes. In `pyQSTEM`, all boundaries are assumed to be periodic, which is suitable for the periodic supercells that we employ throughout our studies of GBs. The TEM parameters used throughout this thesis are chosen to be the same as those used by our experimental collaborators in order to ensure that the experimental and simulated images are as comparable as possible.

3.5.4 Scanning Tunnelling Microscopy

Another, tangentially related, method at the nanoscale which is worthwhile considering is scanning tunneling microscopy (STM). This thesis contains relatively little content that directly references STM and so the description given here shall also be kept brief. In STM, a sharp-tipped probe is brought very close to a specimen and slowly scanned across the surface. If a voltage bias is applied between the probe tip and the specimen, then electrons can tunnel from the specimen (i.e. from an occupied electronic state at the surface) to the tip or from the tip to the specimen (i.e. into an unoccupied electronic state at the surface), depending on the direction of the bias. STM is a surface-sensitive technique which allows for high-fidelity probing of both the atomic and electronic structure of a surface which has used to study the structure of surface reconstructions at the anatase {001} surface[165] as well as providing a direct view of charge traps at surfaces of rutile and anatase.[166,167]

Compared to STEM, the simulation of STM is trivial by invoking the Tersoff-Hamann approximation,[168] assuming one has access to a converged result from a first-principles calculation. First, let us assume that the STM tip can be approximated as a spherical probe with the character of an s-orbital. Then, for a given bias voltage, V_B, the tunnelling current through the tip at a given point in space, $\mathbf{r}$, is proportional to the partial electron density in the energy window between E_F and $E_\mathrm{F} + V_\mathrm{B}$ at position $\mathbf{r}$, where E_F is the Fermi energy. By this definition, a negative V_B would correspond to probing the occupied states near E_F whereas a positive V_B would correspond to probing unoccupied states, so long as these states were within V_B of E_F. The data resulting from this approximation is volumetric, but it can be rendered as a two-dimensional image by plotting a cross-section at a fixed height from the surface of interest, or by plotting the height of an isosurface of a chosen value.

Chapter 4

Charge Trapping in {112} and {110} Twin Boundaries in Anatase [†]

4.1 Introduction

As has been established in Chapter 1, the complex and irregular structure of sintered anatase samples poses an extreme challenge to performing detailed and controlled experiments to probe local structure and electronic properties. In Chapters 2 and 3, we outline how first-principles methods can be employed to support experiment by providing insight into the atomic and electronic structure of extended defects. When making predictions, it is important to choose a technologically relevant defect that would be expected to be prevalent in anatase samples because the defect is either kinetically or energetically favourable. Ideally, it would also be possible to probe these defects experimentally in order to confirm any predictions that were made. One such defect is the $\Sigma 3\{112\}$ twin boundary (TB), which is frequently observed in nanocrystalline samples of anatase. Through extensive transmission electron microscopy (TEM) studies, this TB has been identified as forming by the oriented attachment of particles along the minority {112} facets during the hydrothermal coarsening stage of synthesis.[65–67,170] We also identify another TB, the $\Sigma 1\{110\}$ which, whilst not described in the literature, has symmetry such that it could form in thin films of anatase grown epitaxially on [001]-oriented $SrTiO_3$ substrates.

Here we present first principles modelling of the atomic and electronic structure of the $\Sigma 3\{112\}$ and $\Sigma 1\{110\}$ TBs in anatase using the generalized Koopmans' condition (GKC) compliant hybrid DFT functional described in Section 2.7.5 (a PBEα functional

[†]This chapter has been adapted from work which is published: Quirk JA, Lazarov VK, and McKenna KP. "Electronic Properties of {112} and {110} Twin Boundaries in Anatase TiO_2," *Adv. Theory Simul*, vol. 2, no. 12, pp. 1900157, 2019.[169]

with $\alpha = 0.105$) alongside simulated TEM and STM images to aid with comparison to experiment. Both TBs are found to have low formation energies and so are expected to occur frequently, a prediction supported by the experimental evidence of $\Sigma3\{112\}$ TBs in hydrothermally coarsened samples of anatase.[65–67,170] It is found that both TBs alter hole polaron trapping energies - with more favourable traps at the $\Sigma3\{112\}$ TB and less favourable traps at the $\Sigma1\{110\}$ - but neither provides sites for electron trapping nor are new states introduced in the band gap. For this reason, we predict that these TBs will be relatively benign to the electron mobility of anatase used as an *n*-type electrode, but trapped holes if present (for example, due to UV absorption) may lead to increased charge carrier recombination. Similarly, hole traps at internal interfaces could pose problems for photocatalysis as it could prevent charge from being able to effectively migrate to surface sites and facilitate chemical reactions.

4.2 Computational Methods

The TBs are modelled in periodic supercells containing two symmetrically equivalent boundaries as described in Section 3.3.1. A systematic scan through rigid-body translations was performed in `VASP` according to the procedure outlined Section 3.3.2. For the $\Sigma3\{112\}$ TB a supercell of 5.35 Å in the $[\bar{1}10]$ direction, 5.25 Å in the $[\bar{2}\bar{2}2]$ direction, and around 37.4 Å in the [112] direction, with reciprocal space sampled by a Monkhorst-Pack grid of $2 \times 2 \times 1$ in the respective directions. For the $\Sigma1\{110\}$ TB a supercell of 9.61 Å in the [001] direction, 5.36 Å in the $[1\bar{1}0]$ direction, and around 27.1 Å in the [110] direction, with reciprocal space sampled by a Monkhorst-Pack grid of $1 \times 2 \times 1$ in the respective directions. The lowest energy structures yielded by the scan rigid-body translations are taken to be stable structures and are taken forward for further analysis using hybrid DFT as described in Section 2.7.5. In order to achieve good reciprocal space sampling, we use $3 \times 3 \times 1$ and $2 \times 4 \times 1$ expansions of the aforementioned $\Sigma3\{112\}$ and $\Sigma1\{110\}$ supercells, respectively. All TEM simulations are carried out using `QSTEM` as described in Section 3.5. All STM simulations are carried out as described in Section 3.5, where filled and empty states were probed using a bias energy of -2.5 eV and 5.0 eV, respectively. These biases correspond to partial charge densities outputted from `CP2K`, containing all states 2.5 eV below the VBM and 5.0 eV above the VBM, repsectively.

4.3 Results

4.3.1 Atomic Structure and Image Simulation

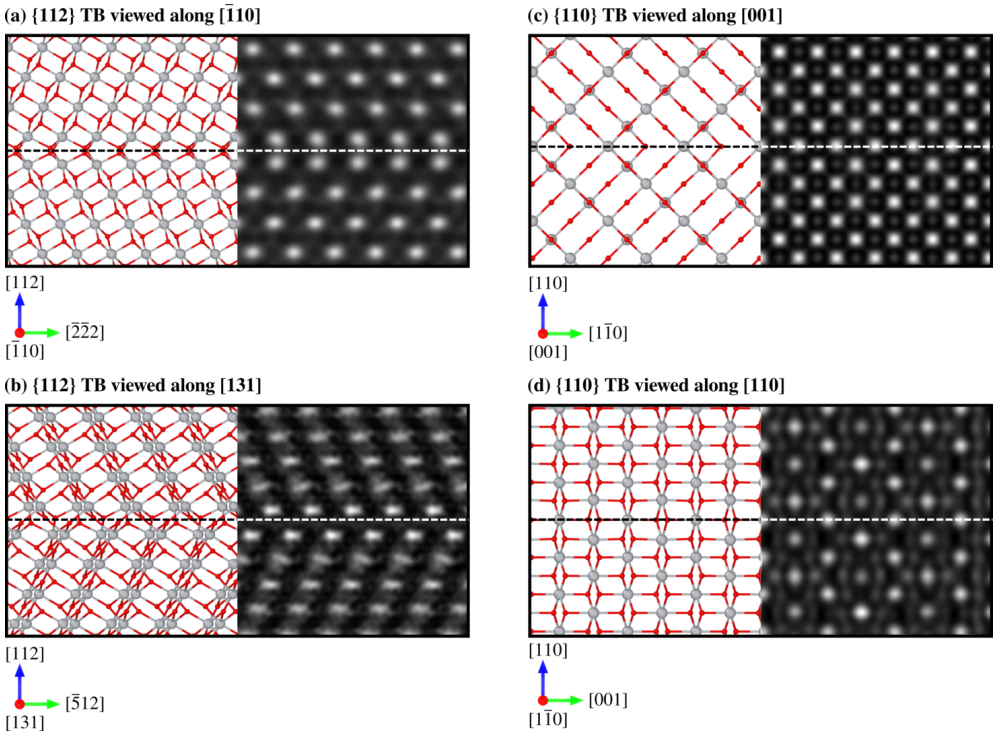

Fig. 4.1. Structure and simulated TEM images for (a) Σ3{112} TB viewed along [110] (-12 nm defocus) and (b) viewed along [131] (10 nm defocus). Structure and simulated TEM images (c) Σ1{110} TB viewed along [001] (2 nm defocus) and (d) viewed along [110] (5 nm defocus). Note that the Σ1{110} TB is invisible to TEM in these projections. Titanium and oxygen ions are represented by gray spheres and red spheres, respectively.

The most stable structures of the Σ3{112} and Σ1{110} TBs were identified by performing a scan of the rigid-body translations between the grains. The Σ3{112} and Σ1{110} have formation energies, γ, of 0.30 Jm^{-2} and 0.34 Jm^{-2} and excess volumes, ΔV, of 0.02 Å and 0.06 Å, respectively. The optimised structures of each TB and simulated TEM images are shown in Figure 4.1. The Σ1 {110} TB adopts a mirror symmetric configuration with no translation between the grains, whereas the Σ3{112} TB has one grain translated by 2.68 Å in the [110] direction. Neither TB imposes significant strain on the lattice; the Σ1{110} TB causes Ti-O bonds to be lengthened by about 1% and the Σ3{112} TB shows no appreciable change in bond lengths. All atoms in both TBs are properly coordinated (i.e. 6-coordinated Ti and 3-coordinated O) with no dangling bonds. Previous theoretical work on anatase surfaces using the

same functional has shown that the presence of under-coordinated Ti sites can allow electrons to self-trap in anatase. Therefore, it could be expected that neither TB is capable of trapping electrons. However, the Σ3{112} TB exhibits local bonding character similar to that of rutile and brookite,[65,66] which might intuitively suggest that its charge-trapping behaviour is more like that of rutile (i.e. able to trap electrons but not trap holes[55,57,166]) than that of anatase. Comparatively, the bonding in the Σ1{110} TB is far closer to that of anatase and it might be expected that its trapping behaviour would be similar to that of bulk anatase. However, as we show below, these naïve assumptions based on structure alone are not correct. The Σ3{112}

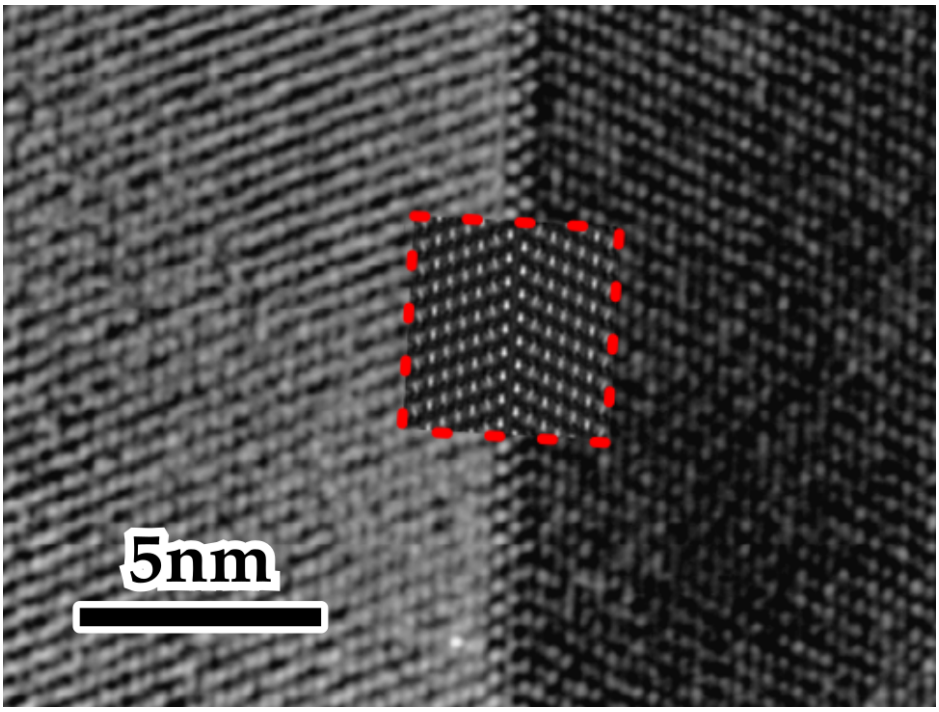

Fig. 4.2. TEM image (adapted with permission from the Mineralogical Society of America from *Formation of Rutile Nuclei at Anatase (112) Twin Interfaces and the Phase Transformation Mechanism in Nanocrystalline Titania.*[65] Copyright 1999.) of a Σ3{112} twinned anatase nanoparticle, viewed down [131]. The inlaid image (red dashed border) is a simulated TEM image, demonstrating close agreement with experiment.

TB has been experimentally observed in samples of hydrothermally coarsened anatase nanoparticles.[65] A simulated TEM image produced from the optimised structure of the Σ3{112} TB viewed along [131] is in extremely good qualitative agreement with an experimental TEM image of a twinned anatase crystal viewed in the same projection (Figure 4.2). The Σ1{110} TB is extremely high-symmetry and undergoes negligible relaxation during geometry optimization, which leads to difficulty in characterisation

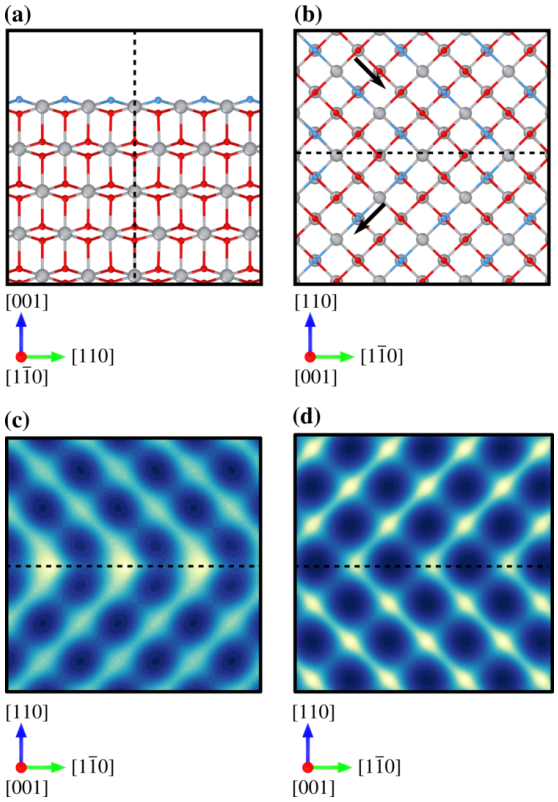

Fig. 4.3. (a) An unreconstructed (001) surface with a $\Sigma 1\{110\}$ TB, viewed along $[1\bar{1}0]$ (b) an unreconstructed (001) surface containing a $\Sigma 1\{110\}$ TB viewed along [001] together with simulated STM images for (c) filled states and (d) empty states. Dashed lines indicate the position of the TB. Titanium and oxygen ions are represented by gray spheres and red spheres, respectively. Characteristic bridging oxygen ions across the surface have been highlighted as blue spheres. Note how the direction of the bonding of the bridging oxygen ions (indicated by arrows) changes direction as the TB is crossed whereas in pristine anatase the direction of the bridging bonds remains unchanged.

with TEM as illustrated by the simulated images. The structure of the $\Sigma 1\{110\}$ TB can be better visualised as a change in the bonding direction of the characteristic 'bridging' oxygens on the (001) surface of anatase, suggesting that surface-sensitive techniques could be better suited to detecting this boundary. We propose that STM would be sufficient to resolve a change of direction in bridging oxygens (Figure 4.3). It is possible to grow thin films of [001] oriented anatase on strontium titanate with a small lattice mismatch between both materials.[171] Given that the $\Sigma 1\{110\}$ boundary involves a 90° rotation about the [001] axis with relatively low strain, we predict that this boundary could occur in epitaxially grown thin films that are constrained to the cubic geometry of the $SrTiO_3$ substrate. Such samples would be suitable for imaging using STM.

4.3.2 Electronic Structure and Trapping

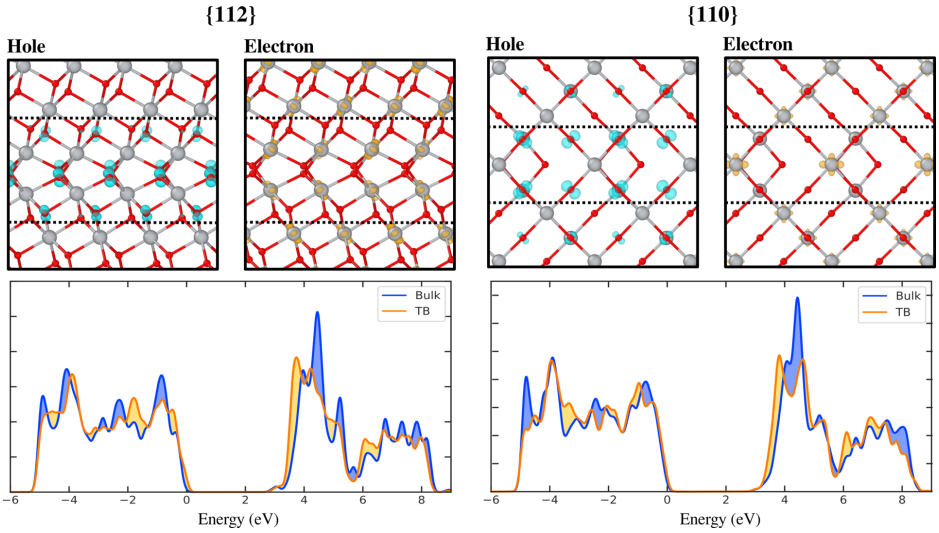

Fig. 4.4. Charge density isosurfaces for vertically added electrons and holes (top) where the area bounded by dashed lines indicates the 'TB region' (isosurface value is 0.005 a_0^{-3}). Also shown is the projected density of states (PDOS) for a charge-neutral system, for the bulk-like region (blue) and the TB region (orange) of the $\Sigma3\{112\}$ (left) and $\Sigma1\{110\}$ (right) supercells. Shaded areas on the PDOS indicate where a region has a greater number of states of a given energy. Titanium and oxygen ions are represented by gray spheres and red spheres, respectively.

For each TB, we calculate the PDOS for atoms in the vicinity of the TB, as well as for the bulk-like region of the grain far from the TB plane (Figure 4.4). With respect to holes, the $\Sigma3\{112\}$ has more states near the VBM in the TB region than in the bulk region which indicates hole trapping behaviour. Conversely, the $\Sigma1\{110\}$ shows that some states move away from the VBM indicating less favourable hole trapping. Both PDOS show that states move down to near the CBM at the TB, which is indicative of electron trapping behaviour. Neither TB alters the band gap or introduces any gap states, which indicates that neither boundary introduces trap states in its equilibrium geometry. To support predictions from the PDOS we produce charge density isosurfaces for electrons and holes added vertically to the TB (i.e. without any geometry optimisation in order to visualise the character of the band edges). It was hoped that the distribution of the band edges across the sites would provide a good predictor of which sites are most favourable for trapping, as a single point calculation with equilibrium geometry is computationally cheaper than performing a geometry optimisation for each site of interest; however, our results indicate that there is no simple correlation between site stability and the band edges. In the $\Sigma3\{112\}$, the charge density isosurface

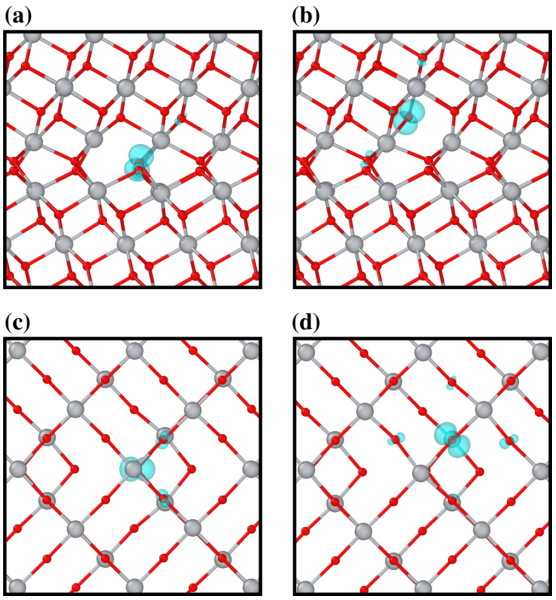

Fig. 4.5. Hole polarons trapped at (a) an O on the Σ3{112} TB, (b) an O adjacent to the Σ3{112} TB, (c) an O on the Σ1{110} TB and, (d) an O directly adjacent to the Σ1{110} TB. The isosurface value is 0.01 a_0^{-3}. Titanium and oxygen ions are represented by gray spheres and red spheres, respectively.

for a vertically added hole shows a strong preference towards O sites in the vicinity of the TB, which is consistent with predictions based on the PDOS. For a vertically added hole in the Σ1{110} we see that the density isosurface avoids O sites directly on the TB plane as expected from the PDOS. There is, however, a small preference towards O sites directly adjacent to the TB, which will correspond to states that are just below the VBM. With regards to electrons, we find that a vertically added electron in the Σ1{110} shows a strong preference towards Ti sites in the TB plane as suggested by the PDOS. However, in the Σ3{112} the density isosurface shows no appreciable preference towards any Ti site, contrary to the PDOS. This can be explained by the fact that the movement of states downwards is not as pronounced in the Σ3{112} as it is in the Σ1{110}.

The above results indicate that these TBs do not significantly perturb the electronic structure of bulk anatase. To assess their impact on polaronic trapping we calculated polaron trapping energies for all symmetrically inequivalent sites in the TB region of each supercell. It was found that neither TB allows the formation of small electron polarons in anatase, which is in agreement with previous theoretical work[57] and experimental evidence indicating that anatase has very high electron mobility.[172,173] Electron trap states at the TB indicated by the PDOS are more likely to be large, diffuse solutions akin to those seen in STM experiments on Nb-doped anatase.[166] Hole

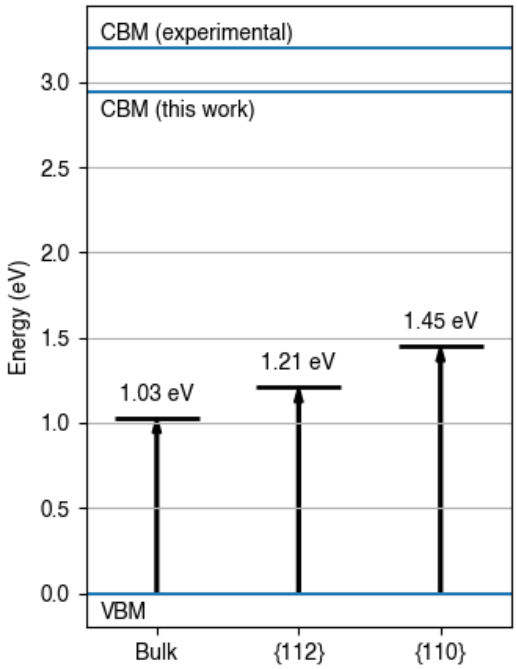

Fig. 4.6. Defect levels of the most stable hole polarons in the bulk-like region, as well as the vicinity of the Σ3{112} and Σ1{110} TBs in anatase TiO_2. The VBM, the theoretical conduction band maximum (CBM) (2.94 eV), and the experimental CBM (3.2 eV) are marked as blue lines.

polarons could be successfully trapped at both sites in the Σ1{110} and two out of three sites in the Σ3{112} (Figure 4.5), with the third site not leading to a delocalised solution but leading to a polaron forming on the nearest TB O. The most stable hole polaron in the Σ{112} TB is shown in Figure 4.5(a), which is 0.178 eV more stable than a bulk-like hole polaron. The most stable hole polaron in the Σ1{110} TB is shown in Figure 4.5(d), which is 0.147 eV more stable than a bulk-like hole polaron.

In spite of the fact that the Σ3{112} TB exhibits rutile-like and brookite-like bonding, it does not mimic either phase with respect to polaron formation. Small electron polarons form in rutile which are not present at the TB. In bulk brookite there are two inequivalent O sites, both of which trap holes, but the relative trapping energies are not consistent with what we find for the TB; the brookite O with the higher polaron trapping energy corresponds to the Σ3{112} with lower trapping energy, and vice versa.[57] The Σ1{110} TB provides a far more favourable site directly adjacent to the boundary, whilst the site on the boundary is slightly less favourable. To provide further insight into the driving force for polaron site preference we analysed strain and electrostatic contributions but could find no clear correlation (see Appendix A), nor do the preferred sites for trapping correlate with the preferred sites of the band edges shown in Figure

4.4. We note that the TBs considered here exhibit no under-coordination and differences in trapping energies are small. This is quite different to the situation in more general extended defects such as surfaces and grain boundaries where correlations between polaron stability and these quantities have been found previously.[174,175] In such a case, much more subtle effects may dictate the stability of polarons and identifying a simple predictive measure of polaron site preference is no longer straightforward.

The polarons modelled in these TBs lead to the presence of a defect level state in the band gap. The defect level of the most stable polaron trapped at each TB is significantly higher than the defect level of a bulk-like polaron (Figure 4.6). We propose that these differences would be possible to probe experimentally using photoluminescence (PL) spectroscopy, where a hole produced by photoabsorption could become self-trapped in the lattice.[176,177] As both TBs present more stable hole polarons than bulk anatase, the expectation is that there would be a higher concentration of polarons at the TB, which could be measured with spatially resolved PL. Furthermore, the defect levels of the TB polarons are higher in energy which would lead to photons emitted by recombination being red-shifted relative to recombination at a bulk-like polaron. The TBs considered in this work are modelled as they would occur in the bulk of the crystal, but it is also possible to probe polaron states at the surface using a scanning probe method such as STM.[166] If a sample of anatase could be produced where a TB terminates at the surface of a film, then a scanning probe method could also be utilised. It should be noted, however, that these polarons near the surface would have modified properties compared to those we have considered.

4.4 Conclusions

The atomic and electronic structure of two TBs in anatase ($\Sigma3\{112\}$ and $\Sigma1\{110\}$) are investigated using a hybrid DFT approach. It was found that the optimised structure of the $\Sigma3\{112\}$ TB was in good agreement with experimental results based on a similarities between the simulated and real TEM images.[65] The predicted structure of the $\Sigma1\{110\}$ TB has very high symmetry, meaning that it would be extremely difficult to observe using methods such as electron microscopy. We propose scanning probe microscopy on (001) oriented anatase (e.g. as grown on $SrTiO_3$ {001}) could resolve this defect, and we provide simulated STM images to aid interpretation of experimental images.

Neither TB exhibits the formation of electron polarons, nor do any states form in the band gap. Due to this, we predict that neither defect would be significantly

problematic when considering anatase as an n-type conductor aside from the increased possibility of recombination due to the higher concentration of trapped holes at the boundary. With regards to photocatalysis, it has been shown in previous studies that holes trapped at anatase surfaces can engage in water-splitting reactions.[49] If holes generated by incident light do not recombine with electrons, they may then become trapped at TB sites far from the surface of the crystal. This will lead to lower numbers of holes available at the surface to interact with adsorbates, thereby lowering the overall reaction rate. Additionally, it must be remembered that both TBs considered in this work are ideal cases with extremely high symmetry, and no dangling bonds or under-coordinated species. The polycrystalline anatase found in a device could have point defects in the vicinity of the TBs, or could have lower symmetry extended defects that might prove to be much more harmful with respect to charge transport. This investigation has provided insight into the formation of polarons in anatase, but more work will be required to fully identify - and learn to counter - more malignant defects that could occur.

Chapter 5

An Experimental and Computational Study of Σ5 Anatase Bicrystals†

5.1 Introduction

The twin boundaries (TBs) described in Chapter 4 did not significantly perturb the electronic structure of anatase, perhaps because they are very high-symmetry and they neither contain broken bonds nor do they impose any significant strain. It may be the case that anatase is not as tolerant towards low-symmetry grain boundaries (GBs), which may introduce trap states. The experimental observation of GBs in polycrystalline samples is not straightforward and essentially relies on serendipity; a GB must present itself in a region of the specimen in which a clean image can be taken, much as we see in the experimental image presented in Figure 4.2. One approach that enables high-quality studies of GBs is the fabrication of a bicrystal. This is accomplished through cleaving large, single crystals along the facets that correspond to the grain-boundary planes of interest. Then, the two cleaved crystals can be rejoined by placing them into contact and annealing at elevated temperatures. The bicrystal approach has been used to successfully elucidate the structures and defect energetics of a wide variety of grain boundaries in oxide materials,[154,179,180] including rutile TiO_2.[181] The poor stability of anatase single crystals makes the standard bicrystal approach for fabricating and imaging GBs[154,179–181] inaccessible for anatase. As an alternative, a well-defined Σ5[001]{310} $SrTiO_3$ bicrystal[154,155,182] is produced from which is cut a suitable substrate onto which an anatase TiO_2 film can be grown epitaxially. The orientation of the

†This chapter has been adapted from work which has just been accepted: Quirk JA, Miao B, Feng B, Kim G, Ohta H, Ikuhara Y, and McKenna KP, "Unveiling the Electronic Structure of Grain Boundaries in Anatase with Electron Microscopy and First-Principles Modelling," Nano Lett., 2021. B. Miao, B. Feng, G. Kim, H. Ohta, and Y. Ikuhara were responsible for all sample fabrication and experimental analysis. All computational work and the writing of the draft manuscript was carried out by myself.[178]

grains in the substrate templates the orientation of the grains in the growing anatase film, which in turn encourages the formation of GBs (Figure 5.1a), giving a means to provide deeper insight into the electronic properties of more general GBs of lower symmetry.

We characterize the $\Sigma5\{310\}$ and the $\Sigma5[33\bar{1}]\{103\}$ GBs (the latter is observed due to the proposed formation of $\{112\}$ twins in the anatase film). Simulated scanning transmission electron microscopy (STEM) images produced from computationally predicted structures are in excellent agreement with experiment. We find that the $\Sigma5[001]\{310\}$ and $\Sigma5[33\bar{1}]\{103\}$ GBs generally only weakly perturb the electronic structure of anatase and should be relatively benign for conductivity. However, segregation of ionized oxygen vacancies is predicted to lead to a space charge region and an inter-grain electrostatic barrier to electron transport of around 0.1 eV. We also predict a highly oxygen-deficient variant of the $\Sigma5[33\bar{1}]\{103\}$ GB that contains large numbers of electron traps in the vicinity of the boundary. This is supported by electron energy loss spectroscopy (EELS) measurements carried out by our collaborators, which show that the region in the vicinity of the $\Sigma5[33\bar{1}]\{103\}$ GB is more reduced than the bulk-like region of the grains. The increased number of electron traps in the vicinity of the GB will lead to decreased carrier mobility and increased rates of recombination, which would be seriously detrimental to the performance in photovoltaics, photocatalysis, and rechargeable battery applications.

5.2 Methods

5.2.1 Experimental Methods

The experimental portion of this study was carried out by our experimental collaborators B. Feng, B. Miao, G. Kim, H. Ohta, and Y. Ikuhara at the University of Tokyo. Experimental details shall be described briefly here to provide context for the chapter.

The $SrTiO_3$ substrates containing $\Sigma5[001]\{310\}$ GB were first fabricated by diffusion bonding of two single crystals at 1500 °C for 10 hours in air (Shinkosha Co. Ltd.). Then they were processed into a substrate and then polished to have a mirror surface. TiO_2 thin films were then deposited by pulsed laser deposition method. The substrates were initially annealed at 700 °C in the deposition chamber with oxygen pressure of 3.0×10^{-3} Pa for 20 min, and then the TiO_2 thin film was deposited. The deposition rate was set to about 2.2 nm min^{-1}. Pure oxygen gas was introduced into the deposition

chamber and then the TiO_2 thin film was cooled down to room temperature. Out-of-plane and in-plane X-ray diffraction patterns suggested that anatase TiO_2 thin film was grown on the $SrTiO_3$ substrate with $[001]SrTiO_3//[001]TiO_2$ epitaxial relationship.

GBs were observed by aberration-corrected STEM (JEM-ARM200CF, JEOL Co Ltd) operated at 200 keV. Annular bright field (ABF) imaging technique was used for atomic scale characterization of GBs. EELS spectra was acquired in STEM mode by an Enfina spectrometer (Gatan Inc). Box scan area for EELS analysis is shown in Figure 5.5d. Integration time is 100s for each measurement, and box scans were carried out for at least three different areas in both bulk and GB. Ti $L_{2,3}$ edge is used for analysis of Ti valence state at both bulk and GB region.

5.2.2 Computational Methods

The GBs are modelled in periodic supercells containing two symmetrically equivalent boundaries as described in Section 3.3.1. A systematic scan through rigid-body translations was performed in `VASP` according to the procedure outlined Section 3.3.2. We use grains with widths of 17.39 Å and 23.87 Å for the $\Sigma5\{310\}$ and $\Sigma5\{103\}$ GB models, respectively. The rigid-body translation supercells used for the $\Sigma5\{310\}$ GB had lattice vectors corresponding to 12.00 Å and 9.62 Å in the $[1\bar{3}0]$ and [001] directions, respectively, and the supercells used for the $\Sigma5\{103\}$ GBs had lattice vectors corresponding to 9.37 Å and 3.79 Å in the $[33\bar{1}]$ and [010] directions, respectively. Reciprocal space sampled by a Monkhorst-Pack grids of $1\times1\times1$ and $1\times2\times1$ for the $\Sigma5\{310\}$ GB and $\Sigma5\{103\}$ GB supercells, respectively. The lowest energy structures yielded by the scan rigid-body translations are taken to be stable structures and are taken forward for further analysis using hybrid DFT as described in Section 2.7.5. In order to achieve good reciprocal space sampling, we use $1\times2\times1$ and $2\times4\times1$ expansions of the aforementioned $\Sigma5\{310\}$ and $\Sigma5\{103\}$ supercells, respectively. The convergence semiangle used in the STEM simulations was set to 22°, where ABF images were produced using electrons collected in the range 11° to 22°. Space charge barriers were calculated from segregation energies using the `PySCSES` code.[157]

5.3 Results and Discussion

Two distinct GB orientations are observed in the ABF STEM images of the anatase bicrystal. The GB structures are shown in Figs. 5.1b-d, where the dark contrast cor-

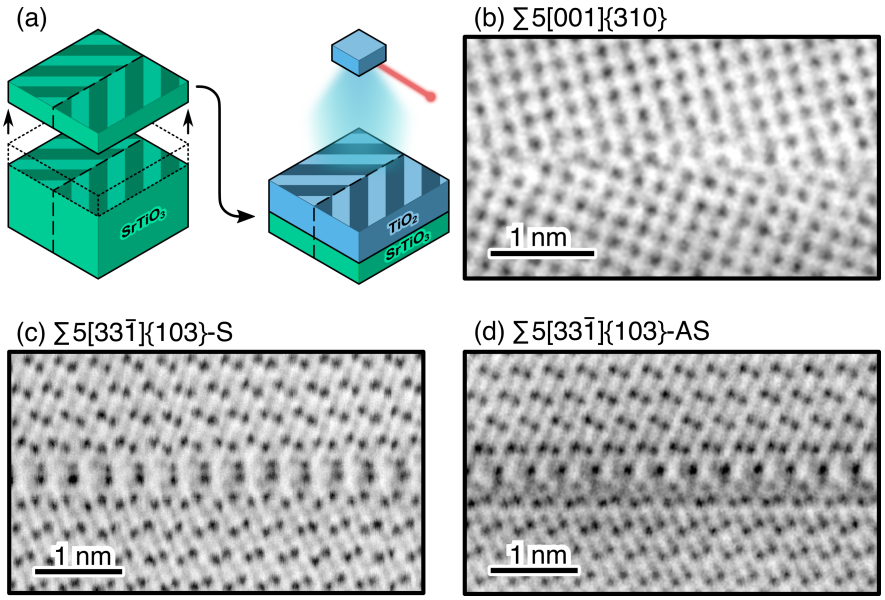

Fig. 5.1. (a) Schematic diagram showing how a slice of an $SrTiO_3$ bicrystal is used as a substrate for the growth of anatase by pulsed laser deposition. The orientation of the anatase grains are templated by the orientation of the grains in the substrate. ABF STEM images of the (b) $\Sigma5[001]\{310\}$ GB, (c) $\Sigma5[33\bar{1}]\{103\}$-S GB, and (d) $\Sigma5[33\bar{1}]\{103\}$-AS GB.

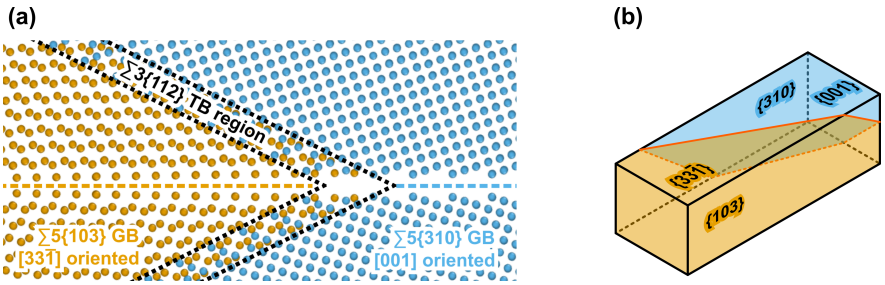

Fig. 5.2. (a) Schematic diagram demonstrating how the presence of a $\Sigma3\{112\}$ twin boundary would account for the observed GBs in the observed projections. (b) Schematic diagram of one grain of the bicrystal with the presence of a $\Sigma3\{112\}$ twin boundary imposing two different orientations.

responds to Ti and O columns. The first is the expected $\Sigma5[001]\{310\}$ GB (Fig. 5.1b), which corresponds to the orientation of the $SrTiO_3$ bicrystal substrate. We also observe $\Sigma5[33\bar{1}]\{103\}$ GBs, which we propose are present due to the intersection of $\Sigma3\{112\}$ twin boundaries which form in the anatase grains (Figure 5.2). For the $\Sigma5[33\bar{1}]\{103\}$, we observe two different configurations in the experimental images, one that is symmetric about the boundary plane which we label the $\Sigma5[33\bar{1}]\{103\}$-S (Fig. 5.1c), and the other that is asymmetric which we label the $\Sigma5[33\bar{1}]\{103\}$-AS (Fig. 5.1d).

Periodic models of GBs are constructed by adjoining two grains, which can have different surface terminations. We identify only one inequivalent termination for the

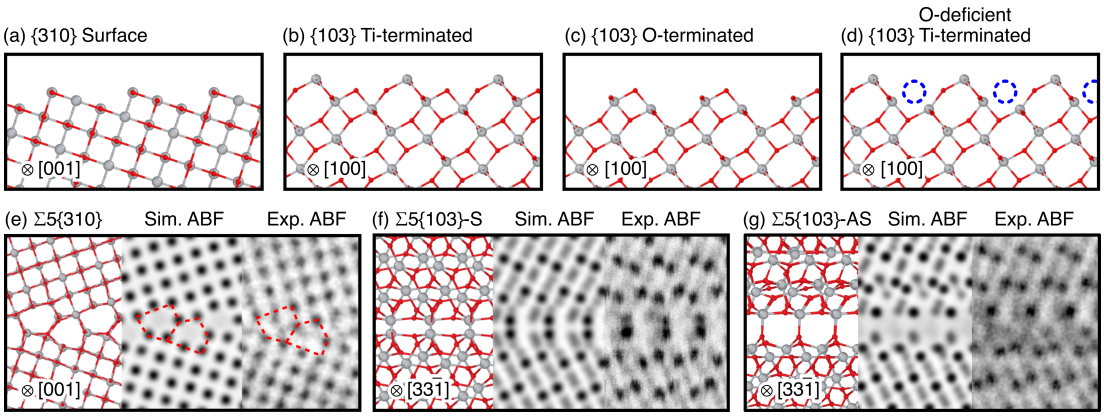

Fig. 5.3. Structural models for the surface termination of grains: (a) {310}, (b) Ti-terminated {103}, (c) O-terminated {103}, and (d) O-deficient Ti-terminated {103}. In all structural models, large gray spheres are titanium and small red spheres are oxygen. The projections for each view are given in the bottom left of each panel. Also shown are corresponding simulated and experimental ABF STEM images for the (e) Σ5{310}, (f) Σ5{103}-S, and (g) Σ5{103}-AS GBs.

{310} grain (Figure 5.3a) and our Σ5{310} GB model is constructed by combining two grains with this termination. For the {103} grain, we find three plausible surface terminations leading to several GB models. The symmetric Σ5{103}-S GB is constructed from two Ti-terminated grains (Fig. 5.3b). The combination of two O-terminated grains yields very high formation energies and was not considered further. The asymmetric Σ5{103}-AS GB can be constructed by combining an O-terminated grain (Figure 5.3c) and an oxygen-deficient Ti-terminated grain (Fig. 5.3d). The removal of oxygen from the Ti-terminated grain is necessary to eliminate the energetically-unfavourable dipole that would otherwise form between the grains. This oxygen-deficient surface termination has been observed experimentally in STEM studies of anatase nanorods.[158]

For each GB we identify the most stable structures by performing a series of geometry optimizations at the different rigid-body translations possible between the grains and calculating a formation energy (see Appendix B) as outlined in Section 3.3.2. We find two inequivalent minima for the Σ5{310} GB with almost identical formation energies of 1.03 Jm^{-2} and 1.09 Jm^{-2}. Simulated ABF STEM images were produced for both of these structures and the best agreement is found with the higher formation energy structure (Fig. 5.3e). When two GB structures are very close in energy, it is not unusual for the predicted lowest energy GB structures to not appear in experimental samples and similar behaviour is reported in a study of Σ5{310} GBs in magnesium oxide,[180] where it is attributed to the presence of calcium impurities which are not captured in the scan of rigid-body translations. Similarly, our rigid-body scans do not

account for slight non-stoichiometry resulting from oxygen deficiency or the presence of impurities in the sample. Our further simulations and analysis of electronic structure shall focus on the GB which shows better agreement with experiment. For the Σ5{103}-S GB, we determine one distinct minima that corresponds to a small formation energy of 0.64 Jm^{-2}. The simulated ABF STEM image produced for this structure is in excellent agreement with experimental observations (Fig. 5.3f). Our non-stoichiometric Σ5{103}-AS structure is missing 8 oxygen atoms per GB in the simulation supercell, meaning that its formation energy depends on the chemical potential of oxygen, μ_O. In the oxygen-poor limit (see Supporting Information), our Σ5{103}-AS structure has a formation energy of 0.91 Jm^{-2} and the simulated ABF STEM image shows good agreement with experimental observations in terms of the dark contrast corresponding to columns of titanium (Fig. 5.3g), but shows less agreement in terms of the contrast in the GB core.

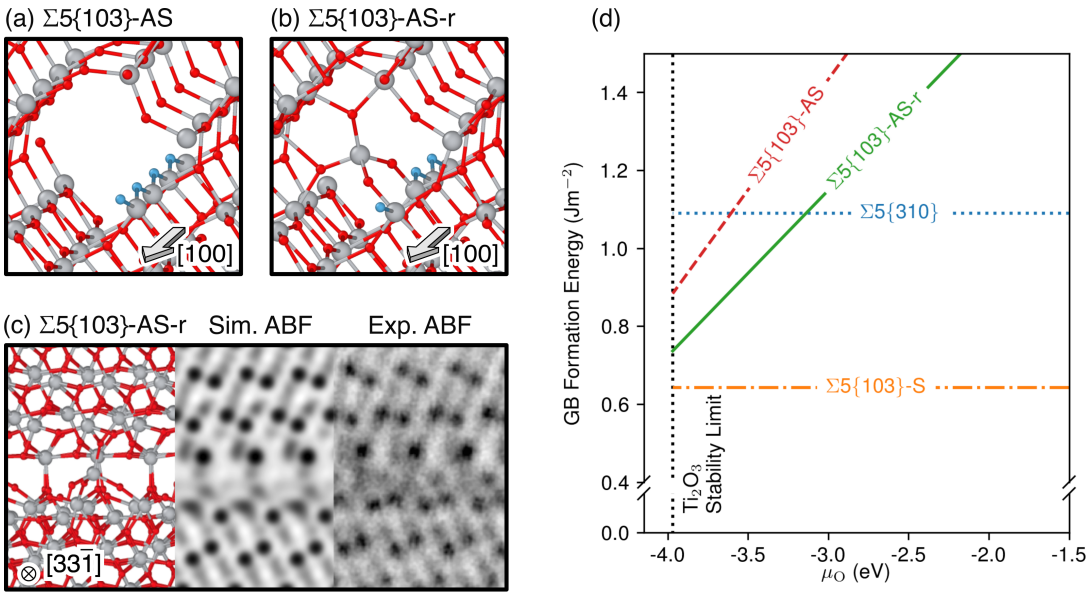

Fig. 5.4. Structural models of the (a) Σ5{103}-AS and (b) Σ5{103}-AS-r GBs. Large gray spheres are titanium, small red spheres are oxygen, and bridging oxygen atoms have been highlighted in blue. Projection indicated by arrows in bottom right of panels. (c) Structural model of the Σ5{103}-AS-r GB with corresponding simulated and experimental ABF STEM images. (d) Formation energies of the GBs as a function of the oxygen chemical potential, μ_O, showing that, in the O-poor limit, the Σ5{103}-AS-r GB has a similar formation energy to the Σ5{103}-S GB. Note that the full of range μ_O up to the oxygen-rich limit of $\mu_O = 0.0$ eV is not shown.

In the Σ5{103}-AS GB model, there are rows of 'bridging' oxygen atoms which have their bonds strained by around 12% (Figure 5.4a), with bonding that is analogous to the unreconstructed {001} anatase surface. For the {001} surface, this strain is relieved

by a well-characterized (1×4) reconstruction where every fourth bridging oxygen atom is replaced by a TiO_3 unit.[183] We attempt a similar reconstruction at the GB, which we label $\Sigma5\{103\}$-AS-r, where we replace every fourth bridging oxygen with a TiO_4 unit (Fig. 5.4b). This reconstruction reduces the strain on the bridging oxygen atoms to around 4%. When comparing simulated ABF STEM images with the experimental image, the $\Sigma5\{103\}$-AS-r model, we see that the there is still good agreement in terms of the positions of the columns of titanium but, with the addition of the TiO_4 units, there are darker regions within the GB core, which is in better qualitative agreement than the $\Sigma5\{103\}$-AS model (Fig. 5.4c). In the oxygen-poor limit of μ_O, the $\Sigma5\{103\}$-AS-r has a formation energy of 0.74 Jm^{-2}, which is significantly lower than that of our predicted $\Sigma5\{310\}$ structure or the $\Sigma5\{103\}$-AS structure (Figure 5.4d). Given the good agreement with the experimental image and the lower formation energy, our further analysis of electronic properties shall focus on the $\Sigma5\{103\}$-AS-r structure.

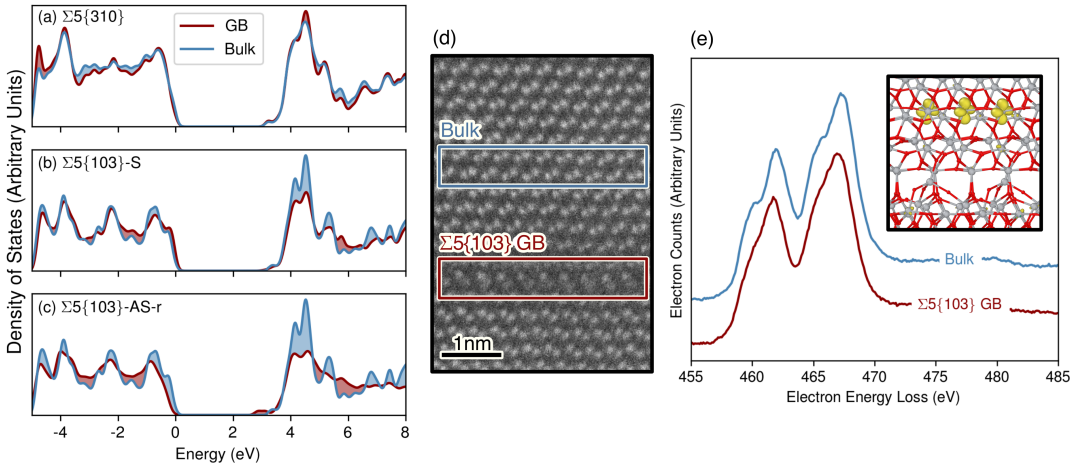

Fig. 5.5. Projected density of states for the (a) $\Sigma5\{310\}$, (b) $\Sigma5\{103\}$-S, and (c) $\Sigma5\{103\}$-AS-r GBs. For each plot, energy is relative to the valence band maximum, the blue curve represents the bulk-like region, and the red curve represents the GB region. The shaded portions indicate where a region has more states of a given energy. For the $\Sigma5\{310\}$ and $\Sigma5\{103\}$-S GBs, no states appear in the gap, but for the $\Sigma5\{103\}$-AS-r GB states appear around 0.5 eV below the conduction band minimum. (d) STEM image with boxes showing regions corresponding to electron energy loss spectroscopy (EELS) spectra. (e) EELS spectrum for the bulk-like region and the $\Sigma5\{103\}$-S GB region showing the Ti $L_{2,3}$ edge. Curves have been offset vertically for clarity. Note that, in the GB region, the two doublets are replaced by two broad peaks, indicating increased presence of Ti^{3+}. Shown in the top right is the absolute spin density isosurface (displayed at 0.05 a_0^{-3}) associated with electrons trapped in the vicinity of the $\Sigma5\{103\}$-S GB.

In order to understand the electronic structure of the GBs, projected density of

states (PDOS) for atoms in the vicinity of the GBs were calculated and compared with a bulk-like region far from the boundary plane. Neither the Σ5{310} nor the Σ5{103}-S exhibit significantly altered band gaps or any states within the gap (Figures 5.5a and 5.5b), which indicates that these GBs do not present deep charge traps in their equilibrium geometry. We verify this by explicitly adding electrons and holes, finding that holes delocalize over oxygen sites near the GBs and electrons delocalize over titanium sites in the bulk-like regions of the grains. For the oxygen-deficient Σ5{103}-AS-r, we see states appearing around 0.5 to 1.0 eV below the conduction band minimum (Fig. 5.5c), corresponding to electron traps (i.e. Ti^{3+} species, as seen in the inset in Fig. 5.5d). EELS measurements were carried out by our experimental collaborators on the Σ5{103} GB region to confirm this prediction (scanned regions are shown in Fig. 5.5d). We found the Σ5{103}-S structure is unstable under the electron beam so only the results of Σ5{103}-AS are presented (shown in Fig. 5.5e). The EELS spectra for the Σ5{103}-AS GB show that the two doublets associated with the Ti^{4+} $L_{3,2}$ edges in bulk anatase are replaced with the two broad peaks in the vicinity of the GB. Based on previous studies which compare Ti $L_{3,2}$ edges in TiO_2 and Ti_2O_3,[184] this is indicative of a higher proportion of Ti^{3+} compared to the bulk-like region. The box scan area for EELS analysis is shown in Fig. 5.5e.

To determine if the charge-trapping behaviour of the non-stoichiometric Σ5{103}-AS and Σ5{103}-AS-r GBs would also be observed in GBs containing dilute oxygen vacancies, we also modelled oxygen vacancies in the vicinity of the Σ5{310}, the Σ5{103}-S, and, for the sake of comparison, the Σ5{112} TB. It is found that, whilst there are some sites showing unfavourable segregation energies, we predict that there would be net segregation to the GBs (Figure 5.6). Much like in bulk anatase, across all of the sites investigated the v_O^{2+} configuration is always more favourable than the v_O^{1+} or v_O^0 configurations and so we do not predict that dilute vacancies in the vicinity of the Σ5{310}, Σ5{103}-S, or Σ3{112} would present deep electron traps. The segregation of charged defects to the GBs will lead to a space charge region developing. We assume, in the bulk, a molar concentration of 0.05 for v_O^{2+}, which is roughly what might be expected for an annealing temperature of 600 K when nearing the oxygen-poor limit. Then, by charge neutrality, a molar concentration of 0.1 for e^-, where we assume that e^- can occupy any Ti site with no drive to segregate towards or away from the GB, to mimic the behaviour of delocalised electrons in anatase. We predict fairly small space charge potential barriers of around 0.1 eV for the Σ5{310} and Σ5{103}-S, and around 0.05

eV for the Σ3{112} (Figure 5.7). These space charge barriers are the means by which a GBs that does not strongly trap charge may still negatively impact the conductivity of a device. In a dye-sensitised solar cell (DSSC), charge carriers injected by the dye must navigate their way through the polycrystalline transport layer to reach the electrode. If there is a significant segregation of v_O^{2+} defects to each GB, the combined effect of all the barriers at the GBs could cause a significant reduction in conductivity. Increasing the size of the grains and reducing the porosity of the sample would be one avenue to reduce the impact to conductivity posed by the GBs. However, this comes with the associated cost of reducing the available surface area for anatase to make contact with the solar-absorbing dye and so a balance would need to be sought between these factors.

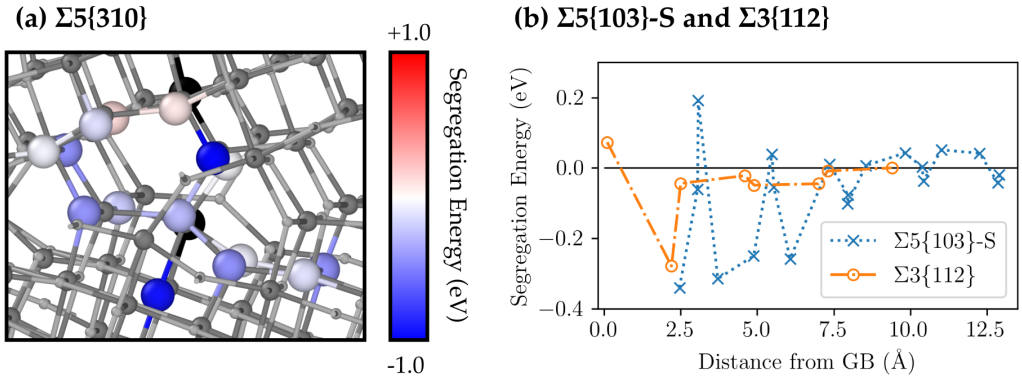

Fig. 5.6. (a) The Σ5{310} GB structure with large spheres color-coded to show the segregation energy associated with oxygen vacancies formed at that site. Black spheres indicate a site in which a vacancy cannot be formed without a neighbouring oxygen atom moving to fill the vacant site. (b) Segregation energies for oxygen vacancy formation in the Σ5{103}-S GB and Σ3{112} TB. Lines act as a guide to the eye.

Our results predict that the pristine Σ5{310} and Σ5{103}-S GB structures would be fairly benign for the performance of anatase in photovoltaic and photocatalytic applications. The GBs show no indication of charge traps in their equilibrium geometry nor do we predict that oxygen vacancies at the GBs would favourably trap electrons, though they would introduce a small space charge potential barrier. In contrast, the oxygen-deficient Σ5{103}-AS and Σ5{103}-AS-r GBs would be far more pathological for device performance; the structure inherently contains large numbers of oxygen vacancies and under-coordinated Ti sites. We find that the excess electrons trap on under-coordinated Ti sites, which is consistent with a previous theoretical study using the same functional investigating the properties of highly oxygen-deficient anatase nanoparticles.[102] Vacancies that strongly trap electrons at the GB would reduce the

number of mobile carriers introduced by each vacancy, reduce electron mobility, and could lead to increased carrier recombination, leading to reduced conductivity in photovoltaic applications. On the other hand, these trap states appear around 0.5 to 1.0 eV below the conduction band minimum and would increase visible light absorption. This is beneficial for photocatalytic applications and is supported by experiments that show oxygen-deficient anatase samples have higher photocatalytic performance.[185,186]

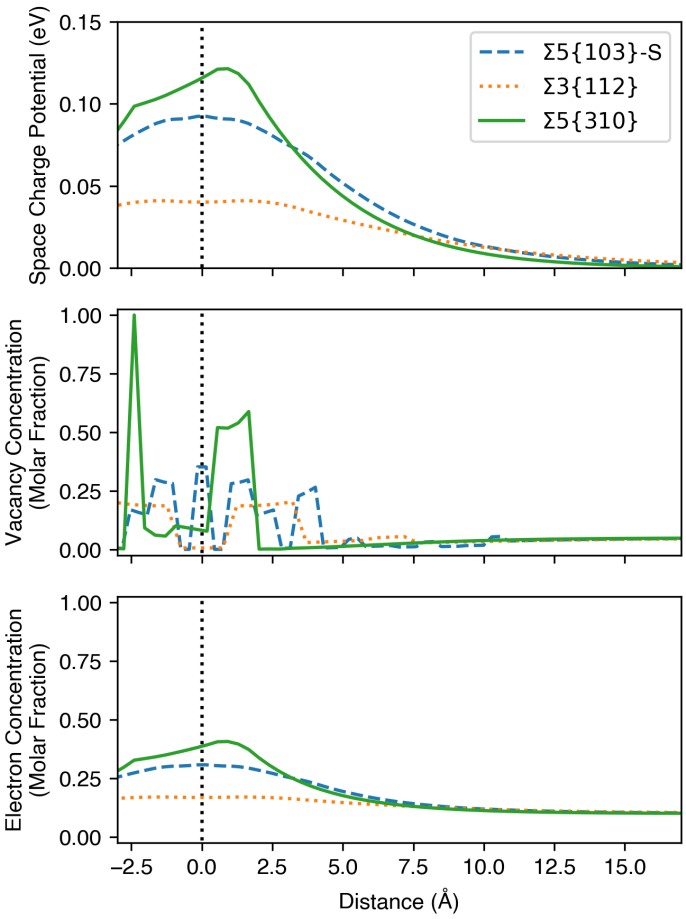

Fig. 5.7. The profiles of (a) space charge potentials, (b) oxygen vacancy molar concentrations, and (c) excess electron molar concentrations for the Σ5{310}, the Σ5{103}-S, and the Σ3{112}. Vertical dotted line indicates the presence of the GB. The perturbation to the potential propagates around 15 Å into the bulk. Note that the Poisson solver employed is site-explicit and so the vacancy concentration profile has a rather irregular shape, with asymmetry in the Σ5{310}. Also note that the segregation of vacancies to the GBs causes the immediate vicinity to be depleted of vacancies. These very low concentrations would be difficult to capture in a supercell calculation, highlighting the need for solving the Poisson-Boltzmann equation as outlined in Section 3.4.1.

These results provide insight into how the properties of GBs in anatase may be engineered to mitigate undesirable electron trapping. In the nanocrystalline anatase films employed in devices, GBs are formed when two nanoparticle surfaces come into

contact and attach during sintering or hydrothermal coarsening. Defects present at the surfaces of the precursor nanoparticles should influence the resulting GB structure. For example, it is known that GBs can form through oriented attachment of nanoparticles along minority facets during hydrothermal coarsening. This process has been identified as being responsible for the formation of $\Sigma3\{112\}$ twin boundaries in nanocrystalline anatase.[65] As stated previously, experimental observations have shown that {103} surfaces appear as oxygen-deficient minority facets in anatase nanoparticles, alongside surfaces such as {102}.[158] We suggest that, in the event that a GB forms through attachment along highly oxygen-deficient minority facets, it could be the case that a non-stoichiometric, oxygen-deficient structure similar to the $\Sigma5\{103\}$-AS or $\Sigma5\{103\}$-AS-r GBs may form. Anatase is typically oxygen-deficient and it is not straightforward to control the degree of oxygen-deficiency at surfaces or the quantities of minority facets present prior to sintering or coarsening. However, it would be possible to treat the surface of the nanoparticles with beneficial dopants so that these dopants can then become incorporated into the GBs. For example, a beneficial dopant might act as an electron donor, to fill charge traps introduced by non-stoichiometry. For less-reduced GBs, which we predict do not introduce deep traps, it may be preferential to seek a dopant that would mitigate the formation of a space charge, either by acting as an oppositely charged defect or by discouraging the segregation of oxygen vacancies to the GBs.

5.4 Conclusion

In summary, we present a combined experimental and computational investigation into the atomic and electronic structure of $\Sigma5\{310\}$ and $\Sigma5\{103\}$ GBs in anatase TiO_2. Low-energy structures predicted by the first-principles models show excellent agreement with experimental observations as evidenced by simulated ABF STEM images. Analysis of the electronic structure indicates that the $\Sigma5\{310\}$ GB would be relatively benign for the performance of photovoltaic or photocatalytic devices as it does not present electron traps in its equilibrium geometry. For the $\Sigma5\{103\}$ GB, however, we find two different GB structures. A stoichiometric structure that shows no electrons traps in equilibrium geometry and another, oxygen-deficient variant which we predict to contain a significant number of trapped electrons. These predictions are supported by EELS observations which shows the $\Sigma5\{103\}$ GB to be more reduced than the bulk-like regions of the grain. Our predictions of the lack of significant perturbation near

the pristine Σ5{310} and Σ5{103}-S GBs may provide some explanation as to why polycrystalline anatase shows excellent performance in applications. However, our prediction of the pathological charge-trapping behaviour of the oxygen deficient Σ5{103}-AS GBs highlights the need to consider the effects that chemical potential and growth conditions may have on the formation of highly-defective and non-stoichiometric boundaries. Mitigating these deleterious effects, e.g. *via* directed doping of the nanoparticle surfaces prior to sintering, should improve carrier mobility and reduce recombination leading to improved performance for applications in photovoltaics, photocatalysis and rechargeable batteries.

Chapter 6

Modeling of Oxygen-Deficient Anatase TiO_2 Nanoparticles[†]

6.1 Introduction

All of the studies presented so far in this thesis are concerned with relatively high-symmetry, extended systems. Whilst these models are very useful for elucidating the properties of grain boundaries (GBs), they will not capture certain features that will be present in a realistic nanocrystalline system. For example, even a perfect equilibrium nanoparticle made up of pristine surfaces will contain edges and vertices where facets meet. Such features have low symmetry and would not be trivial to model in a periodic supercell. There are examples of first-principles modelling of nanoparticles, but they are often limited in their scope or applicability. Many studies perform all calculations using local or semi-local density functional theory (DFT),[187,188] which is inappropriate for modelling charge trapping due to the self-interaction error (SIE). Another approach is to optimise the geometry using semi-local functionals and then apply hybrid DFT to a fixed geometry.[189,190] This is an improved approach but it is not, however, without issues when describing localised charges. Small polaronic states and their associated geometric distortion to the crystal lattice are inseparably linked; if a functional cannot properly describe localised charges, it cannot properly describe the geometry that would allow the charge to become localised. Nevertheless, it can still provide valuable insight in situations where charge localisation is not as relevant. For example, such an approach has been used to determine that the properties of an anatase nanoparticle start to linearly approach bulk-like behaviour at sizes beyond roughly 3 nm (beyond

[†]This chapter has been adapted from work which is published: Quirk JA, Lazarov VK, and McKenna KP. "First-Principles Modeling of Oxygen-Deficient Anatase TiO_2 Nanoparticles," *J. Phys. Chem. C*, vol. 124, no. 43, pp. 23637-23647, 2020.[102]

around 200 atoms), providing a valuable benchmark when constructing model nanoparticles.[191] Other studies have been carried out where geometries of anatase nanoparticles have been determined through a global optimisation procedure where energies are determined using hybrid DFT[192,193] which should be expected to provide more accurate descriptions of energetics and electronic structure, but only consider stoichiometric particles.

As discussed earlier, oxygen vacancies play a decisive role in determining the properties of anatase and a need remains to determine how these vacancies behave in nanoparticles. A previous study examined the properties of a single oxygen vacancy on a $Ti_{84}O_{168}$ nanoparticle using hybrid density functional theory using both standard PBE0 and a parameterisation of PBEα using $\alpha = 0.125$, similar to our generalized Koopmans' condition (GKC)-tuned value of $\alpha = 0.105$.[194,195] This study shows that the choice of α has pronounced effects on the specific location and spin configuration of the most stable vacancy, with the value of $\alpha = 0.125$ providing more reasonable results than PBE0. Reassuringly, it seems that qualitative trends - and therefore the associated predictions that can be made from them - are less affected by the choice of functional. Results from single oxygen vacancies are extremely useful but, in reality, nanoparticles should probably be expected to have multiple oxygen vacancies, though the rough amount of vacancies to be expected and how they interact is unclear. A natural next step would be to determine the degree to which nanoparticles can be reduced and what properties these highly reduced particles would have.

Here, we present hybrid DFT calculations of the atomic and electronic structure of explicit models of $Ti_{33}O_{66}$ and $Ti_{151}O_{302}$ anatase nanoparticles, where all calculations - including geometry optimisations - are carried out using our GKC-tuned hybrid density functional. We consider the reduction of these particles by the formation of oxygen vacancies in order to determine behaviour of excess charge in the nanoparticles. The explicit $Ti_{151}O_{302}$ model is of a sufficient size that it is at the onset of anatase-like crystallinity (based on previous results)[191] and provides a middle-ground between the very small $Ti_{33}O_{66}$ cluster which contains a large proportion of low-symmetry vertex and edge features and the larger, 'macroscopic' particles which consist primarily of extended surfaces and pristine bulk. In order to make comparisons with these macroscopic particles, we also consider extended surface models of facets appearing in the Wulff construction of anatase: the {101} facets, the {001} facets, and the possible reconstruction of the {001} facet and determine the position of the most stable vacancy in

the vicinity of these surfaces. It is shown that excess electrons introduced by vacancies in the vicinity of extended surfaces preferentially delocalise but the excess electrons in nanoparticles prefer to localise on under-coordinated Ti sites.

6.2 Computational Methods

The surfaces are modelled as slabs in a periodic supercell (as described in Section 3.2.1) where slabs are over 24 Å thick, with surface areas between 200 and 300 Å^2 and a vacuum gap of at least 12 Å. The surface models used in this work are taken from a previous study where analysis and discussion of convergence with respect to slab thickness is given.[70] Regarding oxygen vacancies in the vicinity of surfaces, for the {001} and {101} 7 atomic layers were considered to be in the vicinity of the surface, and for the reconstructed {001}, all symmetrically inequivalent sites across 5 atomic layers were considered to be in the vicinity of the surface. Calculations were carried out as detailed in Section 2.7.5.

The procedure to determine stable configurations for reduced nanoparticles first required the construction of $Ti_{33}O_{66}$ and $Ti_{151}O_{302}$ models where the shapes were based on the Wulff construction, using the surface energies for the {101} and {001}. The choice of 33 and 151 formula units of TiO_2 for the small and large nanoparticles are 'magic numbers' that produce high-symmetry Wulff-shaped particles without excessive under-coordination. The choice of the bi-pyramidal shape yielded by the Wulff construction is justified by previous work where this shape was yielded by a global optimisation procedure even for particles as small as our $Ti_{33}O_{66}$.[193] Then, a large number of starting structures were generated by randomly removing oxygen from the particle. These structures were then sorted by total coordination number in order to remove the particles with the lowest number of bonds, assuming that these systems will be less favourable. This is an educated assumption supported by a previous study that shows lower coordinated oxygen is, in general, easier to remove from nanoparticles.[194]

A selection of configurations were chosen such that each stoichiometry explored systems containing surface vacancies, subsurface vacancies, and a mixture of both. In total there were 3 configurations explored for each stoichiometry and the lowest energy system for each stoichiometry was taken forward for analysis. For the $Ti_{33}O_{33(2-\delta)}$ particle we generated a series of stoichiometries by removing 1 O at a time up to 8 removed O ($\delta = 0.24$) and for the $Ti_{151}O_{151(2-\delta)}$ we generated a series of stoichiometries by removing 2 O at a time up to 12 removed O ($\delta = 0.07$). For the large particle

approximations, the facet surface areas and volumes of Wulff constructions, and hence the number of O sites of a given kind, were determined using `WulffPack`.[149] Nanoparticles were modelled in an aperiodic cell using the Martyna-Tuckerman Poisson solver[196] as implemented in `CP2K` where the simulation cells for each particle are made to be over twice the size of the charge density. All geometry optimisation on nanoparticles is performed until the force on ions is less than 0.1 eVÅ^{-1}.

All calculations are spin-polarised, but the number of electrons in each spin channel is kept equal, such that there is no net magnetization in the system. This compromise primarily serves to reduce the size of spin-configuration space for the nanoparticle calculations. Whilst a true global minima may be a system with some net magnetization, the energy contribution due to the spin configurations is expected to be small compared to other contributions from charge localisation and the position of the vacancy. This is supported by calculations in bulk anatase where the difference between the singlet and triplet configurations of an oxygen vacancy with two localised electrons is only 0.09 eV. This energy difference is an order of magnitude smaller than the 0.95 eV energy difference between the localised singlet solution and the solution where two electrons are delocalised across the simulation cell.[54]

6.3 Results and Discussion

6.3.1 Oxygen Vacancies at Surfaces

First, to investigate the properties of large nanoparticles that are oxygen-deficient we consider O vacancies in the vicinity of the facets appearing in the Wulff construction of anatase: the {101} facets and {001} facets, with the {001} facet having a possible reconstruction. In this reconstruction, bridging O sites along the surface are periodically replaced with units of TiO_3, which acts to relieve strain and lowers the surface energy to about half that of the clean, unreconstructed {001} surface.[165,183] This reconstruction is, however, typically observed in thin-film samples annealed in vacuum and it is unclear how large the drive to reconstruct would be in other situations. For example, in the case of a small particle the space available for a reconstruction is limited and it would also be possible to relieve strain through relaxation of the entire particle. The surface formation energies, calculated as described in Equation 3.5, for the {101}, {001}, and reconstructed {001} facets are $\gamma_{\{101\}} = 0.46$ Jm^{-2}, $\gamma_{\{001\}} = 0.99$ Jm^{-2}, $\gamma^{\text{Recon.}}_{\{001\}} = 0.59$ Jm^{-2}, respectively. We focus on the most stable vacancy in the vicinity

of each surface. A definition of defect formation energies and the limits of μ_O can be found in Section 3.1.

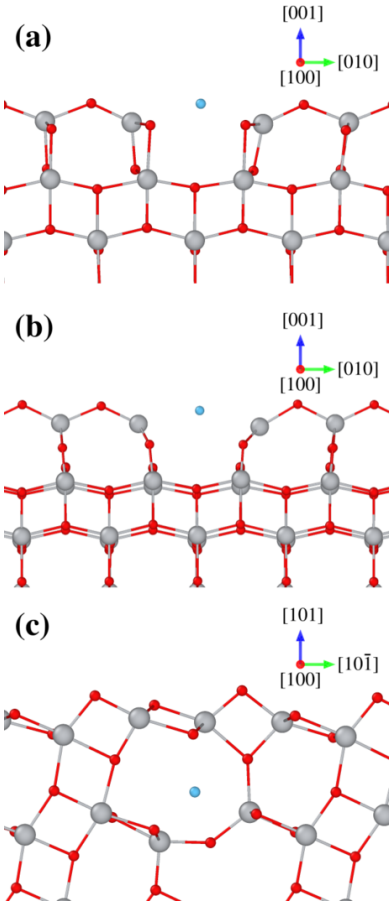

Fig. 6.1. Structures of the most stable vacancies at the (a) unreconstructed {001} surface, (b) {001} reconstructed surface, and (c) {101} surface. Titanium and oxygen ions are represented by gray and red spheres, respectively. Blue spheres indicate position of vacant oxygen.

For the {001} and reconstructed {001} surfaces the most stable vacancy occurs at the surface whereas in the {101} the most stable vacancy occurs at a subsurface site (Figure 6.1). The subsurface vacancy in the {101} is found to have a comparable formation energy to a vacancy in the bulk, only 0.04 eV more favourable. This is consistent with evidence that vacancies have a tendency to segregate away from the {101} to the subsurface and bulk even at low temperatures.[197,198] For O vacancies at both the {001} and reconstructed {001} surfaces we find that it is significantly more favourable to form vacancies, with formation energies 1.44 eV and 0.80 eV lower than the bulk-like solution, respectively. It is predicted that the most stable vacancies at each surface would be favourable to form in the O-poor limit (Figure 6.2). However, it is important to note that the vacancy formation energies were calculated for relatively

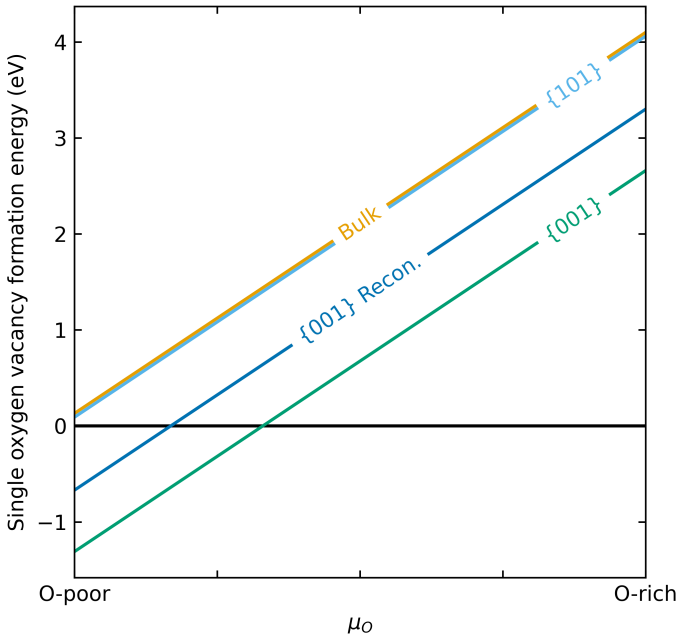

Fig. 6.2. Formation energies of the most stable neutral vacancies in bulk and in the vicinity the majority facets of anatase as a function of oxygen chemical potential, μ_O. The {101} and bulk formation energies are comparable. These formation energies apply to single oxygen vacancies and do not apply to the formation of two or more vacancies.

dilute vacancies in a supercell. Therefore, whilst the negative formation energies in the oxygen-poor limit suggests that at least one vacancy would form spontaneously, it should not be taken to imply that all surface sites would be vacant, nor would it provide an accurate approximation of the concentration of vacancies at these surfaces in such a limit, as there is no consideration of how formation energy is affected by the interaction between defects at very high concentrations.

Similar to the O vacancy in bulk anatase, the excess electrons prefer to delocalise in all of the considered vacancies near surfaces. These delocalised configurations come with a large distortion to the underlying lattice as ions move to screen the effect of the missing oxygen. From these results we conclude that dilute oxygen vacancies in extended surfaces would not be likely to present trapped charges detectable by electron paramagnetic resonance (EPR). Also of note is that the introduction of lower-coordinated Ti species into the majority surfaces does not lead to electron trapping as was observed in a recent study of high index facets.[70]

6.3.2 Reduced Nanoparticles

Low-energy configurations for a $Ti_{33}O_{33(2-\delta)}$ nanoparticle (diameter, $d \approx 1.5$ nm, Figure 6.3a) and a $Ti_{151}O_{151(2-\delta)}$ nanoparticle ($d \approx 2.5$ nm, Figure 6.3b) were determined as described in the Section 6.2. For the $Ti_{33}O_{33(2-\delta)}$ nanoparticles we consider values of $\delta = 0.00$ to 0.24 and for the $Ti_{151}O_{151(2-\delta)}$ we consider $\delta = 0.00$ to 0.07. For an explicit model of a nanoparticle of stoichiometry $Ti_NO_{N(2-\delta)}$ we calculate the formation energy of a neutrally-charged nanoparticle, $E_{\mathrm{d}}^{\mathrm{Particle}}$, as we would calculate a defect formation energy by

$$E_{\mathrm{d}}[\mathrm{Particle}] = E_{\mathrm{tot}}[\mathrm{Particle}] - NE_{\mathrm{tot}}[\mathrm{Bulk}] - \delta N\mu_{\mathrm{O}}, \tag{6.1}$$

where $E_{\mathrm{tot}}[\mathrm{Particle}]$ is the total energy of the particle and $E_{\mathrm{tot}}[\mathrm{Bulk}]$ is the total energy of a unit of bulk anatase. For a stoichiometric 'macroscopic' particle we make the assumption that the formation energy is dominated by the energy required to cleave the nanoparticle from pristine bulk, since the particle is large enough that the facets are essentially extended surfaces with little contribution from edge and vertex effects. Therefore, the formation energy of the stoichiometric 'macroscopic' nanoparticle, $E_{\mathrm{F}}^{\mathrm{Macro}}$, is dominated by the formation energy of the majority facets present in the nanoparticle and can be calculated as

$$E_{\mathrm{F}}^{\mathrm{Macro}} = \sum_i A_i\gamma_i, \tag{6.2}$$

where A_i is the area of the i-th facet, γ_i is the surface formation energy of the i-th facet. For a macroscopic nanoparticle of stoichiometry $Ti_NO_{N(2-\delta)}$, we must also include the formation energies of vacancies both in the bulk and the facets. Making the approximation that vacancies are spread homogeneously throughout the particle this case, then $E_{\mathrm{F}}^{\mathrm{Macro}}$ can be calculated as

$$E_{\mathrm{F}}^{\mathrm{Macro}} = \sum_i \left(A_i\gamma_i - \delta N_i^{\mathrm{O}} E_{\mathrm{F},i}^{\mathrm{Vacancy}}\right) - \delta N_{\mathrm{Bulk}}^{\mathrm{O}} E_{\mathrm{F,\,Bulk}}^{\mathrm{Vacancy}}, \tag{6.3}$$

where N_i^{O} is the number of stable O vacancy locations on the i-th facet, $N_{\mathrm{Bulk}}^{\mathrm{O}}$ is the number of bulk-like O sites not considered as being part of the surface, and $E_{\mathrm{F,\,Bulk}}^{\mathrm{Vacancy}}$ is the formation energy of an O vacancy in bulk. For a nanoparticle containing {101} facets and {001} facets the Wulff construction consists of 98.3% {101} facets and 1.7% {001} facets (Figure 6.3c) and for a nanoparticle containing {101} facets and reconstructed {001} facets the Wulff construction consists of 87.5% {101} facets and 12.5%

reconstructed {001} (Figure 6.3d). These calculations are performed at zero temperature where we do not consider the effects of entropy.

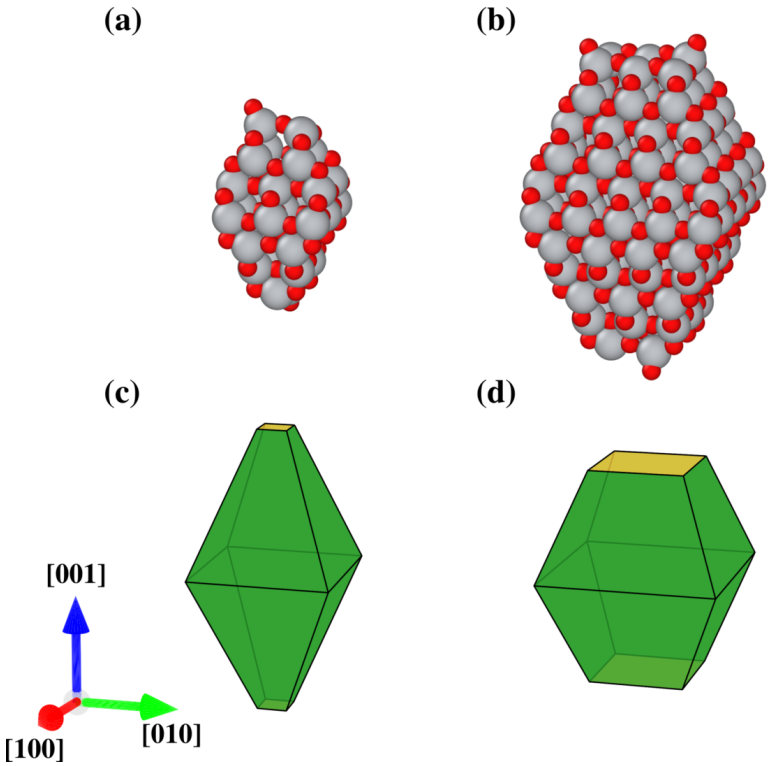

Fig. 6.3. Models of (a) atomic structure of $Ti_{33}O_{66}$ nanoparticle, (b) atomic structure of $Ti_{151}O_{302}$ nanoparticle, (c) Wulff construction involving {101} and {001} facets, and (d) Wulff construction involving {101} and reconstructed {001} facets. Titanium and oxygen ions are represented by gray and red spheres, respectively. {101} and {001} facets are represented by green and yellow facets, respectively.

In the O-rich limit, we observe that stoichiometric particles are always more favourable than their reduced counterparts. However, in the O-poor limit it is favourable to remove O from the particles, with the smaller particle being easier to reduce than the larger particle (Figure 6.4). In the O-poor limit the most reduced particles with a favourable formation energy were $Ti_{33}O_{59}$ ($\delta = 0.21$, for the small particle) and $Ti_{151}O_{294}$ ($\delta = 0.05$, for the large particle). The calculated formation energies per Ti for macroscopic particles exhibit low dependence on the size of the particle so, for illustrative purposes, we choose an example case of a $Ti_{12,000}O_{12,000(2-\delta)}$ nanoparticle ($d \approx 10$ nm, around what would be observed in experiment, consisting of 326.35 nm^2 {101} facets and 5.54 nm^2 {001} facets), using comparable values of δ, where we have assumed that vacancies are spread homogeneously throughout bulk and surface sites (Figure 6.4). Due to the form of Equation 6.3, the formation energy per Ti varies little with the size of the particle, so we show only the $Ti_{12,000}O_{12,000(2-\delta)}$ example. It is clear that larger particles are

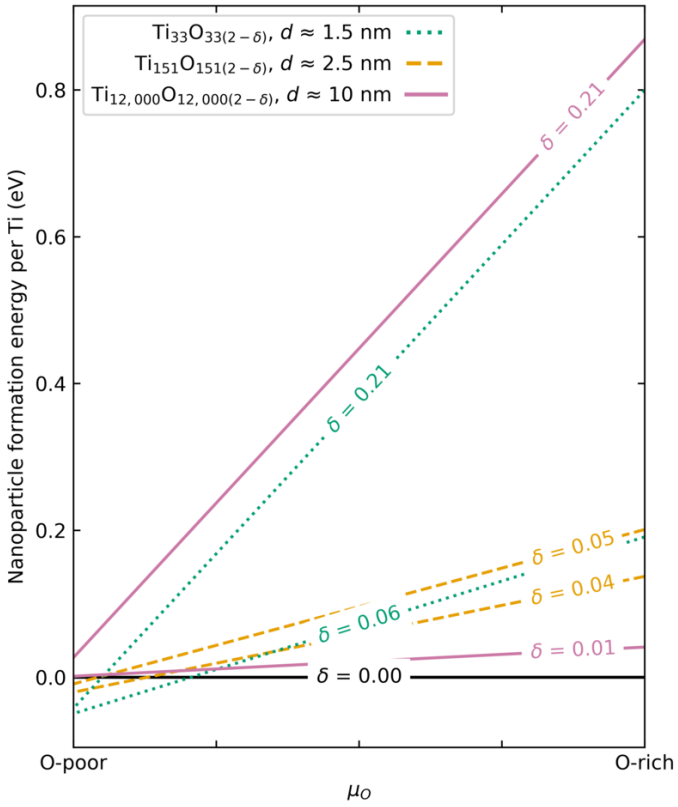

Fig. 6.4. Formation energies per Ti atom plotted as a function of μ_O for $Ti_{33}O_{33(2-\delta)}$, $Ti_{151}O_{151(2-\delta)}$, and the 'macroscopic' $Ti_{12,000}O_{12,000(2-\delta)}$ nanoparticles for various values of δ. All formation energies are taken relative to the stoichiometric configuration ($\delta = 0.00$) of the corresponding size of nanoparticle.

not as readily reducible to the same degree as smaller particles. One factor responsible for this is the presence of low-symmetry and low-coordinated sites. For example, in order to make a nanoparticle stoichiometric without the presence of O interstitials or Ti vacancies it is necessary to include 1-coordinated O on surface sites. Such sites remain energetically favourable in the O-rich limit but quickly become unfavourable as we move into the O-poor regime. Similarly, edge and vertex sites on the nanoparticles lead to atoms being overall lower coordinated than they would be in either bulk or extended surfaces, even before the removal of any further O. The {001} and reconstructed {001} surfaces also exhibit vacancies that are favourable in the O-poor limit but, even if we were to unrealistically remove all of these O from a large Wulff construction particle, it would represent an extremely small value of δ compared to the value of δ observed in our model particles. We emphasize here that these are formation energies at 0 K with

no consideration of effects of configurational entropy of the nanoparticles and, whilst they provide evidence of a trend, we make no attempt to assign specific values of δ that would be expected at finite temperature.

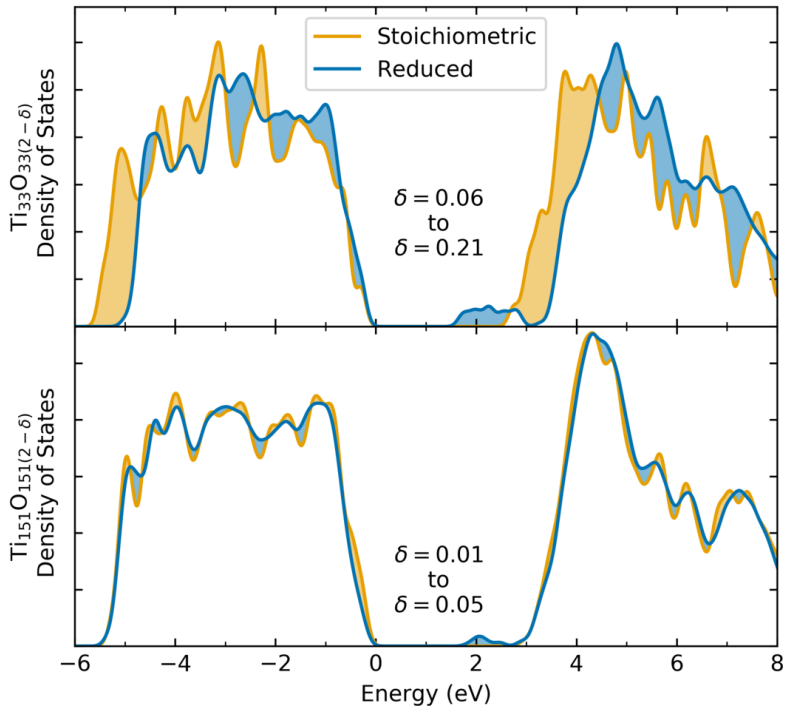

Fig. 6.5. Density of states for (top) the $Ti_{33}O_{33(2-\delta)}$ particles and (bottom) the $Ti_{151}O_{151(2-\delta)}$ particles. Yellow represents the stoichiometric configuration and blue represents the average density of states (DOS) of all favourable reduced configurations. Shaded regions indicate where a configuration has more states of a given energy. In the interest of clarity, the DOS represents the sum of both spin channels.

We calculate the DOS for the modelled nanoparticles and, in order to separate the properties due to the morphology of the nanoparticle and the properties due to reduction, we compare the DOS of the stoichiometric nanoparticles with the average DOS of all favourable reduced stoichiometries (Figure 6.5). The stoichiometric $Ti_{33}O_{33(2-\delta)}$ configuration has a band gap around 0.3 eV lower than any of the $Ti_{151}O_{151(2-\delta)}$ configurations, which can be attributed to states at the valence band maximum (VBM) associated with one-coordinated O sites. When considering reduced $Ti_{33}O_{33(2-\delta)}$ particles, these states are removed and the gap is increased to around 3.0 eV, comparable to the $Ti_{151}O_{151(2-\delta)}$. Reduced nanoparticles contain states in the band gap and, in the more highly reduced $Ti_{33}O_{33(2-\delta)}$ systems, these states appear deeper in the gap. For the $Ti_{151}O_{151(2-\delta)}$, the overall shape of the valence and conduction band remains

relatively unperturbed by reduction, but we see states appearing around 0.5 to 1.0 eV below the conduction band maximum (CBM) in the reduced case. In the case of the $Ti_{33}O_{33(2-\delta)}$ nanoparticles, reduction causes a large change in the shape of the bands. The gap states associated with reduced $Ti_{33}O_{33(2-\delta)}$ appear around 0.5 to 1.5 eV below the CBM, slightly deeper than the $Ti_{151}O_{151(2-\delta)}$ case. These results are consistent with observations that reduced anatase has increased photocatalytic performance.[185,186,199] Defect-free anatase requires ultraviolet radiation for photoexcitation, but these shallow states below the CBM would lead to increased visible light absorption, a very desirable trait if anatase is to be used as a photocatalyst under sunlight. This increased absorption in O-deficient anatase has been observed experimentally and upon annealing in O-rich atmospheres the states disappear, confirming that they originate from reduced Ti species.[200,201]

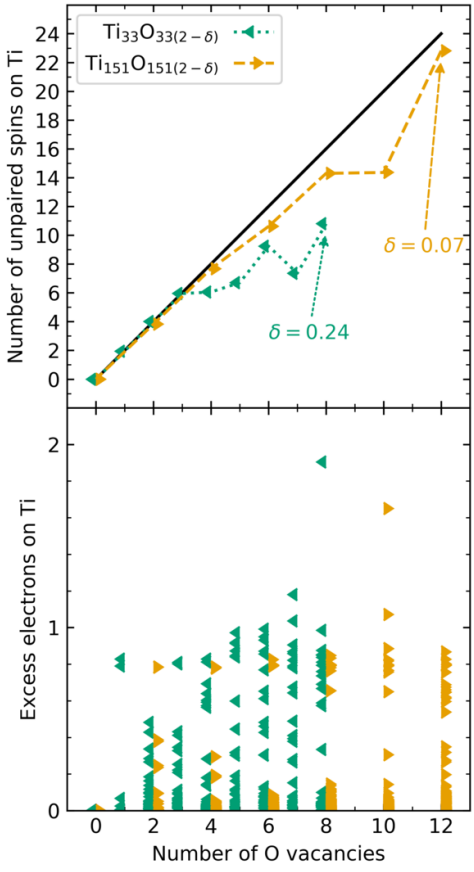

Fig. 6.6. Plot of (top) number of unpaired spins associated with Ti sites and (bottom) number excess electrons associated with each Ti site against number of O vacancies. The solid black line indicates the trend followed if the number of unpaired spins is equal to the number of excess electrons.

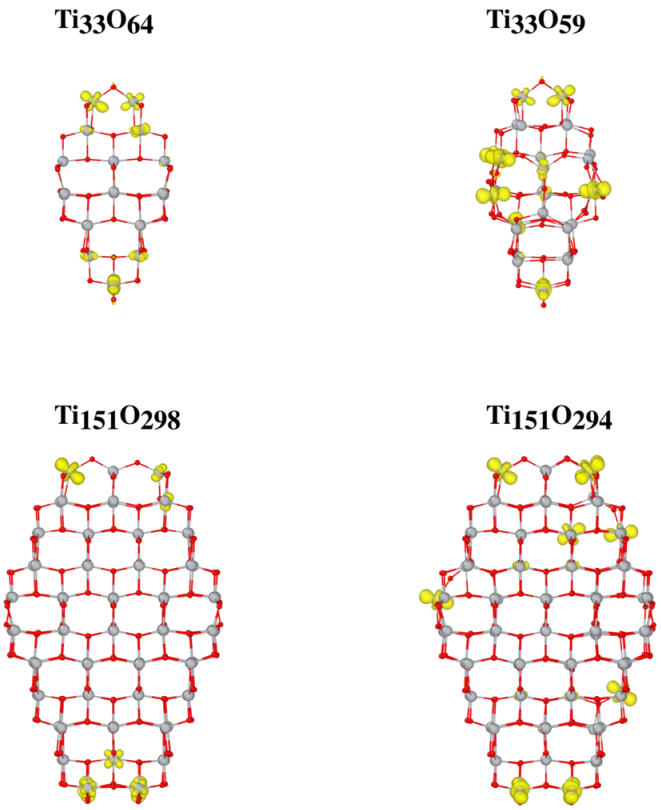

Fig. 6.7. Absolute spin density isosurfaces (isosurface value 0.015 a_0^{-3}) for various stoichiometries of nanoparticle. Titanium and oxygen ions are represented by gray and red spheres, respectively.

To determine the behaviour of excess charges, we perform Bader analysis* on the model nanoparticles.[202–205] Unpaired spins would be visible to EPR, so in order to facilitate comparison with experiment we also consider the absolute spin density associated with each site. We can consider the magnetic moment on a site as being related to the localisation of electrons; if electrons localise to form a Ti^{3+}, then we should expect that there will be unpaired spins on those Ti sites. Therefore, if all electrons localise to form a Ti^{3+} species, we should expect the absolute number of unpaired spins to be equal to the total number of excess electrons introduced by vacancies; it should be noted that, whilst we have fixed the population of each spin channel such that there is no net magnetisation, there can still be local magnetic moments associated with unpaired spins on a given site. All of the electrons introduced by vacancies appear above the VBM; either delocalised into the conduction band or localised into a gap state. Therefore, by taking the partial charge density associated with these excess electrons

*The charge density used in Bader analysis is the *total* charge density including core electrons from the pseudopotential, rather than only the valence electrons.

introduced by the vacancies and partitioning this partial charge density into the atomic volumes determined from Bader analysis, we can determine how many of the excess electrons are held by each Ti atom in the nanoparticle.

In contrast to the extended models of bulk and of majority facets, we find that excess electrons present in the reduced nanoparticles have a tendency towards localising to form Ti^{3+} species at under-coordinated Ti sites near surfaces (Figure 6.7), as evidenced by the high proportion of unpaired spins present compared to the number of excess electrons (Figure 6.6, top). To illustrate how the excess electrons are distributed across sites, we plot the number of excess electrons associated with the Bader volumes of Ti (Figure 6.6, bottom). For each stoichiometry of $Ti_{151}O_{151(2-\delta)}$ we determined to be stable, we see that in most cases the majority of the excess electrons are unpaired except for one stoichiometry that contains an anomalously low number of unpaired spins. Generally there are 2 distinct bands that would correspond to Ti^{4+} and Ti^{3+}, except for the system containing a low number of unpaired spins (Figure 6.6, yellow points, 10 O vacancies). In this system we see a particularly large number of excess electrons on one site, which would indicate that, rather than these excess electrons being delocalised, they have become trapped as a Ti^{2+} species which would be a trap that is invisible to EPR. For the stable stoichiometries of $Ti_{33}O_{33(2-\delta)}$, we find that there is a comparatively lower proportion of unpaired spins than in the $Ti_{151}O_{151(2-\delta)}$ particles but, we do not observe an increase in the number of sites with a number of electrons significant enough that they would correspond to a Ti^{2+}. Instead, we see far less distinct bands in the number of excess electrons and a far greater proportion of sites containing non-negligible numbers of excess electrons (Figure 6.6, bottom, green points). This is indicative of two features: firstly, that the overall symmetry of the small particles is lower than that of the large particles and; secondly, the number of sites available to excess electrons is overall lower in the small particles, meaning that the traps associated with surface sites quickly begin to become filled, forcing more electrons into delocalised solutions.

These results lead us to predict that nanoparticle size has a pronounced effect on the degree to which a sample can be reduced which, in turn, has a pronounced effect on the properties of the material due to the number of Ti^{3+} and Ti^{2+} species that are able to form. It has been observed that Ti^{3+} and Ti^{2+} states in highly reduced of TiO_2 show extremely high photocatalytic activity.[27] We suggest that small nanoparticles would be better suited to photocatalytic applications for two reasons:

firstly, that they would have a larger surface-area-to-volume ratio which is beneficial in catalytic applications; and secondly, that smaller particles are easier to reduce which would allow the creation Ti^{3+} and Ti^{2+} species and increase visible light activity, as discussed previously. We also predict that electron trapping would be more prevalent in nanocrystalline samples than in single crystals but, despite the majority of excess charges becoming trapped in our models, we do not predict that the majority of excess electrons would become trapped in samples containing larger nanoparticles. We remind the reader that our model nanoparticles are small and contain a disproportionate amount of surface features whereas a larger nanoparticle would contain regions better described by the extended models of bulk and surface and the delocalised configurations associated with such extended systems should be expected. Additionally, our results correspond to zero temperature, but it is expected that at finite temperature a proportion of these traps would become unstable, allowing carriers to delocalise. Conductivity experiments have shown that the conductivity of polycrystalline anatase increases with temperature,[206,207] which might, in part, be attributable to increased rates of polaron hopping, but is likely also due to an increase in the number free carriers due to traps becoming ionised; such behaviour is reported in EPR studies where signals from Ti^{3+} species are diminished at room temperature.[56] One of these conductivity experiments[206] demonstrated higher conductivity in particles of smaller diameter, which would be in agreement with our prediction that these particles would be easier to reduce and would contain a higher number of carriers but we emphasize that smaller particles would lead to lower electron mobility due to the number of trap states present in small, reduced particles. This concept is supported by the fact that, whilst increased conductivity is observed at decreased partial pressures of O_2 (i.e. in the O-poor limit, where vacancies are expected to be prevalent), it is also observed that conductivity saturates at high partial pressures of O_2[207] which can be attributed to the decrease in free carrier concentration being balanced by an increase in electron mobility due to the smaller number of trap states present in less-reduced particles. We suggest that this trade-off between number of carriers and electron mobility must be considered for applications where conductivity is important.

6.4 Conclusion

In summary, we have investigated oxygen vacancies and charge trapping in anatase through first-principles calculations of extended {101}, unreconstructed {001}, and re-

constructed {001} surfaces and we compare these results to explicit models of $Ti_{33}O_{33(2-\delta)}$ and $Ti_{151}O_{151(2-\delta)}$ nanoparticles. We find that electrons introduced by vacancies at extended surfaces preferentially delocalise across all Ti sites. However, when considering $Ti_{33}O_{33(2-\delta)}$ and $Ti_{151}O_{151(2-\delta)}$ nanoparticles, electrons will localise to form Ti^{3+} species even when the level of reduction is relatively low and, when reduced further, Ti^{2+} species can also form. The presence of Ti^{3+} species associated with oxygen vacancies in is frequently observed in EPR experiments on anatase nanoparticles,[56,186,199,208] but Ti^{2+} species represent a trap that would be invisible to EPR. The degree to which a particle can be reduced was found to depend strongly on the size of the particle and we suggest that smaller particles will be preferable for photocatalytic applications due to providing better visible light absorption and increased surface area. For photovoltaic and battery applications, there will be a balance to be considered between number of carriers introduced by vacancies and the number of trap states introduced due to particle size and number of under-coordinated Ti sites.

Our nanoparticle models show encouraging agreement with experimental observations, but there are still other open questions. For example, we have only considered an isolated Wulff construction nanoparticle but, depending on growth conditions, anatase nanoparticles can take a wide range of morphologies[209,210] which may exhibit different size-dependent properties regarding reduction and charge trapping. Additionally, adsorption at the surface is important to photocatalytic processes and further investigation into how the presence of nanoparticle features such as edges and vertices change the behaviour of adsorbed species would be valuable. This study has provided insight into reduction and the behaviour of charges, but more work would be required to develop a full understanding of how the size and shape of nanoparticles affects its properties.

Chapter 7

Conclusions

As explained in Chapter 1, an understanding of the behaviour of charge carriers is crucial to understanding the properties of a material. If charge carriers can become trapped in a material, then carrier mobility will be decreased and rates of carrier recombination will be increased. Both of these processes reduce conductivity and will prevent charge carriers from becoming useful, either by reaching an electrode and generating a current or by reaching the surface to undergo a reaction with an adsorbate. The anatase phase of titanium dioxide shows excellent performance in applications including photocatalysis and as an electron transport layer for photovoltaic (PV) applications.[23–26,30–33] This high performance can, in part, be attributed to anatase not allowing electrons to become self-trapped in the bulk and hence exhibiting high electron mobility,[54,56,57] but detailed experimental analysis beyond this is challenging due to the polycrystalline nature of anatase. Previous computational work has predicted that this lack of electron traps also applies to common point defects, such as oxygen vacancies and titanium interstitials, where the most favourable situation is for electrons to delocalise.[54] Predictions for point defects in bulk are valuable, but grain boundaries (GBs), twin boundaries (TBs), and surfaces play a large role in determining the properties of a polycrystalline material. This thesis presented first-principles models of various extended defects using a hybrid density functional theory (DFT) approach optimised for describing charge trapping in anatase. The findings from this study have helped to elucidate how these extended defects impact device performance so that we may devise appropriate methods of engineering anatase for various applications.

Chapter 4, is concerned with the $\Sigma3\{112\}$ and and $\Sigma1\{110\}$ TBs, which are calculated to have very low formation energies. The $\Sigma3\{112\}$ TB is frequently observed in nanocrystalline samples of anatase,[65] and our predicted structure shows excellent agreement with experimental observations. The low formation energy of $\Sigma1\{110\}$ TB

would imply that it occurs frequently in anatase, but its very high symmetry would make it extremely difficult to observe using transmission electron microscopy (TEM). We propose that scanning tunneling microscopy (STM) on [001]-oriented anatase (e.g. as grown on $SrTiO_3$ {001}) would be capable of resolving this defect. Neither of these TBs allows the formation of electron polarons nor do any states appear in the band gap. Due to this, we predict that neither TB would be significantly problematic when considering anatase as an n-type conductor. Deep hole traps are present near the TBs, however, which could be problematic for photocatalytic applications by enabling non-radiative recombination of photogenerated carriers before they can reach the surface and undergo reactions with adsorbates.

The TBs from Chapter 4 are very high-symmetry and they neither contain broken bonds nor do they impose any significant strain. With this in mind, it is not too surprising that anatase would tolerate these defects with little perturbation to it electronic structure. However, in Chapter 5 we show that this behaviour also extends to some lower-symmetry GBs and, even where the GBs contain broken bonds, no states are introduced into the gap and no significant perturbation to the electronic structure is observed. We do, however, predict that intrinsically highly oxygen-deficient GBs would have reasonably low formation energies in the O-poor limit and that these non-stoichiometric boundaries would introduce electron traps. We propose that highly-reduced nanoparticle facets, of which some have been observed experimentally,[158] would enable the formation of non-stoichiometric and pathological GBs. To provide a more complete understanding of the role of oxygen vacancies, we also considered the segregation of dilute concentrations of oxygen vacancies in the vicinity of GBs. Much like in bulk, we find that it is more favourable for electrons to delocalise rather than to become trapped. Even though these vacancies would not strongly trap charge, we show that they would still impact the performance of a device by segregating to GBs and creating a space charge region which would present an electrostatic barrier to inter-grain electronic transport.

Chapter 6 provides some further insight into oxygen deficiency in nanoparticles and we predict that, in O-poor conditions, it becomes energetically favourable to form vacancies in both extended surfaces and explicitly modelled nanoparticles. We compare a 'macroscopic' model based on extended surfaces with two differently-sized model nanoparticles and find that the smaller particles should be expected to more oxygen-deficient than their larger counterparts, and that the higher proportion of under-

coordinated sites at surfaces, edges, and vertices can lead to large numbers of charge carriers becoming trapped. These findings imply that smaller particles would be preferable for photocatalytic applications due to providing better visible light absorption due to the large number of gap states associated with vacancies at the surface and their large surface-area-to-volume ratio. For photovoltaic and battery applications, there will be a balance to be considered between number of carriers introduced by vacancies and the number of trap states introduced due to particle size.

In summary, these results build up a picture of GBs in anatase impacting performance not through their inherent structure, but by their interaction with point defects, namely oxygen vacancies. In dilute concentrations, charged oxygen vacancies will contribute to the development of a space charge region and an associated potential barrier. In high concentrations, these vacancies will start to introduce relatively deep traps on under-coordinated titanium sites. Given that we predict oxygen vacancies at GBs more seriously impact performance than vacancies in the bulk, we propose a strategy of doping the surfaces of nanoparticles prior to sintering. When these surfaces come into contact during sintering, these dopants would become incorporated primarily into the GB regions where they can be most useful, rather than spreading them homogeneously through the bulk of the material.

7.1 Future Work

This project has been concerned with how the behaviour of charge carriers in polycrystalline anatase is affected by tilt GBs, surfaces, and explicit models of nanoparticles. This is valuable, but it is by no means an exhaustive investigation of extended defects. For example, the GBs presented in this thesis are symmetric tilt boundaries in that each grain presents the same crystallographic plane at the GB. In general, GBs may present different crystallographic planes at the GB (for example, {310} and {210}). There are also twist GBs, where the axis of rotation is perpendicular to the GB plane rather than parallel. A real sample of sintered anatase nanoparticles would likely contain a combination of symmetric tilt GBs, asymmetric tilt GBs, twist GBs, and GBs which are a non-idealised mixture of all these types. The strain induced by these GBs may then contribute to the formation of dislocations, which would complicate the matter further. Examples of such systems are have very low symmetry and the determination of stable structures would be constrained due to the requirement for large supercells as well as the vast quantities of possible configurations that would need to be considered.

The sort of systematic scans through configurations shown in this thesis may not be appropriate, but success has been found in elucidating complex structures through the use of genetic algorithms or ab-initio random structure searching.[181,211]

Even if these more challenging defects prove too computationally-demanding to tackle, there is still plenty of valuable analysis that could be carried out on the systems that are presented in this thesis. The discussion in this thesis is concerned with the static picture of equilibrium geometries of extended defects and charges trapped at point defects or by lattice distortions. As this thesis frequently alludes to, these traps will act as recombination centers and are associated with a decrease in mobility, but the specifics of these processes have not been explored in detail. There is first-principles theory that allows for the determination of the rates of non-radiative recombination between trapped carriers and carriers in band edges[110,138] and related theory that allows for the calculation hopping rates and barriers for small polarons,[212,213] without the need for explicitly calculating excited state properties. Further studies could build on the work in this thesis by determining how recombination and polaron hopping differs in the vicinity of GBs compared to in the bulk of the material in order to provide a more complete picture of exactly what role GBs play in device performance.

Abbreviations

ABF Annular bright field

ADMM Auxiliary density matrix method

BF Bright field

BSSE Basis-set superposition error

CBM Conduction band maximum

COHSEX Coulomb hole and screened exchange

CTEM Conventional transmission electron microscopy

DF Dark field

DFT Density functional theory

DFT+U DFT with a Hubbard-like correction

DOS Density of states

DSSC Dye-sensitised solar cell

EELS Electron energy loss spectroscopy

EPR Electron paramagnetic resonance

GB Grain boundary

GGA Generalised gradient approximation

GKC Generalized Koopmans' condition

GTH Goedecker-Tetter-Hutter

GTO Gaussian-type orbital

GW Approximation to the self-energy from the Hedin equations

HAADF High-angle annular dark field

HEG Homogeneous electron gas

HF Hartree-Fock

HOMO Highest-occupied molecular orbital

hybrid DFT A formulation of density functional theory employing some portion of exact Fock exchange

KS Kohn-Sham

LCAO Linear combination of atomic orbitals

LDA Local-density approximation

LUMO Lowest-unoccupied molecular orbital

MGGA Meta-generalised gradient approximation

MOLOPT Molecularly-optimised

PAW Projected augmented wave

PBE Perdew-Burke-Ernzerhof

PBEα Linearly-mixed Perdew-Burke-Ernzerhof hybrid functional

PBE0 Parameterisation of PBEα where $\alpha = 0.25$.

PDOS Projected density of states

PL Photoluminescence

PV Photovoltaic

SCAN Strongly constrained and appropriately normed

SIE Self-interaction error

STEM Scanning transmission electron microscopy

STM Scanning tunneling microscopy

STO Slater-type orbital

TB Twin boundary

TEM Transmission electron microscopy

TISE Time-independent Schrödinger equation

tr-PBEα Coulomb-truncated PBEα

VBM Valence band maximum

Bibliography

[1] A. M. Al-Hamdi, U. Rinner, and M. Sillanpää, "Tin Dioxide as a Photocatalyst for Water Treatment: a Review," *Process Saf. Environ.*, vol. 107, pp. 190–205, 2017.

[2] J. Cheng, J. Wang, Q. Li, H. Liu, and Y. Li, "A Review of Recent Developments in Tin Dioxide Composites for Gas Sensing Application," *J. Ind. Eng. Chem.*, vol. 44, pp. 1–22, 2016.

[3] J. Wolfenstine, J. L. Allen, J. Sakamoto, D. J. Siegel, and H. Choe, "Mechanical Behavior of Li-Ion-Conducting Crystalline Oxide-Based Solid Electrolytes: a Brief Review," *Ionics*, vol. 24, no. 5, pp. 1271–1276, 2018.

[4] C. Stampfl and A. J. Freeman, "Stable and Metastable Structures of the Multiphase Tantalum Nitride System," *Phys. Rev. B*, vol. 71, no. 2, p. 024111, 2005.

[5] L. Wang, B. Chen, J. Ma, G. Cui, and L. Chen, "Reviving Lithium Cobalt Oxide-Based Lithium Secondary Batteries – Toward a Higher Energy Density," *Chem. Soc. Rev.*, vol. 47, no. 17, pp. 6505–6602, 2018.

[6] M. Zhang, J. Wu, Y. Zhu, D. O. Dumcenco, J. Hong, N. Mao, S. Deng, Y. Chen, Y. Yang, C. Jin, *et al.*, "Two-Dimensional Molybdenum Tungsten Diselenide Alloys: Photoluminescence, Raman Scattering, and Electrical Transport," *ACS Nano*, vol. 8, no. 7, pp. 7130–7137, 2014.

[7] M. Shanmugam, T. Bansal, C. A. Durcan, and B. Yu, "Schottky-Barrier Solar Cell Based on Layered Semiconductor Tungsten Disulfide Nanofilm," *Appl. Phys. Lett.*, vol. 101, no. 26, p. 263902, 2012.

[8] M. Shanmugam, C. A. Durcan, R. Jacobs-Gedrim, and B. Yu, "Layered Semiconductor Tungsten Disulfide: Photoactive Material in Bulk Heterojunction Solar Cells," *Nano Energy*, vol. 2, no. 3, pp. 419–424, 2013.

[9] B. Banerjee, "Modern Slavery is an Enabling Condition of Global Neoliberal Capitalism: Commentary on Modern Slavery in Business," *Bus. Soc.*, vol. 60, no. 2, pp. 415–419, 2021.

[10] Y. H. Kim and G. F. Davis, "Challenges for Global Supply Chain Sustainability: Evidence from Conflict Minerals Reports," *Acad. Manag. J.*, vol. 59, no. 6, pp. 1896–1916, 2016.

[11] T. C. Frankel, M. R. Chaves, and J. Ribas, "The Cobalt Pipeline," *Washington Post*, 2016. Accessed on 2021-03-23 at: `https://www.washingtonpost.com/graphics/business/batteries/congo-cobalt-mining-for-lithium-ion-battery/`.

[12] K. Morita and T. Miki, "Thermodynamics of Solar-Grade-Silicon Refining," *Intermetallics*, vol. 11, no. 11-12, pp. 1111–1117, 2003.

[13] L. El Chaar, N. El Zein, *et al.*, "Review of Photovoltaic Technologies," *Renew. Sustain. Energy Rev.*, vol. 15, no. 5, pp. 2165–2175, 2011.

[14] M. Jacoby, "The Future of Low-Cost Solar Cells," *Chem. Eng. News*, vol. 94, no. 18, pp. 30–35, 2016.

[15] R. Kopecek and J. Libal, "Towards Large-Scale Deployment of Bifacial Photovoltaics," *Nature Energy*, vol. 3, no. 6, pp. 443–446, 2018.

[16] A. Romeo, G. Khrypunov, F. Kurdesau, M. Arnold, D. Bätzner, H. Zogg, and A. Tiwari, "High-efficiency Flexible CdTe Solar Cells on Polymer Substrates," *Sol. Energy Mater. Sol. Cells*, vol. 90, no. 18-19, pp. 3407–3415, 2006.

[17] J. Ibers, "Tellurium in a Twist," *Nat. Chem.*, vol. 1, no. 6, pp. 508–508, 2009.

[18] "Web of Science," Accessed on 2021-03-24 at: `http://apps.webofknowledge.com`.

[19] C.-C. Wang and J. Y. Ying, "Sol-Gel Synthesis and Hydrothermal Processing of Anatase and Rutile Titania Nanocrystals," *Chem. Mater.*, vol. 11, no. 11, pp. 3113–3120, 1999.

[20] K. T. Kim, M. Y. Eo, T. T. H. Nguyen, and S. M. Kim, "General Review of Titanium Toxicity," *Int. J. Implant Dent.*, vol. 5, no. 1, pp. 1–12, 2019.

[21] P. Boffetta, A. Soutar, J. W. Cherrie, F. Granath, A. Andersen, A. Anttila, M. Blettner, V. Gaborieau, S. J. Klug, S. Langard, *et al.*, "Mortality Among Workers Employed in the Titanium Dioxide Production Industry in Europe," *Cancer Causes Control*, vol. 15, no. 7, pp. 697–706, 2004.

[22] J. Wang, G. Zhou, C. Chen, H. Yu, T. Wang, Y. Ma, G. Jia, Y. Gao, B. Li, J. Sun, *et al.*, "Acute Toxicity and Biodistribution of Different Sized Titanium Dioxide Particles in Mice After Oral Administration," *Toxicol. Lett.*, vol. 168, no. 2, pp. 176–185, 2007.

[23] A. Fujishima and K. Honda, "Electrochemical Photolysis of Water at a Semiconductor Electrode," *Nature*, vol. 238, no. 5358, p. 37, 1972.

[24] N. L. De Silva, A. C. Jayasundera, A. Folger, O. Kasian, S. Zhang, C.-F. Yan, C. Scheu, and J. Bandara, "Superior Solar-to-Hydrogen Energy Conversion Efficiency by Visible Light-driven Hydrogen Production via Highly Reduced Ti^{2+}/Ti^{3+} States in a Blue Titanium Dioxide Photocatalyst," *Catal. Sci. Technol.*, vol. 8, no. 18, pp. 4657–4664, 2018.

[25] S. G. Kumar and L. G. Devi, "Review on Modified TiO_2 Photocatalysis Under UV/visible Light: Selected Results and Related Mechanisms on Interfacial Charge Carrier Transfer Dynamics," *J. Phys. Chem. A*, vol. 115, no. 46, pp. 13211–13241, 2011.

[26] D. Friedmann, C. Mendive, and D. Bahnemann, "TiO_2 for Water Treatment: Parameters Affecting the Kinetics and Mechanisms of Photocatalysis," *Appl. Catal. B-Environ.*, vol. 99, no. 3-4, pp. 398–406, 2010.

[27] D. S. Dharmagunawardhane, N. L. De Silva, U. B. Gunatilake, C.-F. Yan, and J. Bandara, "Removal of Groundwater Nitrates by Heterogeneous Supramolecular Complexes-Like Photocatalytic System Based on In-Situ Generated and Highly Active Ti^{2+}/Ti^{3+} States in the Reduced TiO_2," *Mol. Catal.*, vol. 470, pp. 89–96, 2019.

[28] J. Wang, R. Li, Z. Zhang, W. Sun, Y. Xie, R. Xu, Z. Xing, and X. Zhang, "Solar Photocatalytic Degradation of Dye Wastewater in the Presence of Heat-treated Anatase TiO_2 Powder," *Environ. Prog.*, vol. 27, no. 2, pp. 242–249, 2008.

[29] V. Scuderi, G. Impellizzeri, L. Romano, M. Scuderi, M. V. Brundo, K. Bergum, M. Zimbone, R. Sanz, M. A. Buccheri, F. Simone, *et al.*, "An Enhanced Photocatalytic Response of Nanometric TiO_2 Wrapping of Au Nanoparticles for Eco-friendly Water Applications," *Nanoscale*, vol. 6, no. 19, pp. 11189–11195, 2014.

[30] B. O'regan and M. Grätzel, "A Low-Cost, High-Efficiency Solar Cell Based on Dye-Sensitized Colloidal TiO_2 Films," *Nature*, vol. 353, no. 6346, p. 737, 1991.

[31] Y. Bai, I. Mora-Sero, F. De Angelis, J. Bisquert, and P. Wang, "Titanium Dioxide Nanomaterials for Photovoltaic Applications," *Chem. Rev.*, vol. 114, no. 19, pp. 10095–10130, 2014.

[32] H.-S. Kim, J.-W. Lee, N. Yantara, P. P. Boix, S. A. Kulkarni, S. Mhaisalkar, M. Grätzel, and N.-G. Park, "High Efficiency Solid-State Sensitized Solar Cell-Based on Submicrometer Rutile TiO_2 Nanorod and $CH_3NH_3PbI_3$ Perovskite Sensitizer," *Nano Lett.*, vol. 13, no. 6, pp. 2412–2417, 2013.

[33] M. Yang, D. Kim, H. Jha, K. Lee, J. Paul, and P. Schmuki, "Nb doping of TiO_2 Nanotubes for an Enhanced Efficiency of Dye-Sensitized Solar Cells," *Chem. Commun.*, vol. 47, no. 7, pp. 2032–2034, 2011.

[34] J. S. Chen, Y. L. Tan, C. M. Li, Y. L. Cheah, D. Luan, S. Madhavi, F. Y. C. Boey, L. A. Archer, and X. W. Lou, "Constructing Hierarchical Spheres From Large Ultrathin Anatase TiO_2 Nanosheets With Nearly 100% Exposed (001) Facets for Fast Reversible Lithium Storage," *J. Am. Chem. Soc.*, vol. 132, no. 17, pp. 6124–6130, 2010.

[35] L. Kavan, M. Grätzel, J. Rathouskỳ, and A. Zukalb, "Nanocrystalline TiO_2 (Anatase) Electrodes: Surface Morphology, Adsorption, and Electrochemical Properties," *J. Electrochem. Soc.*, vol. 143, no. 2, p. 394, 1996.

[36] S.-T. Myung, M. Kikuchi, C. S. Yoon, H. Yashiro, S.-J. Kim, Y.-K. Sun, and B. Scrosati, "Black Anatase Titania Enabling Ultra High Cycling Rates for Rechargeable Lithium Batteries," *Energy Environ. Sci.*, vol. 6, no. 9, pp. 2609–2614, 2013.

[37] Y. Xu, E. M. Lotfabad, H. Wang, B. Farbod, Z. Xu, A. Kohandehghan, and D. Mitlin, "Nanocrystalline Anatase TiO_2: a New Anode Material for Rechargeable Sodium Ion Batteries," *Chem. Commun.*, vol. 49, no. 79, pp. 8973–8975, 2013.

[38] Y.-G. Guo, Y.-S. Hu, W. Sigle, and J. Maier, "Superior Electrode Performance of Nanostructured Mesoporous TiO_2 (Anatase) Through Efficient Hierarchical Mixed Conducting Networks," *Adv. Mater.*, vol. 19, no. 16, pp. 2087–2091, 2007.

[39] G. F. Ortiz, I. Hanzu, T. Djenizian, P. Lavela, J. L. Tirado, and P. Knauth, "Alternative Li-Ion Battery Electrode Based on Self-Organized Titania Nanotubes," *Chem. Mater.*, vol. 21, no. 1, pp. 63–67, 2008.

[40] J. Dawson and J. Robertson, "Improved Calculation of Li and Na Intercalation Properties in Anatase, Rutile, and TiO_2(B)," *J. Phys. Chem. C*, vol. 120, no. 40, pp. 22910–22917, 2016.

[41] A. Sclafani and J. Herrmann, "Comparison of the Photoelectronic and Photocatalytic Activities of Various Anatase and Rutile forms of Titania in Pure Liquid Organic Phases and in Aqueous Solutions," *J. Phys. Chem.*, vol. 100, no. 32, pp. 13655–13661, 1996.

[42] T. Sumita, T. Yamaki, S. Yamamoto, and A. Miyashita, "Photo-Induced Surface Charge Separation of Highly Oriented TiO_2 Anatase and Rutile Thin Films," *Appl. Surf. Sci.*, vol. 200, no. 1-4, pp. 21–26, 2002.

[43] T. Watanabe, A. Nakajima, R. Wang, M. Minabe, S. Koizumi, A. Fujishima, and K. Hashimoto, "Photocatalytic Activity and Photoinduced Hydrophilicity of Titanium Dioxide Coated Glass," *Thin solid films*, vol. 351, no. 1-2, pp. 260–263, 1999.

[44] P. Mazzolini, P. Gondoni, V. Russo, D. Chrastina, C. S. Casari, and A. Li Bassi, "Tuning of Electrical and Optical Properties of Highly Conducting and Transparent Ta-doped TiO_2 Polycrystalline Films," *J. Phys. Chem. C*, vol. 119, no. 13, pp. 6988–6997, 2015.

[45] H.-Y. Lee and J. Robertson, "Doping and Compensation in Nb-doped Anatase and Rutile TiO_2," *J. Appl. Phys.*, vol. 113, no. 21, p. 213706, 2013.

[46] B. J. Morgan, D. O. Scanlon, and G. W. Watson, "Small Polarons in Nb-and Ta-doped Rutile and Anatase TiO_2," *J. Mater. Chem.*, vol. 19, no. 29, pp. 5175–5178, 2009.

[47] S. Zhang, D. Kundaliya, W. Yu, S. Dhar, S. Young, L. Salamanca-Riba, S. Ogale, R. Vispute, and T. Venkatesan, "Niobium Doped TiO_2: Intrinsic Transparent Metallic Anatase Versus Highly Resistive Rutile Phase," *J. Appl. Phys.*, vol. 102, no. 1, p. 013701, 2007.

[48] Y. Furubayashi, T. Hitosugi, Y. Yamamoto, K. Inaba, G. Kinoda, Y. Hirose, T. Shimada, and T. Hasegawa, "A Transparent Metal: Nb-doped Anatase TiO_2," *Appl. Phys. Lett.*, vol. 86, no. 25, p. 252101, 2005.

[49] C. Di Valentin, "A Mechanism for the Hole-Mediated Water Photooxidation on TiO_2 (101) Surfaces," *J. Phys-Condens. Mat.*, vol. 28, no. 7, p. 074002, 2016.

[50] T. Ohsawa, I. V. Lyubinetsky, M. A. Henderson, and S. A. Chambers, "Hole-Mediated Photodecomposition of Trimethyl Acetate on a TiO_2 (001) Anatase Epitaxial Thin Film Surface," *J. Phys. Chem. C*, vol. 112, no. 50, pp. 20050–20056, 2008.

[51] D. Luo, R. Su, W. Zhang, Q. Gong, and R. Zhu, "Minimizing Non-Radiative Recombination Losses in Perovskite Solar Cells," *Nat. Rev. Mater.*, vol. 5, no. 1, pp. 44–60, 2020.

[52] D. Lang and C. Henry, "Nonradiative Recombination at Deep Levels in GaAs and GaP by Lattice-Relaxation Multiphonon Emission," *Phys. Rev. Lett.*, vol. 35, no. 22, p. 1525, 1975.

[53] B. J. Morgan and G. W. Watson, "A DFT+U Description of Oxygen Vacancies at the TiO_2 Rutile (110) Surface," *Surf. Sci.*, vol. 601, no. 21, pp. 5034–5041, 2007.

[54] A. R. Elmaslmane, *Localised Electronic States in Model Systems and Semiconductors*. PhD thesis, University of York, November 2019.

[55] S. Yang, A. Brant, N. Giles, and L. Halliburton, "Intrinsic Small Polarons in Rutile TiO_2," *Phys. Rev. B*, vol. 87, no. 12, p. 125201, 2013.

[56] T. Berger, M. Sterrer, O. Diwald, E. Knözinger, D. Panayotov, T. L. Thompson, and J. T. Yates, "Light-Induced Charge Separation in Anatase TiO_2 Particles," *J. Phys. Chem. B*, vol. 109, no. 13, pp. 6061–6068, 2005.

[57] A. R. Elmaslmane, M. B. Watkins, and K. P. McKenna, "First-Principles Modeling of Polaron Formation in TiO_2 Polymorphs," *J. Chem. Theory Comput.*, vol. 14, no. 7, pp. 3740–3751, 2018.

[58] E. Baldini, L. Chiodo, A. Dominguez, M. Palummo, S. Moser, M. Yazdi-Rizi, G. Auböck, B. P. Mallett, H. Berger, A. Magrez, *et al.*, "Strongly Bound Excitons in Anatase TiO_2 Single Crystals and Nanoparticles," *Nat. Commun.*, vol. 8, no. 1, pp. 1–11, 2017.

[59] C. P. Kumar, N. O. Gopal, T. C. Wang, M.-S. Wong, and S. C. Ke, "EPR Investigation of TiO_2 Nanoparticles with Temperature-Dependent Properties," *J. Phys. Chem. B*, vol. 110, no. 11, pp. 5223–5229, 2006.

[60] D. K. Pallotti, L. Passoni, P. Maddalena, F. Di Fonzo, and S. Lettieri, "Photoluminescence Mechanisms in Anatase and Rutile TiO_2," *J. Phys. Chem. C*, vol. 121, no. 16, pp. 9011–9021, 2017.

[61] M. Gallart, T. Cottineau, B. Hönerlage, V. Keller, N. Keller, and P. Gilliot, "Temperature Dependent Photoluminescence of Anatase and Rutile TiO_2 Single Crystals: Polaron and Self-Trapped Exciton Formation," *J. Appl. Phys.*, vol. 124, no. 13, p. 133104, 2018.

[62] M. Watanabe, S. Sasaki, and T. Hayashi, "Time-Resolved Study of Photoluminescence in Anatase TiO_2," *J. Lumin.*, vol. 87, pp. 1234–1236, 2000.

[63] T. Bak, M. K. Nowotny, L. R. Sheppard, and J. Nowotny, "Mobility of Electronic Charge Carriers in Titanium Dioxide," *J. Phys. Chem. C*, vol. 112, no. 33, pp. 12981–12987, 2008.

[64] K. K. Rao, S. N. Naidu, and L. Iyengar, "Thermal Expansion of Rutile and Anatase," *J. Am. Ceram. Soc.*, vol. 53, no. 3, pp. 124–126, 1970.

[65] R. L. Penn and J. F. Banfield, "Formation of Rutile Nuclei at Anatase {112} Twin Interfaces and the Phase Transformation Mechanism in Nanocrystalline Titania," *Am. Mineral.*, vol. 84, no. 5-6, pp. 871–876, 1999.

[66] R. L. Penn and J. F. Banfield, "Oriented Attachment and Growth, Twinning, Polytypism, and Formation of Metastable Phases: Insights From Nanocrystalline TiO_2," *Am. Mineral.*, vol. 83, no. 9-10, pp. 1077–1082, 1998.

[67] R. L. Penn and J. F. Banfield, "Morphology Development and Crystal Growth in Nanocrystalline Aggregates Under Hydrothermal Conditions: Insights From Titania," *Geochim. Cosmochim. Ac.*, vol. 63, no. 10, pp. 1549–1557, 1999.

[68] A. A. Gribb and J. F. Banfield, "Particle Size Effects on Transformation Kinetics and Phase Stability in Nanocrystalline TiO_2," *Am. Miner.*, vol. 82, no. 7-8, pp. 717–728, 1997.

[69] M. Grätzel, "Sol-Gel Processed TiO_2 Films for Photovoltaic Applications," *J. Sol-Gel Sci. Techn.*, vol. 22, no. 1-2, pp. 7–13, 2001.

[70] J. J. Carey and K. P. McKenna, "Does Polaronic Self-Trapping Occur at Anatase TiO_2 Surfaces?," *J. Phys. Chem. C*, vol. 122, no. 48, pp. 27540–27553, 2018.

[71] T. Luttrell, S. Halpegamage, J. Tao, A. Kramer, E. Sutter, and M. Batzill, "Why is Anatase a Better Photocatalyst than Rutile? Model studies on Epitaxial TiO_2 Films," *Sci. Rep.*, vol. 4, no. 1, pp. 1–8, 2014.

[72] T. Peng, D. Zhao, K. Dai, W. Shi, and K. Hirao, "Synthesis of Titanium Dioxide Nanoparticles with Mesoporous Anatase Wall and High Photocatalytic Activity," *J. Phys. Chem. B*, vol. 109, no. 11, pp. 4947–4952, 2005.

[73] Y. P. Lin, S. Y. Lin, Y. C. Lee, and Y. W. Chen-Yang, "High Surface Area Electrospun Prickle-Like Hierarchical Anatase TiO_2 Nanofibers for Dye-Sensitized Solar Cell Photoanodes," *J. Mater. Chem. A*, vol. 1, no. 34, pp. 9875–9884, 2013.

[74] C. Li, Y. Wu, J. Poplawsky, T. J. Pennycook, N. Paudel, W. Yin, S. J. Haigh, M. P. Oxley, A. R. Lupini, M. Al-Jassim, *et al.*, "Grain-Boundary-Enhanced Carrier Collection in CdTe Solar Cells," *Phys. Rev. Lett.*, vol. 112, no. 15, p. 156103, 2014.

[75] S. Sasano, R. Ishikawa, K. Kawahara, T. Kimura, Y. H. Ikuhara, N. Shibata, and Y. Ikuhara, "Grain Boundary Li-ion Conductivity in $(Li_{0\cdot33}La_{0\cdot56})TiO_3$ Polycrystal," *Appl. Phys. Lett.*, vol. 116, no. 4, p. 043901, 2020.

[76] A. R. Symington, M. Molinari, J. A. Dawson, J. M. Statham, J. Purton, P. Canepa, and S. C. Parker, "Elucidating the Nature of Grain Boundary Resistance in Lithium Lanthanum Titanate," *J. Mater. Chem. A*, 2021.

[77] C.-J. Tong and K. P. McKenna, "Passivating Grain Boundaries in Polycrystalline CdTe," *J. Phys. Chem. C*, vol. 123, no. 39, pp. 23882–23889, 2019.

[78] J. J. Carey and K. P. McKenna, "Screening Doping Strategies to Mitigate Electron Trapping at Anatase TiO_2 Surfaces," *J. Phys. Chem. C*, vol. 123, no. 36, pp. 22358–22367, 2019.

[79] C. W. Ban and G. M. Choi, "The Effect of Sintering on the Grain Boundary Conductivity of Lithium Lanthanum Titanates," *Solid State Ion.*, vol. 140, no. 3-4, pp. 285–292, 2001.

[80] T. Gansum, "Role the Bones–from Iron to Steel," *Norwegian Archaeological Review*, vol. 37, no. 1, pp. 41–57, 2004.

[81] C. Catlow, C. Freeman, M. Islam, R. Jackson, M. Leslie, and S. Tomlinson, "Interatomic Potentials for Oxides," *Philos. Mag.*, vol. 58, no. 1, pp. 123–141, 1988.

[82] P. Hohenberg and W. Kohn, "Inhomogeneous Electron Gas," *Physical review*, vol. 136, no. 3B, p. B864, 1964.

[83] W. Kohn and L. J. Sham, "Self-Consistent Equations Including Exchange and Correlation Effects," *Phys. Rev.*, vol. 140, no. 4A, p. A1133, 1965.

[84] Y. Zhang and W. Yang, "A Challenge for Density Functionals: Self-Interaction Error Increases for Systems With a Noninteger Number of Electrons," *J. Chem. Phys.*, vol. 109, no. 7, pp. 2604–2608, 1998.

[85] A. D. Becke, "A New Mixing of Hartree-Fock and Local Density-Functional Theories," *J. Chem. Phys.*, vol. 98, no. 2, pp. 1372–1377, 1993.

[86] A. Elmaslmane, J. Wetherell, M. Hodgson, K. McKenna, and R. Godby, "Accuracy of Electron Densities Obtained via Koopmans-Compliant Hybrid Functionals," *Phys. Rev. Mater.*, vol. 2, no. 4, p. 040801, 2018.

[87] J. P. Perdew, K. Burke, and M. Ernzerhof, "Generalized Gradient Approximation Made Simple," *Phys. Rev. Lett.*, vol. 77, no. 18, p. 3865, 1996.

[88] R. Van Leeuwen and E. Baerends, "Exchange-Correlation Potential with Correct Asymptotic Behavior," *Phys. Rev. A*, vol. 49, no. 4, p. 2421, 1994.

[89] A. P. Gaiduk, S. K. Chulkov, and V. N. Staroverov, "Reconstruction of Density Functionals from Kohn- Sham Potentials by Integration along Density Scaling Paths," *J. Chem. Theory Comput.*, vol. 5, no. 4, pp. 699–707, 2009.

[90] M. G. Medvedev, I. S. Bushmarinov, J. Sun, J. P. Perdew, and K. A. Lyssenko, "Density Functional Theory is Straying From the Path Toward the Exact Functional," *Science*, vol. 355, no. 6320, pp. 49–52, 2017.

[91] J. Sun, A. Ruzsinszky, and J. P. Perdew, "Strongly Constrained and Appropriately Normed Semilocal Density Functional," *Phys. Rev. Lett.*, vol. 115, no. 3, p. 036402, 2015.

[92] J. Sun, R. C. Remsing, Y. Zhang, Z. Sun, A. Ruzsinszky, H. Peng, Z. Yang, A. Paul, U. Waghmare, X. Wu, *et al.*, "Accurate First-Principles Structures and Energies of Diversely Bonded Systems From an Efficient Density Functional," *Nat. Chem.*, vol. 8, no. 9, p. 831, 2016.

[93] R. Godby, M. Schlüter, and L. Sham, "Accurate Exchange-Correlation Potential for Silicon and its Discontinuity on Addition of an Electron," *Phys. Rev. Lett.*, vol. 56, no. 22, p. 2415, 1986.

[94] V. I. Anisimov, J. Zaanen, and O. K. Andersen, "Band theory and mott insulators: Hubbard u instead of stoner i," *Phys. Rev. B*, vol. 44, no. 3, p. 943, 1991.

[95] J. Hubbard, "Electron correlations in narrow energy bands," *Proc. R. Soc. Lond. A*, vol. 276, no. 1365, pp. 238–257, 1963.

[96] M. Cococcioni and S. De Gironcoli, "Linear response approach to the calculation of the effective interaction parameters in the lda+u method," *Phys. Rev. B*, vol. 71, no. 3, p. 035105, 2005.

[97] M. Yu, S. Yang, C. Wu, and N. Marom, "Machine learning the hubbard u parameter in dft+u using bayesian optimization," *Npj Comput. Mater.*, vol. 6, no. 1, pp. 1–6, 2020.

[98] L. Wang, T. Maxisch, and G. Ceder, "Oxidation energies of transition metal oxides within the gga+u framework," *Phys. Rev. B*, vol. 73, no. 19, p. 195107, 2006.

[99] M. Arroyo-de Dompablo, A. Morales-García, and M. Taravillo, "Dft+u calculations of crystal lattice, electronic structure, and phase stability under pressure of TiO_2 polymorphs," *J. Chem. Phys.*, vol. 135, no. 5, p. 054503, 2011.

[100] E. Shojaee, M. Abbasnejad, M. Saeedian, and M. Mohammadizadeh, "First-principles study of lattice dynamics of TiO_2 in brookite and cotunnite structures," *Phys. Rev. B*, vol. 83, no. 17, p. 174302, 2011.

[101] G. S. Gautam and E. A. Carter, "Evaluating transition metal oxides within dft-scan and scan+u frameworks for solar thermochemical applications," *Phys. Rev. Mater.*, vol. 2, no. 9, p. 095401, 2018.

[102] J. A. Quirk, V. K. Lazarov, and K. P. McKenna, "First-Principles Modeling of Oxygen-Deficient Anatase TiO_2 Nanoparticles," *J. Phys. Chem. C*, vol. 124, no. 43, pp. 23637–23647, 2020.

[103] J. P. Perdew, M. Ernzerhof, and K. Burke, "Rationale for Mixing Exact Exchange With Density Functional Approximations," *J. Chem. Phys.*, vol. 105, no. 22, pp. 9982–9985, 1996.

[104] K. Burke, M. Ernzerhof, and J. P. Perdew, "The Adiabatic Connection Method: a Non-Empirical Hybrid," *Chem. Phys. Lett.*, vol. 265, no. 1-2, pp. 115–120, 1997.

[105] D. Zhang and D. G. Truhlar, "Unmasking Static Correlation Error in Hybrid Kohn-Sham Density Functional Theory," *J. Chem. Theory Comput.*, vol. 16, no. 9, pp. 5432–5440, 2020.

[106] P. Deák, A. Gali, A. Sólyom, A. Buruzs, and T. Frauenheim, "Electronic Structure of Boron-Interstitial Clusters in Silicon," *J. Phys. Condens. Matter*, vol. 17, no. 22, p. S2141, 2005.

[107] J. Lyons, A. Janotti, and C. Van de Walle, "Carbon Impurities and the Yellow Luminescence in GaN," *Appl. Phys. Lett.*, vol. 97, no. 15, p. 152108, 2010.

[108] A. Alkauskas, P. Broqvist, and A. Pasquarello, "Defect Levels Through Hybrid Density Functionals: Insights and Applications," *Phys. Status Solidi B*, vol. 248, no. 4, pp. 775–789, 2011.

[109] A. Di Paola, M. Bellardita, and L. Palmisano, "Brookite, the Least Known TiO_2 Photocatalyst," *Catalysts*, vol. 3, no. 1, pp. 36–73, 2013.

[110] A. Alkauskas, J. L. Lyons, D. Steiauf, and C. G. Van de Walle, "First-Principles Calculations of Luminescence Spectrum Line Shapes for Defects in Semiconductors: the Example of GaN and ZnO," *Phys. Rev. Lett.*, vol. 109, no. 26, p. 267401, 2012.

[111] Z.-H. Cui, Y.-C. Wang, M.-Y. Zhang, X. Xu, and H. Jiang, "Doubly Screened Hybrid Functional: an Accurate First-Principles Approach for Both Narrow- and Wide-gap Semiconductors," *J. Phys. Chem. Lett.*, vol. 9, no. 9, pp. 2338–2345, 2018.

[112] J. H. Skone, M. Govoni, and G. Galli, "Self-Consistent Hybrid Functional for Condensed Systems," *Phys. Rev. B*, vol. 89, no. 19, p. 195112, 2014.

[113] M. Srebro and J. Autschbach, "Does a Molecule-Specific Density Functional Give an Accurate Electron Density? The Challenging Case of the CuCl Electric Field Gradient," *J. Phys. Chem. Lett.*, vol. 3, no. 5, pp. 576–581, 2012.

[114] M. Srebro and J. Autschbach, "Tuned Range-separated Time-Dependent Density Functional Theory Applied to Optical Rotation," *J. Chem. Theory Comput.*, vol. 8, no. 1, pp. 245–256, 2012.

[115] L. Kronik, T. Stein, S. Refaely-Abramson, and R. Baer, "Excitation Gaps of Finite-Sized Systems From Optimally Tuned Range-Separated Hybrid Functionals," *J. Chem. Theory Comput.*, vol. 8, no. 5, pp. 1515–1531, 2012.

[116] V. Vlček, H. R. Eisenberg, G. Steinle-Neumann, L. Kronik, and R. Baer, "Deviations From Piecewise Linearity in the Solid-State Limit With Approximate Density Functionals," *J. Chem. Phys.*, vol. 142, no. 3, p. 034107, 2015.

[117] R. Nada, C. Catlow, C. Pisani, and R. Orlando, "An Ab-initio Hartree-Fock Perturbed-Cluster Study of Neutral Defects in LiF," *Model. Simul. Mater. Sci. Eng*, vol. 1, no. 2, p. 165, 1993.

[118] H. Shi, R. Eglitis, and G. Borstel, "Ab-initio Calculations of the BaF_2 Bulk and Surface F-centres," *J. Phys. Condens. Matter*, vol. 18, no. 35, p. 8367, 2006.

[119] T. Tada, S. Takemoto, S. Matsuishi, and H. Hosono, "High-Throughput Ab Initio Screening for Two-Dimensional Electride Materials," *Inorg. Chem.*, vol. 53, no. 19, pp. 10347–10358, 2014.

[120] M. A. Spackman and A. S. Mitchell, "Basis Set Choice and Basis Set Superposition Error (BSSE) in Periodic Hartree–Fock Calculations on Molecular Crystals," *Phys. Chem. Chem. Phys.*, vol. 3, no. 8, pp. 1518–1523, 2001.

[121] C. Hartwigsen, S. Gœdecker, and J. Hutter, "Relativistic Separable Dual-Space Gaussian Pseudopotentials From H to Rn," *Phys. Rev. B*, vol. 58, no. 7, p. 3641, 1998.

[122] S. Goedecker, M. Teter, and J. Hutter, "Separable Dual-space Gaussian Pseudopotentials," *Phys. Rev. B*, vol. 54, no. 3, p. 1703, 1996.

[123] M. Krack, "Pseudopotentials for H to Kr Optimized for Gradient-Corrected Exchange-Correlation Functionals," *Theor. Chem. Acc.*, vol. 114, no. 1-3, pp. 145–152, 2005.

[124] J. Spencer and A. Alavi, "Efficient Calculation of the Exact Exchange Energy in Periodic Systems Using a Truncated Coulomb Potential," *Phys. Rev. B*, vol. 77, no. 19, p. 193110, 2008.

[125] J. VandeVondele and J. Hutter, "Gaussian Basis Sets for Accurate Calculations on Molecular Systems in Gas and Condensed Phases," *J. Chem. Phys.*, vol. 127, no. 11, p. 114105, 2007.

[126] P. E. Blöchl, "Projector Augmented-Wave Method," *Phys. Rev. B*, vol. 50, no. 24, p. 17953, 1994.

[127] G. Kresse and D. Joubert, "From Ultrasoft Pseudopotentials to the Projector Augmented-wave Method," *Phys. Rev. B*, vol. 59, no. 3, p. 1758, 1999.

[128] F. Kröger and H. Vink, "Relations between the concentrations of imperfections in crystalline solids," *Solid State Phys.*, vol. 3, pp. 307–435, 1956.

[129] D. Ohnenstetter, A. Fallick, and A. Fagan, *The Geology and Genesis of Gem Corundum Deposits*, vol. 2. Mineralogical Association of Canada, 2 ed., 2007.

[130] A. Peaker, V. Markevich, B. Hamilton, G. Parada, A. Dudas, A. Pap, E. Don, B. Lim, J. Schmidt, L. Yu, *et al.*, "Recombination via Point Defects and Their

Complexes in Solar Silicon," *Phys. Status Solidi C*, vol. 209, no. 10, pp. 1884–1893, 2012.

[131] A. Chernyakov, M. Sobolev, V. Ratnikov, N. Shmidt, and E. Yakimov, "Nonradiative Recombination Dynamics in InGaN/GaN LED Defect system," *Superlattice Microstruct*, vol. 45, no. 4-5, pp. 301–307, 2009.

[132] C. Freysoldt, B. Grabowski, T. Hickel, J. Neugebauer, G. Kresse, A. Janotti, and C. G. Van de Walle, "First-Principles Calculations for Point Defects in Solids," *Rev. Mod. Phys*, vol. 86, no. 1, p. 253, 2014.

[133] C. Freysoldt, J. Neugebauer, and C. G. Van de Walle, "Fully ab initio finite-size corrections for charged-defect supercell calculations," *Phys. Rev. Lett.*, vol. 102, no. 1, p. 016402, 2009.

[134] T. Durrant, S. Murphy, M. Watkins, and A. Shluger, "Relation between image charge and potential alignment corrections for charged defects in periodic boundary conditions," *J. Chem. Phys.*, vol. 149, no. 2, p. 024103, 2018.

[135] G. Makov and M. Payne, "Periodic boundary conditions in ab initio calculations," *Phys. Rev. B*, vol. 51, no. 7, p. 4014, 1995.

[136] J. Buckeridge, "Equilibrium Point Defect and Charge Carrier Concentrations in a Material Determined Through Calculation of the Self-Consistent Fermi Energy," *Comput. Phys. Commun*, vol. 244, pp. 329–342, 2019.

[137] S. F. Boys and F. Bernardi, "The Calculation of Small Molecular Interactions by the Differences of Separate Total Energies. Some Procedures with Reduced Errors," *Mol. Phys.*, vol. 19, no. 4, pp. 553–566, 1970.

[138] A. Alkauskas, Q. Yan, and C. G. Van de Walle, "First-Principles Theory of Nonradiative Carrier Capture via Multiphonon Emission," *Phys. Rev. B*, vol. 90, no. 7, p. 075202, 2014.

[139] J. J. Carey, J. A. Quirk, and K. P. McKenna, "Hole polaron migration in bulk phases of TiO_2 using hybrid density functional theory," *J. Phys. Chem. C*, 2021.

[140] H.-Y. Lee, S. J. Clark, J. Robertson, *et al.*, "Calculation of Point Defects in Rutile TiO_2 by the Screened-exchange Hybrid Functional," *Phys. Rev. B*, vol. 86, no. 7, p. 075209, 2012.

[141] S. Na-Phattalung, M. F. Smith, K. Kim, M.-H. Du, S.-H. Wei, S. Zhang, and S. Limpijumnong, "First-Principles Study of Native Defects in Anatase TiO_2," *Phys. Rev. B*, vol. 73, no. 12, p. 125205, 2006.

[142] W. Sun and G. Ceder, "Efficient Creation and Convergence of Surface Slabs," *Surf. Sci*, vol. 617, pp. 53–59, 2013.

[143] J. Fierro and L. G. Tejuca, "Non-Stoichiometric Surface Behaviour of $LaMO_3$ Oxides as Evidenced by XPS," *Appl. Surf. Sci.*, vol. 27, no. 4, pp. 453–457, 1987.

[144] A. Y. Cho and J. Arthur, "Molecular Beam Epitaxy," *Prog. Solid State Ch.*, vol. 10, pp. 157–191, 1975.

[145] W. Wang, W. Bowen, S. Spanninga, S. Lin, and J. Phillips, "Optical Characteristics of ZnTeO Thin Films Synthesized by Pulsed Laser Deposition and Molecular Beam Epitaxy," *J. Electron. Mater.*, vol. 38, no. 1, pp. 119–125, 2009.

[146] F. Wrobel, A. Mark, G. Christiani, W. Sigle, H.-U. Habermeier, P. van Aken, G. Logvenov, B. Keimer, and E. Benckiser, "Comparative Study of $LaNiO_3/LaAlO_3$ Heterostructures Grown by Pulsed Laser Deposition and Oxide Molecular Beam Epitaxy," *Appl. Phys. Lett.*, vol. 110, no. 4, p. 041606, 2017.

[147] D. H. Lowndes, D. Geohegan, A. Puretzky, D. Norton, and C. Rouleau, "Synthesis of Novel Thin-Film Materials by Pulsed Laser Deposition," *Science*, vol. 273, no. 5277, pp. 898–903, 1996.

[148] G. Wulff, "Xxv. zur frage der geschwindigkeit des wachsthums und der auflösung der krystallflächen," *Z. Kristallogr. Cryst. Mater*, vol. 34, no. 1-6, pp. 449–530, 1901.

[149] J. Rahm and P. Erhart, "WulffPack: A Python Package for Wulff Constructions," *J. Open Source Softw.*, vol. 5, no. 45, p. 1944, 2020.

[150] K. P. McKenna, "Structure, Electronic Properties, and Oxygen Incorporation/Diffusion Characteristics of the Σ5 TiN (310)[001] Tilt Grain Boundary," *J. Appl. Phys*, vol. 123, no. 7, p. 075301, 2018.

[151] J. J. Bean and K. P. McKenna, "Origin of Differences in the Excess Volume of Copper and Nickel Grain Boundaries," *Acta Mater.*, vol. 110, pp. 246–257, 2016.

[152] S. Von Alfthan, P. Haynes, K. Kaski, and A. Sutton, "Are the Structures of Twist Grain Boundaries in Silicon Ordered at 0 K?," *Phys. Rev. Lett.*, vol. 96, no. 5, p. 055505, 2006.

[153] G. Schusteritsch and C. J. Pickard, "Predicting Interface Structures: From $SrTiO_3$ to Graphene," *Phys. Rev. B*, vol. 90, no. 3, p. 035424, 2014.

[154] M. Imaeda, T. Mizoguchi, Y. Sato, H.-S. Lee, S. Findlay, N. Shibata, T. Yamamoto, and Y. Ikuhara, "Atomic Structure, Electronic Structure, and Defect Energetics in [001](310) Σ 5 Grain Boundaries of $SrTiO_3$ and $BaTiO_3$," *Phys. Rev. B*, vol. 78, no. 24, p. 245320, 2008.

[155] H.-S. Lee, T. Mizoguchi, J. Mistui, T. Yamamoto, S.-J. Kang, and Y. Ikuhara, "Defect Energetics in $SrTiO_3$ Symmetric Tilt Grain Boundaries," *Phys. Rev. B*, vol. 83, no. 10, p. 104110, 2011.

[156] X. Gao, Y. H. Ikuhara, C. A. Fisher, R. Huang, A. Kuwabara, H. Moriwake, K. Kohama, and Y. Ikuhara, "Oxygen Loss and Surface Degradation During Electrochemical Cycling of Lithium-ion Battery Cathode Material $LiMn_2O_4$," *J. Mater. Chem. A*, vol. 7, no. 15, pp. 8845–8854, 2019.

[157] G. L. Wellock and B. J. Morgan, "pyscses: a PYthon Space-Charge Site-Explicit Solver," *J. Open Source Softw.*, vol. 4, no. 35, p. 1209, 2019.

[158] W. Yuan, J. Meng, B. Zhu, Y. Gao, Z. Zhang, C. Sun, and Y. Wang, "Unveiling the Atomic Structures of the Minority Surfaces of TiO_2 Nanocrystals," *Chem. Mater.*, vol. 30, no. 1, pp. 288–295, 2018.

[159] H. Kim, J. Y. Zhang, S. Raghavan, and S. Stemmer, "Direct Observation of Sr Vacancies in $SrTiO_3$ by Quantitative Scanning Transmission Electron Microscopy," *Phys. Rev. X*, vol. 6, no. 4, p. 041063, 2016.

[160] E. Okunishi, I. Ishikawa, H. Sawada, F. Hosokawa, M. Hori, and Y. Kondo, "Visualization of Light Elements at Ultrahigh Resolution by STEM Annular Bright Field Microscopy," *Microsc. Microanal*, vol. 15, no. S2, pp. 164–165, 2009.

[161] R. Ishikawa, E. Okunishi, H. Sawada, Y. Kondo, F. Hosokawa, and E. Abe, "Direct Imaging of Hydrogen-Atom Columns in a Crystal by Annular Bright-Field Electron Microscopy," *Nat. Mater.*, vol. 10, no. 4, p. 278, 2011.

[162] M. Haider, S. Uhlemann, E. Schwan, H. Rose, B. Kabius, and K. Urban, "Electron Microscopy Image Enhanced," *Nature*, vol. 392, no. 6678, pp. 768–769, 1998.

[163] C. T. Koch, *Determination of Core Structure Periodicity and Point Defect Density Along Dislocations*. PhD thesis, Arizona State University, 2002.

[164] E. J. Kirkland, *Advanced Computing in Electron Microscopy*. Springer, 1998.

[165] Y. Liang, S. Gan, S. A. Chambers, and E. I. Altman, "Surface Structure of Anatase TiO_2 (001): Reconstruction, Atomic Steps, and Domains," *Phys. Rev. B*, vol. 63, no. 23, p. 235402, 2001.

[166] M. Setvin, C. Franchini, X. Hao, M. Schmid, A. Janotti, M. Kaltak, C. G. Van de Walle, G. Kresse, and U. Diebold, "Direct View at Excess Electrons in TiO_2 Rutile and Anatase," *Phys. Rev. Lett.*, vol. 113, no. 8, p. 086402, 2014.

[167] M. Setvin, X. Hao, B. Daniel, J. Pavelec, Z. Novotny, G. S. Parkinson, M. Schmid, G. Kresse, C. Franchini, and U. Diebold, "Charge Trapping at the Step Edges of TiO_2 Anatase (101)," *Angew. Chem.*, vol. 53, no. 18, pp. 4714–4716, 2014.

[168] J. Tersoff and D. Hamann, "Theory of the Scanning Tunneling Microscope," *Phys. Rev. B*, vol. 31, no. 2, p. 805, 1985.

[169] J. A. Quirk, V. K. Lazarov, and K. P. McKenna, "Electronic Properties of {112} and {110} Twin Boundaries in Anatase TiO_2," *Adv. Theory Simul.*, vol. 2, no. 12, p. 1900157, 2019.

[170] P. I. Gouma and M. J. Mills, "Anatase-To-Rutile Transformation in Titania Powders," *J. Am. Ceram. Soc.*, vol. 84, no. 3, pp. 619–622, 2001.

[171] H. Seo, A. B. Posadas, C. Mitra, A. V. Kvit, J. Ramdani, and A. A. Demkov, "Band Alignment and Electronic Structure of the Anatase $TiO_2/SrTiO_3$ (001) Heterostructure Integrated on Si (001)," *Phys. Rev. B*, vol. 86, no. 7, p. 075301, 2012.

[172] B. Sun, A. V. Vorontsov, and P. G. Smirniotis, "Role of Platinum Deposited on TiO_2 in Phenol Photocatalytic Oxidation," *Langmuir*, vol. 19, no. 8, pp. 3151–3156, 2003.

[173] L. Forro, O. Chauvet, D. Emin, L. Zuppiroli, H. Berger, and F. Levy, "High Mobility n-type Charge Carriers in Large Single Crystals of Anatase (TiO_2)," *J. Appl. Phys.*, vol. 75, no. 1, pp. 633–635, 1994.

[174] M. J. Wolf, K. P. McKenna, and A. L. Shluger, "Hole Trapping at Surfaces of m-ZrO_2 and m-HfO_2 Nanocrystals," *J. Phys. Chem. C*, vol. 116, no. 49, pp. 25888–25897, 2012.

[175] S. K. Wallace and K. P. Mckenna, "Facet-Dependent Electron Trapping in TiO_2 Nanocrystals," *J. Phys. Chem. C*, vol. 119, no. 4, pp. 1913–1920, 2015.

[176] K. Wakabayashi, Y. Yamaguchi, T. Sekiya, and S. Kurita, "Time-Resolved Luminescence Spectra in Colorless Anatase TiO_2 Single Crystal," *J. Lumin.*, vol. 112, no. 1-4, pp. 50–53, 2005.

[177] C. C. Mercado, F. J. Knorr, and J. L. McHale, "Observation of Charge Transport in Single Titanium Dioxide Nanotubes by Micro-Photoluminescence Imaging and Spectroscopy," *ACS Nano*, vol. 6, no. 8, pp. 7270–7280, 2012.

[178] J. A. Quirk, B. Miao, B. Feng, G. Kim, H. Ohta, Y. Ikuhara, and K. P. McKenna, "Unveiling the Electronic Structure of Grain Boundaries in Anatase with Electron Microscopy and First-Principles Modelling," *Nano Lett.*, 2021. Just accepted.

[179] H. Nishimura, K. Matsunaga, T. Saito, T. Yamamoto, and Y. Ikuhara, "Atomic Structures and Energies of Σ7 Symmetrical Tilt Grain Boundaries in Alumina Bicrystals," *J. Am. Ceram. Soc.*, vol. 86, no. 4, pp. 574–80, 2003.

[180] Y. Yan, M. Chisholm, G. Duscher, A. Maiti, S. Pennycook, and S. Pantelides, "Impurity-Induced Structural Transformation of a MgO Grain Boundary," *Phys. Rev. Lett.*, vol. 81, no. 17, p. 3675, 1998.

[181] G. Schusteritsch, R. Ishikawa, A. Elmaslmane, K. Inoue, K. McKenna, Y. Ikuhara, and C. Pickard, "Anatase-Like Grain Boundary Structure in Rutile Titanium Dioxide," *Nano Lett.*, 2021.

[182] S.-Y. Choi, S.-D. Kim, M. Choi, H.-S. Lee, J. Ryu, N. Shibata, T. Mizoguchi, E. Tochigi, T. Yamamoto, S.-J. L. Kang, *et al.*, "Assessment of Strain-Generated Oxygen Vacancies Using $SrTiO_3$ Bicrystals," *Nano Lett.*, vol. 15, no. 6, pp. 4129–4134, 2015.

[183] M. Lazzeri and A. Selloni, "Stress-Driven Reconstruction of an Oxide Surface: the Anatase TiO_2 (001)-(1× 4) Surface," *Phys. Rev. Lett.*, vol. 87, no. 26, p. 266105, 2001.

[184] V. Lusvardi, M. Barteau, J. G. Chen, J. Eng Jr, B. Frühberger, and A. Teplyakov, "An NEXAFS Investigation of the Reduction and Reoxidation of TiO_2 (001)," *Surf. Sci*, vol. 397, no. 1-3, pp. 237–250, 1998.

[185] I. Justicia, P. Ordejón, G. Canto, J. L. Mozos, J. Fraxedas, G. A. Battiston, R. Gerbasi, and A. Figueras, "Designed Self-Doped Titanium Oxide Thin Films for Efficient Visible-Light Photocatalysis," *Adv. Mater.*, vol. 14, no. 19, pp. 1399–1402, 2002.

[186] S. Wei, S. Ni, and X. Xu, "A New Approach to Inducing Ti^{3+} in Anatase TiO_2 for Efficient Photocatalytic Hydrogen Production," *Chinese J. of Catal.*, vol. 39, no. 3, pp. 510–516, 2018.

[187] J. Liu, Q. Liu, P. Fang, C. Pan, and W. Xiao, "First Principles Study of the Adsorption of a NO Molecule on N-doped Anatase Nanoparticles," *Appl. Surf. Sci.*, vol. 258, no. 20, pp. 8312–8318, 2012.

[188] Y. Lei, H. Liu, and W. Xiao, "First Principles Study of the Size Effect of TiO_2 Anatase Nanoparticles in Dye-Sensitized Solar Cell," *Model. Simul. Mater. Sci. Eng*, vol. 18, no. 2, p. 025004, 2010.

[189] F. De Angelis, S. Fantacci, and A. Selloni, "Alignment of the Dye's Molecular Levels with the TiO_2 Band Edges in Dye-sensitized Solar Cells: a DFT-TDDFT study," *Nanotechnology*, vol. 19, no. 42, p. 424002, 2008.

[190] R. Valero, A. Morales-Garcia, and F. Illas, "Investigating the Character of Excited States in TiO2 Nanoparticles from Topological Descriptors: Implications for Photocatalysis," *Phys. Chem. Chem. Phys.*, vol. 22, no. 5, pp. 3017–3029, 2020.

[191] O. Lamiel-Garcia, K. C. Ko, J. Y. Lee, S. T. Bromley, and F. Illas, "When Anatase Nanoparticles Become Bulklike: Properties of Realistic TiO_2 Nanoparticles in the 1-6 nm Size Range From All Electron Relativistic Density Functional Theory Based Calculations," *J. Chem. Theory Comput.*, vol. 13, no. 4, pp. 1785–1793, 2017.

[192] Á. Morales-García, R. Valero, and F. Illas, "Electronic Properties of Realistic Anatase TiO_2 Nanoparticles from G_0W_0 Calculations on a Gaussian and Plane Waves Scheme," *J. Chem. Theory Comput.*, vol. 15, no. 9, pp. 5024–5030, 2019.

[193] O. Lamiel-Garcia, A. Cuko, M. Calatayud, F. Illas, and S. T. Bromley, "Predicting Size-Dependent Emergence of Crystallinity in Nanomaterials: Titania Nanoclusters Versus Nanocrystals," *Nanoscale*, vol. 9, no. 3, pp. 1049–1058, 2017.

[194] Morales-García, O. Lamiel-García, R. Valero, and F. Illas, "Properties of Single Oxygen Vacancies on a Realistic $(TiO_2)_{84}$ Nanoparticle: a Challenge for Density Functionals," *J. Phys. Chem. C*, vol. 122, no. 4, pp. 2413–2421, 2018.

[195] K. C. Ko, O. Lamiel-García, J. Y. Lee, and F. Illas, "Performance of a Modified Hybrid Functional in the Simultaneous Description of Stoichiometric and Reduced TiO_2 Polymorphs," *Phys. Chem. Chem. Phys.*, vol. 18, no. 17, pp. 12357–12367, 2016.

[196] G. J. Martyna and M. E. Tuckerman, "A Reciprocal Space Based Method for Treating Long Range Interactions in Ab Initio and Force-Field-Based Calculations in Clusters," *J. Chem. Phys.*, vol. 110, no. 6, pp. 2810–2821, 1999.

[197] Y. He, O. Dulub, H. Cheng, A. Selloni, and U. Diebold, "Evidence for the Predominance of Subsurface Defects on Reduced Anatase TiO_2 (101)," *Phys. Rev. Lett.*, vol. 102, no. 10, p. 106105, 2009.

[198] P. Scheiber, M. Fidler, O. Dulub, M. Schmid, U. Diebold, W. Hou, U. Aschauer, and A. Selloni, "(Sub) Surface Mobility of Oxygen Vacancies at the TiO_2 Anatase (101) Surface," *Phys. Rev. Lett.*, vol. 109, no. 13, p. 136103, 2012.

[199] X. Liu, H. Xu, L. R. Grabstanowicz, S. Gao, Z. Lou, W. Wang, Y. Dai, T. Xu, *et al.*, "Ti^{3+} Self-doped TiO_{2-x} Anatase Nanoparticles via Oxidation of TiH_2 in H_2O_2," *Catal. Today*, vol. 225, pp. 80–89, 2014.

[200] T. Sekiya, S. Kamei, and S. Kurita, "Luminescence of Anatase TiO_2 Single Crystals Annealed in Oxygen Atmosphere," *J. Lumin.*, vol. 87, pp. 1140–1142, 2000.

[201] B. Choudhury and A. Choudhury, "Oxygen Defect Dependent Variation of Band Gap, Urbach Energy and Luminescence Property of Anatase, Anatase-Rutile Mixed Phase and of Rutile Phases of TiO_2 Nanoparticles," *Physica E Low Dimens. Syst. Nanostruct.*, vol. 56, pp. 364–371, 2014.

[202] W. Tang, E. Sanville, and G. Henkelman, "A Grid-Based Bader Analysis Algorithm Without Lattice Bias," *J. Phys. Condens. Matter*, vol. 21, no. 8, p. 084204, 2009.

[203] E. Sanville, S. D. Kenny, R. Smith, and G. Henkelman, "Improved Grid-Based Algorithm for Bader Charge Allocation," *J. Comput. Chem.*, vol. 28, no. 5, pp. 899–908, 2007.

[204] G. Henkelman, A. Arnaldsson, and H. Jónsson, "A Fast and Robust Algorithm for Bader Decomposition of Charge Density," *Comput. Mater. Sci.*, vol. 36, no. 3, pp. 354–360, 2006.

[205] M. Yu and D. R. Trinkle, "Accurate and Efficient Algorithm for Bader Charge Integration," *J. Chem. Phys.*, vol. 134, no. 6, p. 064111, 2011.

[206] B. Huber, A. Brodyanski, M. Scheib, A. Orendorz, C. Ziegler, and H. Gnaser, "Nanocrystalline Anatase TiO_2 Thin Films: Preparation and Crystallite Size-Dependent Properties," *Thin Solid Films*, vol. 472, no. 1-2, pp. 114–124, 2005.

[207] T. Dittrich, J. Weidmann, F. Koch, I. Uhlendorf, and I. Lauermann, "Temperature-and Oxygen Partial Pressure-Dependent Electrical Conductivity in Nanoporous Rutile and Anatase," *Appl. Phys. Lett.*, vol. 75, no. 25, pp. 3980–3982, 1999.

[208] I. R. Macdonald, R. F. Howe, X. Zhang, and W. Zhou, "In Situ EPR Studies of Electron Trapping in a Nanocrystalline Rutile," *J. Photoch. Photobio. A*, vol. 216, no. 2-3, pp. 238–243, 2010.

[209] K. Sellschopp, W. Heckel, J. Gäding, C. J. Schröter, A. Hensel, T. Vossmeyer, H. Weller, S. Müller, and G. Vonbun-Feldbauer, "Shape-Controlling Effects of Hydrohalic and Carboxylic Acids in TiO_2 Nanoparticle Synthesis," *J. Chem. Phys.*, vol. 152, no. 6, p. 064702, 2020.

[210] G. Liu, C. Y. Jimmy, G. Q. M. Lu, and H.-M. Cheng, "Crystal Facet Engineering of Semiconductor Photocatalysts: Motivations, Advances and Unique Properties," *Chem. Comm.*, vol. 47, no. 24, pp. 6763–6783, 2011.

[211] E. Maras, M. Saito, K. Inoue, H. Jónsson, Y. Ikuhara, and K. P. McKenna, "Determination of the Structure and Properties of an Edge Dislocation in Rutile TiO_2," *Acta Mater.*, vol. 163, pp. 199–207, 2019.

[212] D. Emin and T. Holstein, "Studies of Small-Polaron Motion IV. Adiabatic Theory of the Hall Effect," *Ann. Phys.*, vol. 53, no. 3, pp. 439–520, 1969.

[213] R. A. Marcus and N. Sutin, "Electron Transfers in Chemistry and Biology," *Biochim. Biophys. Acta*, vol. 811, no. 3, pp. 265–322, 1985.

[214] J. C. Slater, "Atomic Shielding Constants," *Phys. Rev.*, vol. 36, no. 1, p. 57, 1930.

[215] W. Olovsson, C. Göransson, T. Marten, and I. A. Abrikosov, "Core-Level Shifts in Complex Metallic Systems From First Principles," *Phys. Status Solidi B*, vol. 243, no. 11, pp. 2447–2464, 2006.

Appendix A

Charge Trapping in {112} and {110} Twin Boundaries in Anatase: Supplemental Material

To analyse the factors that influence the stability of polarons at particular sites we can define a strain energy, S, as

$$S = E_{\text{tot}}[\text{Polaron}] - E_{\text{tot}}[\text{Neutral}], \tag{A.0.1}$$

where $E_{\text{tot}}[\text{Polaron}]$ is the total energy of the cell containing the polaron and $E_{\text{tot}}[\text{Neutral}]$ is the total energy of the same polaron geometry, but with the charge removed. From this we can define a relative strain energy, ΔS, as

$$\Delta S = S_{\text{TB}} - S_{\text{Bulk}}, \tag{A.0.2}$$

where S_{TB} and S_{Bulk} are the strain energies of a twin boundary (TB) polaron and a bulk-like polaron, respectively. This provides a means by which to consider how the strain at different sites contributes to the total energy. To further characterise differences in electrostatic properties between sites in the 'pristine' TB we consider the average electrostatic energy, $\bar{V}_i$, on a given ion at position $\mathbf{R}_i$ defined as

$$\bar{V}_i = \int V(\mathbf{r})\rho_{\text{Test}}(|\mathbf{r} - \mathbf{R}_i|)\,\mathrm{d}^3\mathbf{r}, \tag{A.0.3}$$

where V is the electrostatic potential and ρ_{Test} is a test charge density which is normalised to 1. We have chosen ρ_{Test} to take the form of a Slater-type $1s$ orbital.[214] We

then define a core-level shift, Δc, as

$$\Delta c = \bar{V}_i - \bar{V}_{\text{Bulk}}, \tag{A.0.4}$$

where $\bar{V}_{\text{Bulk}}$ is the average electrostatic potential on a bulk-like ion of the same species. Core level shifts have been shown to provide a good measure of the 'chemical environment' of an ion in a lattice.[215]

TB	Site	$\Delta\ E_{\text{T}}$	S	ΔS	Δc
{112}	Bulk-like	0.000	1.011	0.000	0.000
	(a)	-0.178	1.016	0.005	0.068
	(b)	-0.158	1.017	0.007	-0.013
{110}	Bulk-like	0.000	1.042	0.000	0.000
	(c)	0.073	1.041	-0.001	-0.099
	(d)	-0.142	1.057	0.015	-0.051

Table A.1: Relative trapping energies (ΔE_{T}), total strain energies (S), strain energy relative to a bulk-like hole polaron (ΔS), and core level shifts (Δc) in the {112} and {110} TB. Sites are labelled (a), (b), (c), and (d) corresponding to polarons shown in the alphabetically labelled panels in Fig 4.5 in the main text. Bulk-like polarons are taken to be a polaron trapped in the plane of atoms in the center of each grain, equidistant from both TB planes in the supercell.) All energies are quoted in eV.

Appendix B

An Experimental and Computational Study of Σ5 Anatase Bicrystals: Supplemental Material

The initial GB models used for the scans of rigid-body translations and corresponding energy surfaces are shown in Figure B.1. The Σ5{310} shows two inequivalent minima marked A and B, with formation energies of 1.03 Jm^{-2} and 1.09 Jm^{-2}, respectively (Figure B.1a). Minima A corresponds to a post-optimization translation of 0.00 Å and 2.53 Å in the $[1\bar{3}0]$ and [001] directions and minima B corresponds to post-optimization translations of 3.00 Å and 0.00 Å. The scan of rigid-body translations for the Σ5{103}-S shows one distinct minima (Figure B.1b) that corresponds to small formation energy of just 0.64 Jm^{-2} and translations of 4.93 Å and 0.04 Å in the $[33\bar{1}]$ and [010] directions, respectively. The lowest-energy structure for the Σ5{103}-AS corresponds to a post-optimization translation of 5.61 Å and 0.47Å in the $[33\bar{1}]$ and [010] directions, respectively (Figure B.1c), quite similar to the post-optimization translation for the stable Σ5{103}-S structure. At each considered translation, all atoms are allowed to relax, the lattice vectors parallel to the GB plane are held fixed, and the lattice vector normal to the to the GB plane is allowed to relax.

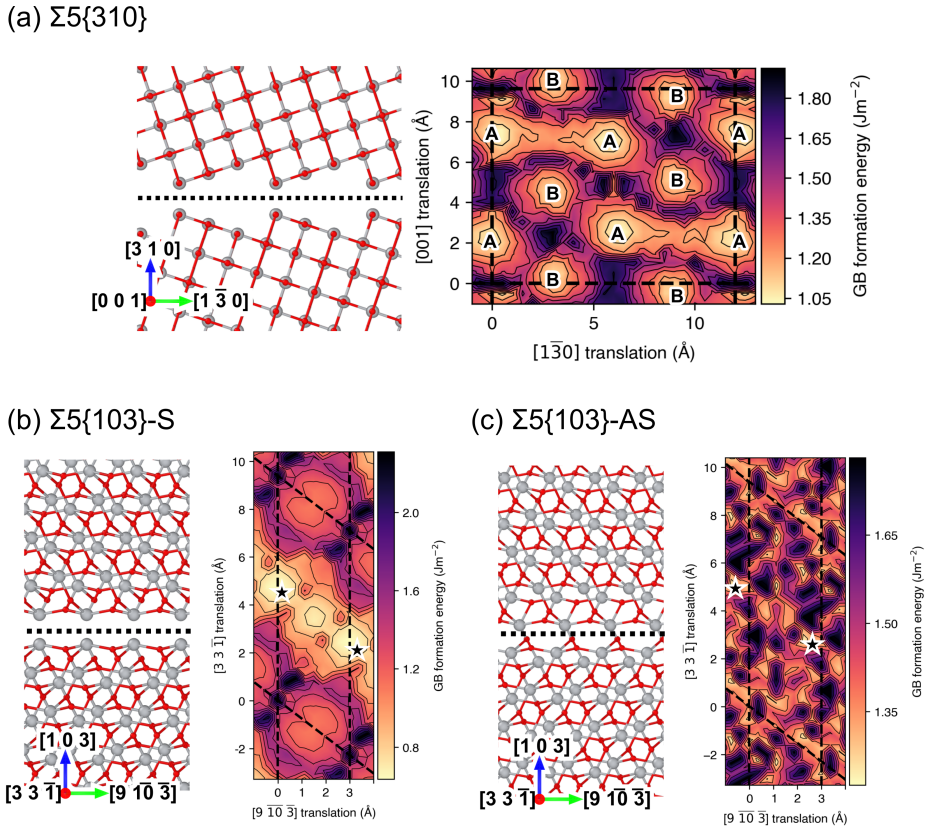

Fig. B.1. Initial structures and their associated rigid-body translation formation energy surfaces for the (a) [001]Σ5{310} grain boundary (GB) where uppercase A and B labelled on the energy surface plot indicate minima inequivalent minima, (b) [33$\bar{1}$]Σ5{103}-S GB, and (c) [33$\bar{1}$]Σ5{103}-AS GB where the star-shaped markers on the energy surface plot indicate the energy minima. Large gray spheres are titanium, small red spheres are oxygen, and where the dotted line indicates the GB plane separating each grain. Dashed lines on the energy surface plots mark the boundary of the simulation supercells used in the scans.